NOTE TO USERS

This reproduction is the best copy available.

UMI®

Reproduced with permission of the copyright owner. Further reproduction prohibited without permission.

Reproduced with permission of the copyright owner. Further reproduction prohibited without permission.

SUPERCONDUCTOR-INSULATOR TRANSITION IN QUASI-ONE-DIMENSIONAL NANOWIRES

BY

ANTHONY TRAVIS BOLLINGER

B.S., Purdue University, 1999

DISSERTATION

Submitted in partial fulfillment of the requirements
for the degree of Doctor of Philosophy in Physics
in the Graduate College of the
University of Illinois at Urbana-Champaign, 2005

Urbana, Illinois

Reproduced with permission of the copyright owner. Further reproduction prohibited without permission.

UMI Number: 3198930

INFORMATION TO USERS

The quality of this reproduction is dependent upon the quality of the copy submitted. Broken or indistinct print, colored or poor quality illustrations and photographs, print bleed-through, substandard margins, and improper alignment can adversely affect reproduction.

In the unlikely event that the author did not send a complete manuscript and there are missing pages, these will be noted. Also, if unauthorized copyright material had to be removed, a note will indicate the deletion.

UMI®

UMI Microform 3198930

Copyright 2006 by ProQuest Information and Learning Company.

All rights reserved. This microform edition is protected against unauthorized copying under Title 17, United States Code.

ProQuest Information and Learning Company
300 North Zeeb Road
P.O. Box 1346
Ann Arbor, MI 48106-1346

Reproduced with permission of the copyright owner. Further reproduction prohibited without permission.

© 2005 by Anthony Travis Bollinger. All rights reserved.

Reproduced with permission of the copyright owner. Further reproduction prohibited without permission.

CERTIFICATE OF COMMITTEE APPROVAL

University of Illinois at Urbana-Champaign
Graduate College

August 23, 2005

We hereby recommend that the thesis by:

ANTHONY TRAVIS BOLLINGER

Entitled:

SUPERCONDUCTOR-INSULATOR TRANSITION IN QUASI-ONE-DIMENSIONAL NANOWIRES

Be accepted in partial fulfillment of the requirements for the degree of:

Doctor of Philosophy

Signatures:

Director of Research - Alexey Bezryadin

Head of Department - Jeremiah Sullivan

Committee on Final Examination*

Chairperson - Dale Van Harlingen

Committee Member - Philip Phillips

Committee Member - John D. Stack

Committee Member -

Committee Member -

Committee Member -

* Required for doctoral degree but not for master's degree

Reproduced with permission of the copyright owner. Further reproduction prohibited without permission.

SUPERCONDUCTOR-INSULATOR TRANSITION IN
QUASI-ONE-DIMENSIONAL NANOWIRES

Anthony Travis Bollinger, Ph.D.
Department of Physics
University of Illinois at Urbana-Champaign, 2005
Alexey Bezryadin, Advisor

We have studied a large group of superconducting MoGe nanowires fabricated by a molecular templating technique. A well-defined superconductor-insulator transition (SIT) is observed in homogeneous wires with lengths less than ~200 nm. The total normal state resistance of the wire is found to be the control parameter for this transition with the critical point occurring near the quantum of resistance for Cooper pairs. Wires in the superconducting phase of the SIT are well described by the Langer-Ambegaokar-McCumber-Halperin theory of thermally activated phase slips. No resistance "tails" characteristic of quantum phase slips were observed. Wires in the insulating phase of the SIT follow the predictions of the theory of weak Coulomb blockade in a diffusive normal metal. Longer wires display signs of a "mixed" behavior that is similar to that found for inhomogeneous wires in which a single wire acts as a combination of two or more superconducting and/or insulating sections.

Reproduced with permission of the copyright owner. Further reproduction prohibited without permission.

This dissertation is dedicated to the memory of Don Bollinger

Reproduced with permission of the copyright owner. Further reproduction prohibited without permission.

Acknowledgements

The work presented in this dissertation could not have been completed without the assistance of many people. Foremost, I would like to thank my advisor, Alexey Bezryadin. His guidance and patience with me have been extremely beneficial and I have learned more from him than he probably knows. Alexey is an excellent experimentalist and I feel fortunate to have been able to learn from him. The other person who had the greatest impact on my development at Illinois is Andrey Rogachev. He was always willing to lend a hand and teach me new things about physics, fabrication, and measurement. The best advice I received about doing research on my own and with others came from him and for that I am ever grateful.

Much of the nanowire fabrication was performed in the Microfabrication and Crystal Growth Facility and class 100 cleanroom of the Materials Research Laboratory. I thank Tony Banks for all of his hard work in maintaining this excellent resource and for his technical advice (which includes knowledge of the hot fishing spots close to Champaign). I am also grateful to Vania Petrova, Mike Marshall, Steve Burdin, and Nancy Finnegan of the Center for Materials Microanalysis for instrument training and assistance. John Hughes and Gabe Cueva of the Micro and Nanotechnology laboratory were also helpful in electron beam writing and pattern generation.

Reproduced with permission of the copyright owner. Further reproduction prohibited without permission.

The past and present members of Alexey's research group have provided a continuous source of ideas, answers, and encouragement while keeping the atmosphere in the lab very open and enjoyable. These include Ulas Coskun, Mike Boss, Brent Trenhaile, Dave Hopkins, Thomas Aref, Mitrabhanu Sahu, Rob Dinsmore, Matthew Brenner, Jack Waddell, Johnathan Whitmer, Mark Murphey, Sang Lin Chu, Alan Dibos, Mikas Remeika, Bob Colby, C. J. Lo, Anil Nandyala, and Hisashi Kajiura. I have also benefited from interactions with students of Dale Van Harlingen's research group. Tony Bonetti and Sergey Frolov provided fabrication assistance and advice at the beginning of this project and Trevis Crane's help was crucial during dilution fridge measurements.

Finally, I would like to thank my wife, Kirsten, for everything she has done for me during our time here in Illinois. My graduate school experience has been much easier and enjoyable because of her. The love and support of my parents, Mark and Ginger Bollinger, has also carried me through this time. Because they always said I could, I have. I also thank Adam Bollinger, M. O. Bollinger, Cleone Peterson, Lance and Jan Peterson, and George and Barbara Whittaker for their love and Derek Tournear, Mike Goins, Perry Trowbridge, Steve and Tara Young, Jeff and Jen Schroder, Pete and Jen Farm, and Geoff and Raechel Ingrum for their friendship.

This work was supported by NSF CAREER grant #DMR 01-34770, DOE Grant #DEFG02-91-ER45439, the Alfred P. Sloan Foundation, and the University of Illinois Department of Physics through teaching assistantships. Some fabrication was carried out in the Center for Microanalysis of Materials, University of Illinois, which is partially supported by the U. S. Department of Energy under grant DEFG02-91-ER45439.

Reproduced with permission of the copyright owner. Further reproduction prohibited without permission.

Contents

Chapter

List of Tables ..... **x**

List of Figures ..... **xi**

1 Introduction **1**

1.1 References 6

2 Physics of One-Dimensional Superconductors **9**

2.1 Thermal fluctuations 9

2.1.1 Phase slips 9

2.1.2 The free energy barrier 11

2.1.3 LAMH resistance 17

2.1.4 Experimental verification 21

2.2 Quantum fluctuations 21

2.2.1 The Giordano model 23

2.2.2 Quantum phase slip theories 26

2.2.3 Experimental comparison 28

2.3 The superconductor-insulator transition 33

2.4 References 38

3 Fabrication and Measurement of Superconducting Nanowires **40**

3.1 Fabrication of superconducting nanowires 42

Reproduced with permission of the copyright owner. Further reproduction prohibited without permission.

3.1.1 Preparing the substrate 42
3.1.2 Depositing fluorinated single walled carbon nanotubes 43
3.1.3 Sputtering MoGe 45
3.1.4 Scanning electron microscopy 49
3.1.5 Photolithography and etching 51
3.2 Measurement of superconducting nanowires 53
3.2.1 Mounting the sample 53
3.2.2 Cryostats 54
3.2.3 Electrical measurements 57
3.3 References 59

4 Properties of Superconducting Nanowires 61
4.1 Homogeneity of nanowires 61
4.1.1 Resistance vs. temperature curves 61
4.1.2 Critical temperature of film electrodes 63
4.1.3 Nanowire resistivity 66
4.2 R(T) behavior of superconducting nanowires 67
4.2.1 Comparison with LAMH theory 69
4.2.2 Comparison with QPS theories 72
4.3 V(I) behavior of superconducting nanowires 75
4.3.1 V(I) curves 75
4.3.2 Retrapping and switching currents 77
4.3.3 Differential resistance curves 79
4.4 Effect of magnetic field on superconducting nanowires 80
4.5 References 91

5 Properties of Insulating Nanowires 95
5.1 Introduction 96
5.2 Recap of fabrication and measurement 97
5.3 R(T) behavior of insulating nanowires 98
5.4 dI(V)/dV behavior of insulating nanowires 103

Reproduced with permission of the copyright owner. Further reproduction prohibited without permission.

5.5 Conclusions 107
5.6 References 108

6 The Superconductor-Insulator Transition 111
6.1 R(T) Curves 116
6.2 Phase Diagram 121
6.3 Role of homogeneity 128
6.3.1 Introduction 129
6.3.2 Essential fabrication difference 130
6.3.3 Estimation of oxidized MoGe thickness 132
6.3.4 Recap of measurement 134
6.3.5 R(T) measurements 134
6.3.6 dV(I)/dI measurements 137
6.3.7 Discussion of inhomogeneous wires 138
6.3.8 Conclusions 140
6.4 Final conclusions 140
6.5 References 141

7 Additional Measurements – Superconducting Nanobridges 144
7.1 Introduction 144
7.2 Experimental Setup 149
7.3 Results 151
7.4 Discussion 153
7.4.1 LAMH attempt frequency for a short bridge 154
7.4.2 Modification of the prefactor 154
7.4.3 Determination of the linear resistance from high bias current measurements 157
7.5 Summary 161
7.6 References 161

Author's Biography 164

Reproduced with permission of the copyright owner. Further reproduction prohibited without permission.

List of Tables

3.1 Measured and derived physical parameters for MoGe 46

6.1 Parameters for short and standard length samples 113

6.2 Parameters for long samples 114

6.3 Parameters of nanowires used in morphology study 132

7.1 Parameters of nanobridge samples 150

Reproduced with permission of the copyright owner. Further reproduction prohibited without permission.

List of Figures

2.1 Depiction of a phase slip event 11
2.2 Free energy diagrams 18
2.3 Data from early experiments with fits to the LAMH theory 22
2.4 Data from Giordano with fits to his model of MQT 25
2.5 Data from Lau *et al.* with fits to Giordano's model of MQT 29
2.6 Data from Lau with fits to the microscopic theory of QPS 31
2.7 Data from Zgirski *et al.* with fits to the microscopic theory of QPS 32
2.8 Data from Xiong, Herzog, and Dynes displaying a superconductor-insulator transition 34
2.9 Data from Bezryadin, Lau, and Tinkham displaying a superconductor-insulator transition 35
2.10 Data from Rogachev and Bezryadin displaying a superconductor-insulator transition 38
3.1 Diagram of fabrication steps 41
3.2 Bulk critical temperature as a function of germanium content for $Mo_{1-x}Ge_x$ 45
3.3 TEM image of a MoGe wire 47
3.4 The AJA sputtering system 48
3.5 The Hitachi S-4700 SEM 49
3.6 SEM images of wires 50
3.7 SEM images of alignment markers 50
3.8 The Suss Microtech Inc. MJB3 mask aligner 51
3.9 Diagram of electrode pad photolithography mask 52
3.10 SEM image of finished device 53

Reproduced with permission of the copyright owner. Further reproduction prohibited without permission.

3.11 Pictures of cryostats 54
3.12 Circuit diagram for measurement of nanowires 57
4.1 Resistance vs. temperature curves for representative nanowires 62
4.2 Comparison of film electrode critical temperature vs. film thickness 64
4.3 Normal state resistance divided by length vs. width times thickness for all nanowires 67
4.4 Resistance vs. temperature curves for the superconducting samples 68
4.5 Comparison of resistance vs. temperature data to the LAMH theory 69
4.6 Fitting parameters used in the fits to the LAMH theory 71
4.7 Resistance vs. temperature data compared with Giordano's model of MQT 73
4.8 Resistance vs. temperature data compared with Golubev and Zaikin's model of QPS 74
4.9 Voltage vs. current behavior at different temperatures for a representative nanowire 76
4.10 Switching current vs. temperature 78
4.11 Differential resistance vs. bias current for a representative sample 80
4.12 Resistance vs. temperature for a Nb nanowire in different magnetic fields 82
4.13 Voltage vs. current dependence of a MoGe nanowire at different temperatures 84
4.14 Differential resistance vs. bias current of a MoGe nanowire at different temperatures 85
4.15 Resistance vs. temperature of a MoGe nanowire at zero and high magnetic field 86
4.16 Adjustable parameters used in the LAMH fits 88
4.17 Normalized critical temperature vs. normalized magnetic field 89
5.1 SEM image and comparison of resistance vs. temperature curves of superconducting and insulating nanowires 99
5.2 Normalized conductance change vs. temperature curves for insulating wires 102

Reproduced with permission of the copyright owner. Further reproduction prohibited without permission.

5.3 Differential conductance vs. bias voltage curves for insulating wires 104
5.4 Fitting parameters used in the fits to Golubev and Zaikin's theory of weak Coulomb blockade 106
6.1 Resistance vs. temperature curves for standard length (~100 nm) wires 115
6.2 Resistance vs. temperature curves for short (~50 nm) wires 117
6.3 Resistance vs. temperature curves for long (~450 nm) wires 118
6.4 Voltage vs. current curves for sample 020904a 120
6.5 Resistance vs. temperature curve for sample 041204l 120
6.6 Resistance vs. temperature curves for short and standard length wires 122
6.7 Resistance per unit length vs. temperature curves for short and standard length wires 123
6.8 Phase diagram of all measured samples 125
6.9 Critical temperature vs. total normal state resistance 127
6.10 Sample configuration and TEM micrographs of homogeneous and inhomogeneous nanowires 131
6.11 Length per unit resistance vs. width and film critical temperature vs. film thickness for homogeneous and inhomogeneous samples 133
6.12 Resistance vs. temperature for homogeneous and inhomogeneous samples .. 135
6.13 Differential resistance vs. bias current for homogeneous and inhomogeneous samples 137
7.1 Sample schematic and SEM micrograph of a typical sample 145
7.2 Low-bias resistance versus temperature dependence measured on a thin film without constriction 151
7.3 Low-bias resistance for five different samples with bridges 153
7.4 Differential resistance as a function of the dc bias current for sample B2 158
7.5 Resistance vs. temperature curve for sample B2 159

Reproduced with permission of the copyright owner. Further reproduction prohibited without permission.

Chapter 1

Introduction

The subject of one-dimensional superconductivity is many decades old. Despite its age, it continues to be a topic of great interest and a fundamental field of condensed matter research. The central question in one-dimensional superconductivity is how the superconducting properties of a wire are destroyed as its dimensions are reduced. Continual advancements in fabrication techniques have allowed researchers to create wires of ever shrinking size, resulting in an increasing number of observed effects that shed light on this basic question.

For superconductivity to survive in any system two requirements must be met. The electrons in the system must have some attractive interaction between them, thus condensing into bosons called Cooper pairs. The Cooper pairs then must become phase coherent. If either of these two conditions is not present, superconductivity will be extinguished. The main way that superconductivity is weakened in a one-dimensional wire is by thermal fluctuations, which break the phase coherence of the wire. Since these fluctuations are always present for all temperatures, $T > 0$, a one-dimensional wire can only be in a truly superconducting state with a resistance, R, that is zero at $T = 0$.

The first experiments that uncovered an underlying effect from thermal fluctuations in wires were by Parks and Groff [1], who observed an anomalous

Reproduced with permission of the copyright owner. Further reproduction prohibited without permission.

temperature dependence of the critical current in Sn microstrips that were a few microns wide and tens of nanometers thick. Their work was inspired by seeing a preprint from Little [2], who was the first to recognize the importance of thermal fluctuations in wires, and showed that these fluctuations could lead to the decay of a persistent current in a wire loop.

Other experiments [3, 4] were performed that showed signs of thermal fluctuation effects and soon a rigorous theory, based on Ginzburg-Landau theory [5], was produced by Langer, Ambegaokar, McCumber and Halperin (LAMH) [6, 7]. In the LAMH theory, a free energy barrier exists between quasi-stationary states that are characterized by a phase difference across the wire of the Ginzburg-Landau order parameter that varies by multiples of 2π from state to state. The thermal activation of the system over this free energy barrier results in the order parameter going to zero at some point along the wire and the phase "slipping" by 2π, which leads to dissipation and hence resistance. While the LAMH theory was originally derived for the case of voltage biased wires, McCumber [8] showed that in the experimentally relevant situation of current biasing, the results of the LAMH theory are identical. The predictions of the LAMH theory were subsequently confirmed in separate experiments by Lukens, Warburton, and Webb [9] and Newbower, Beasley, and Tinkham [10] on Sn whiskers that were ~ 0.5 μm in diameter and showed good agreement with the LAMH theory of thermally activated phase slips over many orders of magnitude in resistance.

As microfabrication techniques developed, Giordano was able to perform a series of measurements on In and PbIn wires that had effective diameters ranging from 15-100 nm [11-14]. He observed a crossover in the thinnest samples from LAMH behavior to a

Reproduced with permission of the copyright owner. Further reproduction prohibited without permission.

weaker temperature dependence of the resistance characterized by resistance "tails". This additional resistance was attributed to quantum phase slips (QPS), in which the system tunnels through the free energy barrier [15] rather than being thermally activated over it. Giordano's work lead to a surge in QPS theories [16-23] and some recent experimental work supports the existence of QPS effects in one-dimensional wires [24-26]. However, other experiments have not observed such effects, adding to the debate over whether QPS are observable in one-dimensional superconducting wires or not [16, 18]. For example, Sharifi, Herzog, and Dynes [27] found a systematic deviation from LAMH behavior in measurements on Pb wires 22-55 nm wide, but no crossover to a more weakly temperature dependent behavior (i.e. no resistance "tail").

Adding to the account of the examination of the disappearance of superconductivity in one-dimension is the observation by Bezryadin, Lau, and Tinkham [28] of a superconductor-insulator transition (SIT) in superconducting nanowires ~10 nm in width made of amorphous MoGe. It was found that for wires whose normal state resistance was less than the quantum resistance for Cooper pairs, $R_Q = h/4e^2$, the wires were superconducting, while wires with normal resistances greater than R_Q were insulating, with increasing resistance as $T \to 0$ and no signs of superconductivity whatsoever. A similar dichotomy was observed by Rogachev and Bezryadin [29] with Nb nanowires 10-20 nm in width. Theoretical work exists that can explain some features of the SIT and can be broken into two groups. Some theories describe a "fermionic" mechanism in which Cooper pairs do not form, due to the critical temperature of the superconducting wire being driven to zero by processes such as weak localization [30] or increased Coulomb repulsion [31]. Other theories describe a "bosonic" mechanism in

Reproduced with permission of the copyright owner. Further reproduction prohibited without permission.

which the phase coherence of the wire is completely destroyed by a proliferation of QPS [18, 20, 21]. The SIT story is complicated by the fact that the experiments by Lau *et al.* [24] on a set of longer MoGe nanowires fabricated by the same method as in Ref. [28] did not show a SIT but rather signs of a crossover from superconducting to insulating behavior as the cross-sectional area of the wire was reduced.

While the history of one-dimensional superconductivity is filled with many breakthroughs, both theoretically and experimentally, it is clear from the brief description above of the work to date that unanswered questions remain. Specifically, does a superconductor-insulator transition in one-dimensional superconducting wires truly exist? If so, what controls it? What are the requirements for its occurrence? And what are the natures of the superconducting and insulating phases? Also, why have quantum phase slips been observed in some experiments but not others? These questions are the motivation for the work presented in this dissertation as they keep the subject of one-dimensional superconductivity from being as understood as superconductivity in other reduced dimensions, namely two-dimensional films [32, 33], zero-dimensional Josephson junctions [34-36], and zero-dimensional grains [37-39].

In this dissertation, a systematic study will be presented that shows that a superconductor-insulator transition does exist in one-dimensional superconducting wires. Throughout this dissertation we refer to those wires in the superconducting phase of the SIT as "superconducting" wires and those in the insulating phase as "insulating". We would like to stress here that the insulating wires are not *strictly* insulating in the sense of infinite resistance at zero temperature. Rather we refer to them as insulating because their resistance increases with cooling at low temperatures and they show a zero peak

Reproduced with permission of the copyright owner. Further reproduction prohibited without permission.

resistance peak. The contents of this work are laid out as follows. In Chapter 2, we will look more closely at some of the relevant work outlined in this introduction, beginning with the LAMH theory of thermally activated phase slips and its experimental confirmation. We will then examine Giordano's observation of macroscopic quantum tunneling of phase and some of the quantum phase slip theories. Finally, we will explore the recent observations pertaining to the superconductor-insulator transition.

The largest obstacle to studying one-dimensional superconductivity experimentally is the ability to produce homogenous wires. Chapter 3 will explain in detail how we fabricate the high quality MoGe nanowires for this dissertation using the molecular templating technique developed in Ref. [28]. The experimental measurements and low temperature equipment used will also be described.

The results are then divided between the subsequent three chapters. In Chapter 4, we present results on the quality of all of the MoGe wires and also provide a description of the properties of those wires that are superconducting as well as comparison with theory. The properties of the insulating wires are described in Chapter 5 and a model for their behavior that is based on recent theories is proposed. In Chapter 6, we bring all of these results together to clarify the observed superconductor-insulator transition in homogenous wires. Results on inhomogeneous wires are also discussed. The final chapter of this dissertation, Chapter 7, will be devoted to another set of measurements on superconducting nanobridges that are somewhat separate from the main work on the SIT and were performed along the way to concluding this work.

Reproduced with permission of the copyright owner. Further reproduction prohibited without permission.

1.1 References

[1] R. D. Parks and R. P. Groff, Phys. Rev. Lett. **18**, 342 (1967).

[2] W. A. Little, Phys. Rev. **156**, 398 (1967).

[3] T. K. Hunt and J. E. Mercereau, Phys. Rev. Lett. **18**, 551 (1967).

[4] W. W. Webb and R. J. Warburton, Phys. Rev. Lett. **20**, 461 (1968).

[5] V. L. Ginzburg and L. D. Landau, Zh. Eksperim. i. Teor. Fiz. **20**, 1064 (1950).

[6] J. S. Langer and V. Ambegaokar, Phys. Rev. **164**, 498 (1967).

[7] D. E. McCumber and B. I. Halperin, Phys. Rev. B **1**, 1054 (1970).

[8] D. E. McCumber, Phys. Rev. **172**, 427 (1968).

[9] J. E. Lukens, R. J. Warburton, and W. W. Webb, Phys. Rev. Lett. **25**, 1180 (1970).

[10] R. S. Newbower, M. R. Beasley, and M. Tinkham, Phys. Rev. B **5**, 864 (1972).

[11] N. Giordano, Phys. Rev. Lett. **61**, 2137 (1988).

[12] N. Giordano and E. R. Shuler, Phys. Rev. Lett. **63**, 2417 (1989).

[13] N. Giordano, Phys. Rev. B **41**, 6350 (1990).

[14] N. Giordano, Phys. Rev. B **43**, 160 (1991).

[15] A. J. Van Run, J. Romijn, and J. E. Mooij, Jpn. J. Appl. Phys. **26**, 1765 (1987).

[16] J. M. Duan, Phys. Rev. Lett. **74**, 5128 (1995).

[17] Y. Chang, Phys. Rev. B **54**, 9436 (1996).

[18] A. D. Zaikin, D. S. Golubev, A. van Otterlo, G. T. Zimányi, Phys. Rev. Lett. **78**, 1552 (1997).

[19] D. S. Golubev and A. D. Zaikin, Phys. Rev. B **64**, 014504 (2001).

[20] Y. Oreg and E. Demler, cond-mat/0106645 (2001).

Reproduced with permission of the copyright owner. Further reproduction prohibited without permission.

[21] H. P. Büchler, V. B. Geshkenbein, and G. Blatter, Phys. Rev. Lett. **92**, 067007 (2004).

[22] S. Sachdev, P. Werner, and M. Tryoer, Phys. Rev. Lett. **92**, 237003 (2004).

[23] S. Khlebnikov, Phys. Rev. Lett. **93**, 090403 (2004).

[24] C. N. Lau, N. Markovic, M. Bockrath, A. Bezryadin, and M. Tinkham, Phys. Rev. Lett. **87**, 217003 (2001).

[25] M. Zgirski, K. -P. Riikonen, V. Touboltsev, and K. Arutyunov, Nano Lett. **5**, 1029 (2005).

[26] F. Altomare, A. M. Chang, M. R. Melloch, Y. Hong, and C. W. Tu, cond-mat/0505772 (2005).

[27] F. Sharifi, A. V. Harzog, and R. C. Dynes, Phys. Rev. Lett. **71**, 428 (1993).

[28] A. Bezryadin, C. N. Lau, and M. Tinkham, Nature **404**, 971 (2000).

[29] A. Rogachev and A. Bezryadin, Appl. Phys. Lett. **83**, 512 (2003).

[30] Y. –J. Kim and K. J. Chang, cond-mat/9706032 (1997).

[31] Y. Oreg and A. M. Finkel'stein, Phys. Rev. Lett. **83**, 191 (1999).

[32] A. M. Finkel'stein, Physica B **197**, 636 (1994).

[33] A. M. Goldman and N. Markovic, Phys Today **51**, 39 (1998).

[34] M. Tinkham, *Introduction to Superconductivity*, 2nd ed. (McGraw-Hill, New York, 1996).

[35] G. Schön and A. D. Zaikin, Physics Reports **198**, 237 (1990).

[36] J. S. Penttilä, Ü. Parts, P. J. Hakonen, M. A. Paalanen, and E. B. Sonin, Phys. Rev. Lett. **82**, 1004 (1999).

[37] D. C. Ralph, C. T. Black, and M. Tinkham, Phys. Rev. Lett. **74**, 3241 (1995).

Reproduced with permission of the copyright owner. Further reproduction prohibited without permission.

[38] C. T. Black, D. C. Ralph, and M. Tinkham, Phys. Rev. Lett. **76**, 688 (1996).

[39] D. C. Ralph, C. T. Black, and M. Tinkham, Phys. Rev. Lett. **78**, 4087 (1997).

Reproduced with permission of the copyright owner. Further reproduction prohibited without permission.

Chapter 2

Physics of One-Dimensional Superconductors

As outlined in the introduction, much progress has been made in understanding how superconductivity is altered when dimensionality is reduced. In this chapter, we will examine in more detail some of the relevant theoretical predictions and corresponding experimental work that comprises the foundation for this dissertation. We shall begin with the topic of how thermal fluctuations in a one-dimensional wire can briefly destroy superconductivity and give rise to a measurable resistance. From there we will look at the additional effect of quantum fluctuations. Finally, we will consider observations in the thinnest wires produced in which superconductivity is extinguished altogether, with resistance increasing as temperature approaches zero.

2.1 Thermal fluctuations

2.1.1 Phase slips

Within the Ginzburg-Landau theory of superconductivity [1], the superconducting electrons are described by the complex order parameter

$$\psi = \psi_0 e^{i\phi} \tag{2.1}$$

Reproduced with permission of the copyright owner. Further reproduction prohibited without permission.

where ψ_0 is the magnitude of the order parameter and ϕ is its phase. This order parameter gives the local density of superconducting electrons, $n_S = |\psi|^2 = \psi_0^2$. In the absence of magnetic field, the supercurrent is driven by phase gradients, with a velocity

$$v_S = \frac{\hbar}{2m}\nabla\phi \tag{2.2}$$

where m is the mass of an electron. The supercurrent can then be written as

$$\begin{aligned} I_S &= J_S A \\ &= 2en_S v_S A \\ &= \frac{e\hbar}{m}\psi_0^2 \nabla\phi A \end{aligned} \tag{2.3}$$

where A is the cross sectional area of the wire. Due to conservation of current, $\psi_0^2\nabla\phi = \text{constant}$. Little [2] was the first to recognize that if $\psi_0 \to 0$ then the phase could undergo great changes. The process in which $\psi_0 \to 0$ and ϕ changes rapidly, or "slips", by 2π is known as a phase slip, as depicted in Fig. 2.1. In current biased wires, thermal fluctuations below the critical temperature, T_C, of a wire trigger phase slips, which lead to dissipation in the form of pulses of voltage, V, by the Josephson relation $2eV/\hbar = d\phi/dt$. This is the origin of resistance below T_C in a superconducting wire. If this dissipation were not present, any voltage applied across the wire would soon accelerate the supercurrent's velocity to the depairing velocity and superconductivity would be destroyed. The phase slips afford a way for the energy introduced by the voltage source to be dissipated as heat, rather than going into the kinetic energy of the supercurrent. Thus, a quasi stationary state in the wire is provided in which phase of 2π is removed from the system at the same rate as it is being introduced by the voltage source.

Reproduced with permission of the copyright owner. Further reproduction prohibited without permission.

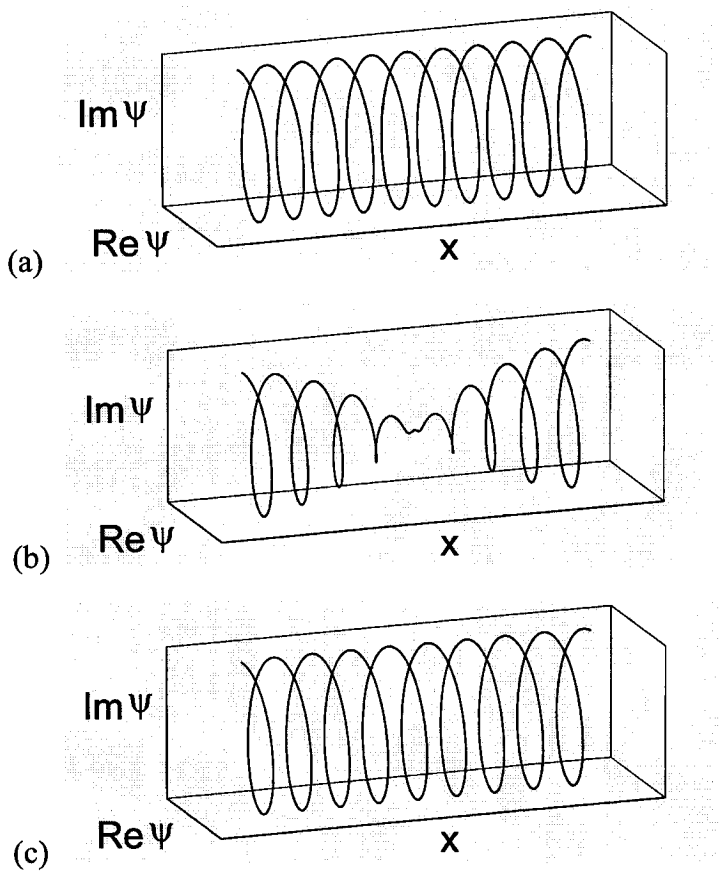

Figure 2.1: Depiction of a phase slip event. (a) Before the phase slip there are ten helical turns along the wire (phase difference of $10\times 2\pi$). (b) The order parameter goes to zero at some point along the wire, allowing the phase to slip by 2π. (c) After the phase slip a helical turn has been subtracted (phase difference of $9\times 2\pi$).

2.1.2 The free energy barrier

The thermal fluctuations must be able to provide a certain minimum amount of energy to the system in order to produce a phase slip. Langer and Ambegaokar [3] used time independent Ginzburg-Landau theory and found that the value of this minimum free energy barrier that separates two stationary states of a one-dimensional superconductor with a number of helices that are different by one turn is

Reproduced with permission of the copyright owner. Further reproduction prohibited without permission.

$$\Delta F(T) = \frac{8\sqrt{2}}{3}\frac{H_C^2(T)}{8\pi}A\xi(T) \tag{2.4}$$

where H_C is the thermodynamic critical field, A is the cross sectional area of the wire, and ξ is the Ginzburg-Landau coherence length. Their result is quite reasonable since, as discussed above, for a phase slip to occur a small section of the wire with length $\sim\xi$ must become normal (because $\psi_0 \to 0$). Therefore, besides a numerical factor, the free energy barrier Langer and Ambegaokar found is the condensation energy of this section. Recalling that near T_C

$$H_C(T) \propto \left(1-\frac{T}{T_C}\right) \quad \text{and} \quad \xi(T) \propto \left(1-\frac{T}{T_C}\right)^{-1/2} \tag{2.5}$$

we see that from Eq. 2.4

$$\Delta F(T) \propto \left(1-\frac{T}{T_C}\right)^{3/2} \tag{2.6}$$

The free energy barrier can then be written as

$$\Delta F(T) = \Delta F(0)\left(1-\frac{T}{T_C}\right)^{3/2} \tag{2.7}$$

and what we would like to do now is find an expression for $\Delta F(0)$ which is easily compared with experiment. To begin, we start with $\Delta F(0)$ as

$$\Delta F(0) = \frac{8\sqrt{2}}{3}\frac{H_C^2(0)}{8\pi}A\xi(0) \tag{2.8}$$

and eliminate $H_C^2(0)$. This is accomplished by recognizing that the Ginzburg-Landau coherence length is defined by

Reproduced with permission of the copyright owner. Further reproduction prohibited without permission.

$$\xi^2(T) = \frac{\hbar^2}{4m|\alpha(T)|} \tag{2.9}$$

where

$$\alpha(T) = -\frac{2e^2}{mc^2} H_C^2(T)\lambda_{eff}^2(T) \tag{2.10}$$

λ_{eff} is the effective penetration depth, and c is the speed of light. At $T = 0$ we have then

$$\begin{aligned} \xi^2(0) &= \frac{\hbar^2}{4m\frac{4e^2}{2mc^2} H_C^2(0)\lambda_{eff}^2(0)} \\ &= \frac{\hbar^2 c^2}{8e^2 H_C^2(0)\lambda_{eff}^2(0)} \end{aligned} \tag{2.11}$$

so

$$H_C^2(0) = \frac{\hbar^2 c^2}{8e^2\xi^2(0)\lambda_{eff}^2(0)} \tag{2.12}$$

We can now use this equality in Eq. 2.8 to eliminate $H_C^2(0)$

$$\begin{aligned} \Delta F(0) &= \frac{8\sqrt{2}}{3}\frac{H_C^2(0)}{8\pi} A\xi(0) \\ &= \frac{8\sqrt{2}}{3}\frac{1}{8\pi}\frac{\hbar^2 c^2}{8e^2\xi^2(0)\lambda_{eff}^2(0)} A\xi(0) \\ &= \frac{\sqrt{2}}{3}\frac{A}{8\pi}\frac{\hbar^2 c^2}{e^2\xi(0)\lambda_{eff}^2(0)} \end{aligned} \tag{2.13}$$

The next step is to eliminate the effective penetration depth term. In the dirty limit, which is valid for $Mo_{0.79}Ge_{0.21}$ since $3\ \text{Å} \approx \ell \ll \lambda_L(0) \approx 18.5\ \text{nm}$, where λ_L is the London penetration depth, we have

$$\lambda_{eff}^2(T) = \lambda_L^2(T)\frac{\xi_0}{J(0,T)\ell} \tag{2.14}$$

Reproduced with permission of the copyright owner. Further reproduction prohibited without permission.

where ξ_0 is the Pippard (or BCS) coherence length and ℓ is the mean free path. Therefore

$$\frac{1}{\lambda_{eff}^2(0)} = \frac{1}{\lambda_L^2(0)} \frac{J(0,0)\ell}{\xi_0} = \frac{1}{\lambda_L^2(0)} \frac{\ell}{\xi_0} \tag{2.15}$$

where in the last step $J(0,T)$, the real space Fourier transform of the BCS kernel $K(0,T)$ for the nonlocal relation between $\vec{J}$ and $\vec{A}$ evaluated at $\vec{R} = 0$, is simply equal to one at $T = 0$. At this point we can eliminate the effective penetration depth

$$\begin{aligned} \Delta F(0) &= \frac{\sqrt{2}}{3} \frac{A}{8\pi} \frac{\hbar^2 c^2}{e^2 \xi(0) \lambda_{eff}^2(0)} \\ &= \frac{\sqrt{2}}{3} \frac{A}{8\pi} \frac{\hbar^2 c^2}{e^2 \xi(0)} \frac{1}{\lambda_L^2(0)} \frac{\ell}{\xi_0} \end{aligned} \tag{2.16}$$

but now we must rid ourselves of the London penetration depth. This has the value

$$\lambda_L^2(T) = \frac{mc^2}{4\pi n_s(T) e^2} \tag{2.17}$$

so

$$\frac{1}{\lambda_L^2(0)} = \frac{4\pi n_s(0) e^2}{mc^2} = \frac{4\pi n e^2}{mc^2} \tag{2.18}$$

where n is the density of normal electrons. At zero temperature all electrons are paired so we were able to use $n = n_S(0)$ in the second equality of Eq. 2.18. The free energy barrier then becomes

Reproduced with permission of the copyright owner. Further reproduction prohibited without permission.

$$\begin{aligned}\Delta F(0) &= \frac{\sqrt{2}}{3}\frac{A}{8\pi}\frac{\hbar^2 c^2}{e^2\xi(0)}\frac{1}{\lambda_L^2(0)}\frac{\ell}{\xi_0} \\ &= \frac{\sqrt{2}}{3}\frac{A}{8\pi}\frac{\hbar^2 c^2}{e^2\xi(0)}\frac{\ell}{\xi_0}\frac{4\pi n e^2}{mc^2} \\ &= \frac{\sqrt{2}}{3}\frac{A}{2}\frac{\hbar^2}{e^2\xi(0)}\frac{\ell}{\xi_0}\frac{ne^2}{m}\end{aligned} \tag{2.19}$$

From BCS theory

$$\xi_0 = \frac{\hbar v_F}{\pi\Delta(0)} \tag{2.20}$$

where v_F is the Fermi velocity and $\Delta(0)$ is the superconducting gap at zero temperature so

$$\begin{aligned}\Delta F(0) &= \frac{\sqrt{2}}{3}\frac{A}{2}\frac{\hbar^2}{e^2\xi(0)}\frac{\ell}{\xi_0}\frac{ne^2}{m}\frac{\pi\Delta(0)}{\hbar v_F} \\ &= \frac{\sqrt{2}}{3}\frac{\pi\hbar}{2e^2}\frac{A}{\xi(0)}\frac{ne^2\ell}{mv_F}\Delta(0)\end{aligned} \tag{2.21}$$

For the final phase of our derivation we need to remember that from Drude theory the force on an electron in a normal metal is modeled as

$$m\frac{dv}{dt} = eE - \frac{mv}{\tau} \tag{2.22}$$

where v is the electron velocity, E is the electric field, and τ is the elastic scattering time. In the steady state $dv/dt = 0$ so we have

$$eE = \frac{mv}{\tau} \tag{2.23}$$

from which we get Ohm's law

$$j = nev = \frac{ne^2\tau}{m}E \equiv \sigma E \tag{2.24}$$

Reproduced with permission of the copyright owner. Further reproduction prohibited without permission.

From the conductivity we get the resistivity

$$\sigma = \frac{ne^2\tau}{m} = \frac{ne^2\ell}{mv_F} = \frac{1}{\rho} \tag{2.25}$$

which we now use in Eq. 2.21

$$\begin{aligned} \Delta F(0) &= \frac{\sqrt{2}}{3}\frac{\pi\hbar}{2e^2}\frac{A}{\xi(0)}\frac{ne^2\ell}{mv_F}\Delta(0) \\ &= \frac{\sqrt{2}}{3}\frac{\pi\hbar}{2e^2}\frac{A}{\xi(0)}\frac{1}{\rho}\Delta(0) \end{aligned} \tag{2.26}$$

Finally, we recognize that the BCS gap at zero temperature is $\Delta(0) = (\pi/e^{\gamma})k_B T_C \simeq 1.76 k_B T_C$, where $\gamma = 0.577$ is Euler's constant, and we arrive at

$$\begin{aligned} \Delta F(0) &= \frac{\sqrt{2}}{3}\frac{\pi\hbar}{2e^2}\frac{A}{\xi(0)}\frac{1}{\rho}\frac{\pi}{e^{\gamma}}k_B T_C \\ &= \frac{\sqrt{2}\pi}{3e^{\gamma}}\frac{R_Q}{R_N}\frac{L}{\xi(0)}k_B T_C \end{aligned} \tag{2.27}$$

where in the last step we made use of the usual relations for the quantum resistance for Cooper pairs, R_Q, and the normal resistance of the wire, R_N,

$$R_Q = \frac{\pi\hbar}{2e^2} \qquad \text{and} \qquad R_N = \frac{\rho L}{A} \tag{2.28}$$

where L is the length of the wire. As a final simplification we define a parameter, c [4], which will allow us to express the free energy barrier plainly as

$$\begin{aligned} \Delta F(T) &= \Delta F(0)\left(1 - \frac{T}{T_C}\right)^{3/2} \\ &= ck_B T_C\left(1 - \frac{T}{T_C}\right)^{3/2} \end{aligned} \tag{2.29}$$

where

Reproduced with permission of the copyright owner. Further reproduction prohibited without permission.

$$c \equiv \frac{\sqrt{2}\pi}{3e^{\gamma}} \frac{R_Q}{R_N} \frac{L}{\xi(0)} \simeq 0.83 \frac{R_Q}{R_N} \frac{L}{\xi(0)} \tag{2.30}$$

2.1.3 LAMH resistance

The phase slips induced by thermal fluctuations are more commonly called thermally activated phase slips (TAPS) because the fluctuations thermally activate the system over the free energy barrier, which changes the phase by 2π, thus providing the phase slip (Fig. 2.2(a)). The resistance then should have an activated dependence form ($R \propto \exp\left[-\Delta F(T)/k_B T\right]$), which, as we will see shortly, is the case. To derive the resistance from TAPS we must first include the effect of the bias current in the wire. This has the consequence of "tilting" the free energy landscape (Fig. 2.2(b)), making phase slips in one direction more preferable to the other by lowering the barrier in that direction and raising it in the other. The amount the free energy is raised and lowered, δF, is the work done by the source during a phase slip event

$$\delta F = \int IV dt \tag{2.31}$$

where I is current. Using the Josephson relation, we can write this as

$$\begin{aligned} \delta F &= \int_0^{2\pi} IV \frac{\hbar}{2eV} d\phi \\ &= \frac{hI}{2e} \end{aligned} \tag{2.32}$$

The free energy barriers for "positive" and "negative" phase slips are then

$$\begin{aligned} \Delta F_+ &= \Delta F + (\delta F/2) = \Delta F + (hI/4e) \\ \Delta F_- &= \Delta F - (\delta F/2) = \Delta F - (hI/4e) \end{aligned} \tag{2.33}$$

Reproduced with permission of the copyright owner. Further reproduction prohibited without permission.

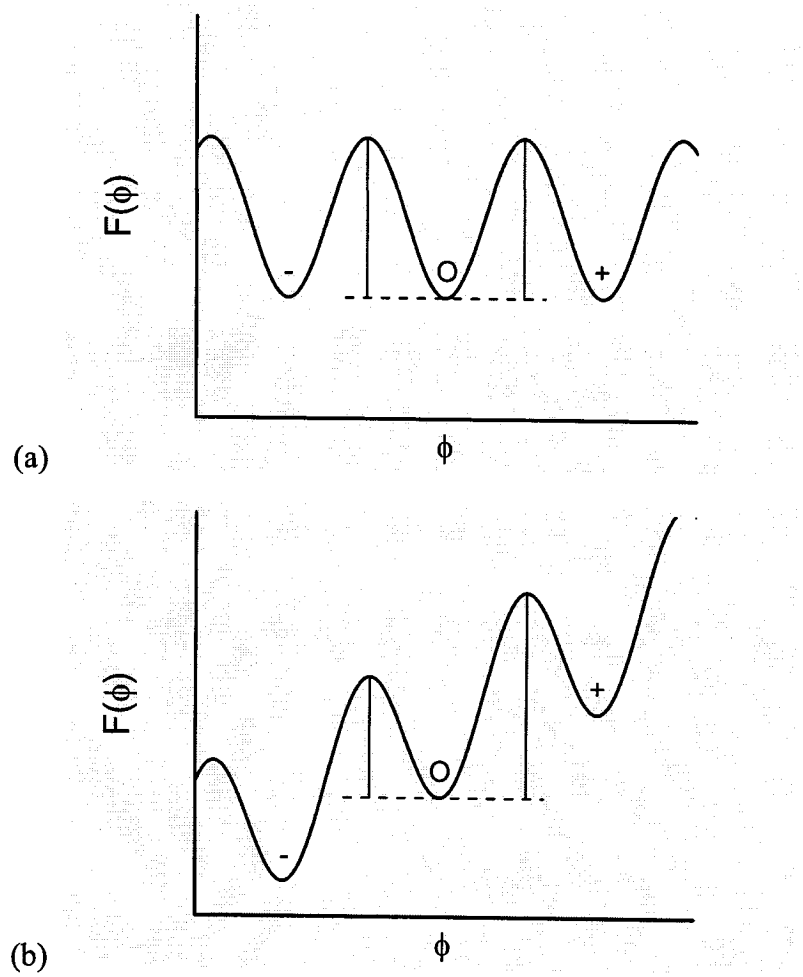

Figure 2.2: Free energy diagrams. (a) When no bias current is applied, the system, at state O, has equal probability to be thermally activated to state + and state -, since the barrier heights are the same. "Positive" and "negative" phase slips occur at equal rates. (b) A bias current tilts the free energy diagram, introducing a change in the barrier heights. The system is more likely to be thermally activated to state -, resulting in a net phase slip rate and, therefore, to a measurable resistance.

If the system attempts to go over these barriers with a frequency Ω, it will be successfully excited with a probability set by the Boltzman factors $\exp\left(-\Delta F_{\pm}/k_B T\right)$. The phase of the system will then be lost at a rate

Reproduced with permission of the copyright owner. Further reproduction prohibited without permission.

$$\begin{aligned}\frac{d\phi}{dt} &= \Omega\left\{\exp\left[-\frac{\Delta F_-}{k_BT}\right]-\exp\left[-\frac{\Delta F_+}{k_BT}\right]\right\} \\ &= \Omega\left\{\exp\left[-\frac{\Delta F-(hI/4e)}{k_BT}\right]-\exp\left[-\frac{\Delta F+(hI/4e)}{k_BT}\right]\right\} \\ &= \Omega e^{-\Delta F/k_BT}\left\{\exp\left[\frac{hI/4e}{k_BT}\right]-\exp\left[-\frac{hI/4e}{k_BT}\right]\right\} \\ &= 2\Omega e^{-\Delta F/k_BT}\sinh\left(\frac{hI}{4ek_BT}\right)\end{aligned} \tag{2.34}$$

Now, we can derive the resistance from this by simply using the Josephson relation to get the resistive voltage from thermal phase slips

$$\begin{aligned}\frac{d\phi}{dt} &= \frac{2eV}{\hbar} = 2\Omega e^{-\Delta F/k_BT}\sinh\left(\frac{hI}{4ek_BT}\right) \\ V &= \frac{\hbar\Omega}{e}e^{-\Delta F/k_BT}\sinh\left(\frac{hI}{4ek_BT}\right)\end{aligned} \tag{2.35}$$

and then differentiate

$$\begin{aligned}\frac{dV}{dI} &= \frac{d}{dI}\left[\frac{\hbar\Omega}{e}e^{-\Delta F/k_BT}\sinh\left(\frac{hI}{4ek_BT}\right)\right] \\ &= \frac{h}{4e^2}\frac{\hbar\Omega}{k_BT}e^{-\Delta F/k_BT}\cosh\left(\frac{hI}{4ek_BT}\right)\end{aligned} \tag{2.36}$$

When $I \ll 4ek_BT/h \simeq 13.4$ nA/K the hyperbolic cosine is essentially equal to one and the zero-bias resistance is

$$R = R_Q\frac{\hbar\Omega}{k_BT}e^{-\Delta F/k_BT} \tag{2.37}$$

where $R_Q = h/(2e)^2$ is the quantum resistance for Cooper pairs. We should note that upon comparing Eqs. 2.36 and 2.37, at a fixed temperature the differential resistance at all bias is simply the zero-bias resistance at that temperature multiplied by the hyperbolic

Reproduced with permission of the copyright owner. Further reproduction prohibited without permission.

cosine factor ($dV(I,T)/dI = R(T)\cosh(hI/4ek_BT)$). We will use this fact later in Chapter 4 when looking at differential resistance data.

When Langer and Ambegaokar formulated their theory they assumed the attempt frequency to simply be the inverse elastic scattering time multiplied by the number of electrons in the wire. Using time dependent Ginzburg-Landau theory, it was subsequently discovered by McCumber and Halperin [5] that, while Langer and Ambegaokar's result for the free energy barrier was correct, the attempt frequency is more properly given by

$$\Omega = \frac{L}{\xi}\sqrt{\frac{\Delta F}{k_B T}}\frac{1}{\tau_S} \tag{2.38}$$

where

$$\tau_S = \frac{\pi\hbar}{8k_B(T_C - T)} \tag{2.39}$$

is the Ginzburg-Landau time, which is the characteristic relaxation rate of the superconductor in time dependent Ginzburg-Landau theory. In Eq. 2.38, $1/\tau_S$ sets the scale for Ω, L/ξ is the number of independent wire segments in which phase slips can attempt to occur, and $\sqrt{\Delta F/k_B T}$ accounts for overlap of these segments. Combining Eqs. 2.29, 2.37, 2.38, and 2.39 allows us to write the full temperature dependence of the Langer-Ambegaokar-McCumber-Halperin (LAMH) resistance as

$$R_{LAMH}(T) = \frac{8L\sqrt{c}}{\pi\xi(0)}R_Q\left(\frac{T}{T_C}\right)^{-3/2}\left(1-\frac{T}{T_C}\right)^{9/4}\exp\left[-c\frac{T_C}{T}\left(1-\frac{T}{T_C}\right)^{3/2}\right] \tag{2.40}$$

where c is defined in Eq. 2.30. Thus, we have a formula for the LAMH resistance which is easily compared to experiment as L and R_N are known from scanning electron

Reproduced with permission of the copyright owner. Further reproduction prohibited without permission.

microscope pictures of the wire and electrical measurements, respectively. To compare Eq. 2.40 to data only two fitting parameters need to be used, namely T_C and $\xi(0)$.

2.1.4 Experimental verification

In the early 1970s Lukens, Warburton, and Webb [6] and Newbower, Beasley, and Tinkham [7] reported on separate measurements of single crystal tin "whiskers" (Fig. 2.3) with diameters ~ 0.5 μm. They both found that the resistance below T_C of the wire is well described by the LAMH theory. However, both reports do show some deviation from the theory as $T \to T_C$ but this is to be expected, as the theory is only valid when $\Delta F \gg k_B T$, whereas $\Delta F \to 0$ as $T \to T_C$. While the agreement between the LAMH theory and the data of Newbower, Beasley, and Tinkham is good, they further found that they could improve their fits by including a parallel normal channel such that $R^{-1}(T) = R_N^{-1}(T) + R_{LAMH}^{-1}(T)$.

2.2 Quantum fluctuations

The interest in how fluctuations destroy superconductivity in wires stems from the very basic question of the stability of circulating supercurrents. Above, we have seen how thermal fluctuations can give rise to the reduction of the phase gradient, and hence to a decrease in supercurrent, since $I_S \propto \nabla\phi$. The question then remains, can we stabilize the supercurrent lifetime in a loop by simply lowering the temperature enough that the rate of thermally activated phase slips becomes negligible? As fabrication methods continued to

Reproduced with permission of the copyright owner. Further reproduction prohibited without permission.

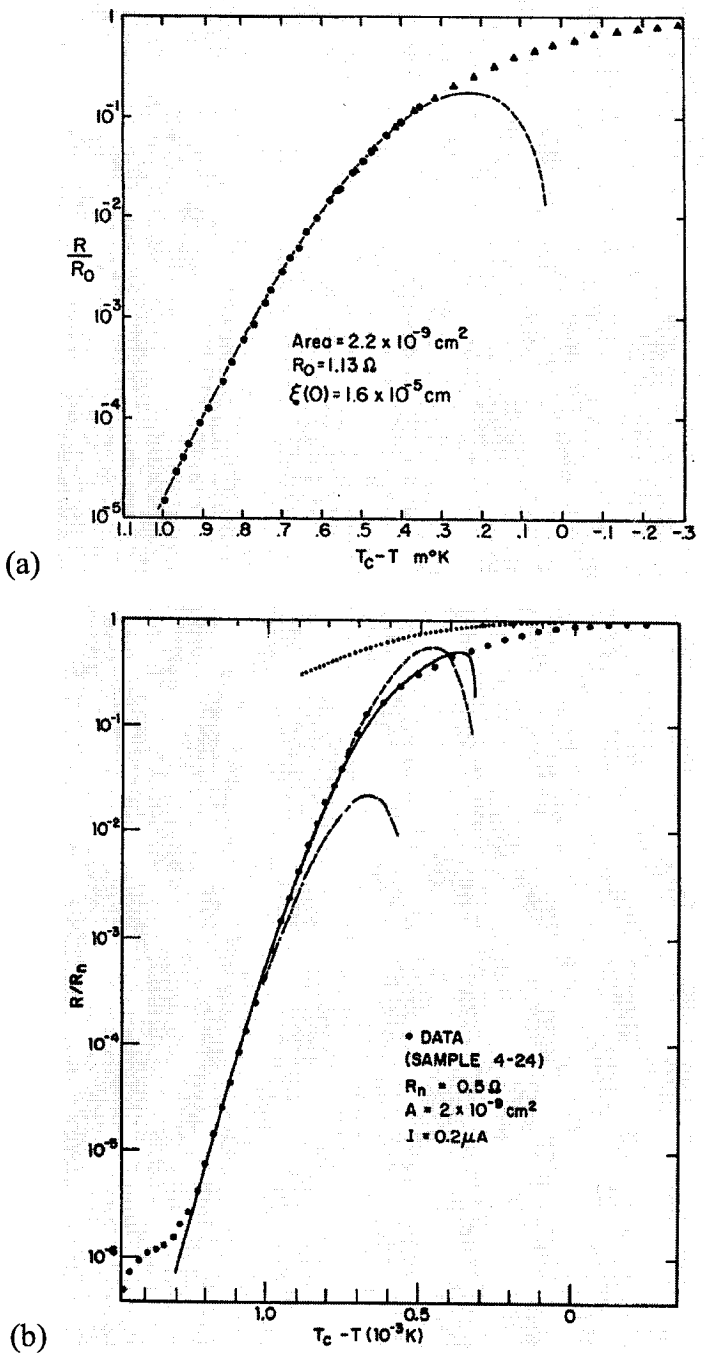

Figure 2.3: (a) Data (symbols) from Lukens Warburton, and Webb [6] and their fit to LAMH theory (dashed line). (b) Data (symbols) from Newbower, Beasley, and Tinkham [7]. The various fits are to LAMH theory (dashed line), LAMH theory with parallel normal channel (solid line), LAMH theory with different attempt frequency (dot-dashed line), and Tucker-Halperin theory (dotted line). The deviation at lowest temperatures is attributed to contact effects.

Reproduced with permission of the copyright owner. Further reproduction prohibited without permission.

advance and wires of increasingly smaller cross section were able to be produced, new effects were discovered that indicate the answer to this question *in general* is "no".

2.2.1 The Giordano model

In the late 1980's, Giordano [8] observed a crossover in the resistance of one-dimensional In wires with diameters ~ 50 nm fabricated by a step-edge technique, from the LAMH behavior to a slower variation with decreasing temperature (Fig. 2.4). These resistance "tails" were attributed to the macroscopic quantum tunneling of phase (MQT) in which the state of the system is not thermally activated *over* the free energy barrier but rather tunnels *through* the barrier [9]. At the time, no quantitative theory for MQT in wires existed for comparison with his data. So Giordano derived an expression for the MQT rate in a wire in analogy with the well known theory of MQT in other systems, namely Josephson junctions [10]. Both a wire and a Josephson junction can be described as the motion of a "particle" in a tilted washboard potential so his reasoning is logical.

The time dependent Ginzburg-Landau theory, from which the LAMH theory was derived, predicts a purely diffusive time dependence for the order parameter. Hence, in terms of a particle in a tilted washboard potential, the LAMH theory is in the limit of strong damping. Giordano used this same limit in his derivation and found that the rate for MQT is

$$\Gamma_{MQT} = 16\sqrt{3}\alpha_0^4 \left(\frac{V_b}{\hbar\tau_S}\right)^{1/2} \exp\left(-\frac{\pi\beta\tau_S V_b}{6\sqrt{2}\hbar}\right) \tag{2.41}$$

where α_0 is the damping factor, V_b is the barrier height, and β is a constant of order unity that reflects the uncertainty in knowing the distance the particle tunnels under the barrier. Giordano reasonably argued that $V_b = \Delta F$ and that a factor of L/ξ should be

Reproduced with permission of the copyright owner. Further reproduction prohibited without permission.

inserted to account for the number of independent positions at which MQT could occur so

$$\Gamma_{MQT} = 16\sqrt{3}\alpha_0^4 \frac{L}{\xi}\left(\frac{\Delta F}{\hbar\tau_S}\right)^{1/2} \exp\left(-\frac{\pi\beta\tau_S\Delta F}{6\sqrt{2}\hbar}\right) \tag{2.42}$$

from which he arrived at an expression for the resistance due to MQT as

$$R_{MQT} = R_Q \frac{h}{k_B T} 16\sqrt{3}\alpha_0^4 \frac{L}{\xi}\left(\frac{\Delta F}{\hbar\tau_S}\right)^{1/2} \exp\left(-\frac{\pi\beta\tau_S\Delta F}{6\sqrt{2}\hbar}\right) \tag{2.43}$$

If we now define $a \equiv 32\sqrt{3}\pi\alpha_0^4$ and $b \equiv \pi\beta/6\sqrt{2}$ then Eq. 2.43 can be written as

$$R_{MQT} = aR_Q \frac{\hbar}{k_B T}\frac{L}{\xi}\left(\frac{\Delta F}{\hbar/\tau_S}\right)^{1/2} \frac{1}{\tau_S} \exp\left(-\frac{b\Delta F}{\hbar/\tau_S}\right) \tag{2.44}$$

Comparison of Eq. 2.44 with Eqs. 2.37 and 2.38 shows that, apart from the constants a and b, the resistance from macroscopic quantum tunneling of phase that Giordano arrived at is equivalent to the thermally activated phase slip resistance but with $\Delta F/k_B T$ replaced with $\Delta F/(\hbar/\tau_S)$. This is a reasonable result as the characteristic energy scale for thermal activation should be $k_B T$ whereas for quantum tunneling one would guess from the uncertainty principle it should be $\Delta E = \hbar/\Delta t = \hbar/\tau_S$. However, because these two energy scales have different temperature dependences the resistance from MQT that is predicted by Eq. 2.44 decreases more slowly with temperature than that from TAPS. This is easily seen by comparing the arguments of the exponential functions in Eqs. 2.40 and 2.44, which for R_{LAMH} goes as $(T_C/T)(1-T/T_C)^{3/2}$ and for R_{MQT} as $(1-T/T_C)^{1/2}$. Therefore, while the LAMH theory predicts a truly superconducting state with $R = 0$ at $T = 0$, resistance due to MQT survives at $T = 0$.

Reproduced with permission of the copyright owner. Further reproduction prohibited without permission.

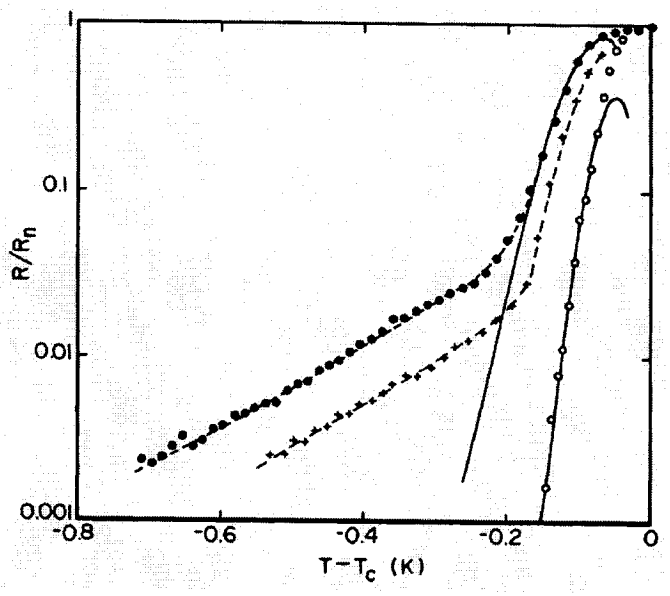

Figure 2.4: Data (symbols) from Giordano [8]. Wire diameters are 410 Å (•), 505 Å (+), and 720 Å (○). The solid curves are fits to LAMH theory alone whereas the dashed curves include the effect of MQT. MQT is only observed in thinnest wires.

Giordano fit his data, as shown in Fig. 2.4, with the function $R(T) = R_{LAMH}(T) + R_{MQT}(T)$ to include the effects of both thermally activated phase slips and macroscopic quantum tunneling of phase and obtained good agreement, seemingly justifying his model. One drawback to this agreement however, as pointed out by Duan [11], is that since $\Delta F \propto A$ one would expect that the $R(T)$ curves for wires of different cross sectional area would show different slopes in the $\log R(T)$ vs. T representation that Giordano presented. Instead, the data for wires with diameters 410 Å and 505 Å have the same slope at low temperature, which Duan argued was due to granularity of the wires and Josephson weak links. Giordano himself reports observing grains in the wires of size 100-200 Å and that in fitting the data the free energy barrier

Reproduced with permission of the copyright owner. Further reproduction prohibited without permission.

had to be reduced by a factor ~ 4, which he admits may be due to inhomogeneities, or "weak spots". Considering these facts, it becomes doubtful that the deviation from LAMH behavior Giordano observed was actually entirely due to MQT. Still, it can be argued that his derivation for R_{MQT} and at least the appearance that MQT in one-dimensional wires could be observed were valuable in that they produced a resurgence of interest in a topic that was nearly dormant for over a decade.

2.2.2 Quantum phase slip theories

The interest that was generated by Giordano's results naturally lead to further examination of the effect that quantum tunneling of phase, or quantum phase slips (QPS), has on the behavior of one-dimensional superconducting wires. One of the first microscopic theories of QPS that appeared after Giordano's work was by Chang [12]. Using a functional integral approach he concluded that the resistance from QPS was

$$R_{Chang} = R_Q \frac{h}{k_B T} \frac{1}{3\pi\sqrt[4]{18}} \frac{L}{\xi} \left(\frac{\Delta F}{\hbar/\tau_S} \right)^{1/2} \frac{1}{\tau_S} \exp\left(-\frac{\pi}{27\sqrt{2}} \frac{\Delta F}{\hbar/\tau_S} \right) \tag{2.45}$$

By comparing with Eq. 2.44, aside from the numerical factors in the exponent and pre-exponent, Eq. 2.45 is identical to the result Giordano obtained. Not surprisingly, Chang was able to fit Giordano's data with his theory, but due to the problems already discussed about the data the validity of Chang's work remains unclear.

At about the same time, Duan addressed the role that electromagnetic fields have on the occurrence of QPS [11]. Since the typical time duration for QPS at zero temperature is $\tau_S(0) = \pi\hbar/8k_B T_C \approx \hbar/\Delta(0)$ and the gap is usually of the order 1 meV, the corresponding frequency of the voltage pulse produced by the QPS is of the order 1 THz.

Reproduced with permission of the copyright owner. Further reproduction prohibited without permission.

The dissipation of electromagnetic signals at such high frequencies in a superconductor is the same as that in the normal state, so the effect of dissipation on QPS needs to be examined. Duan found that when dissipation is included, the rate of QPS is reduced by a factor of $\exp(-A_{Duan}/\alpha)$, where $A_{Duan} = (\pi/4)\ln\ln(I_C/I)$ and α is the fine structure constant. For realistic currents, $A_{Duan} \sim 1$ and so the reduction factor is $\sim \exp(-137)$, effectively resulting in a complete suppression of QPS by the dissipative environment. This result is valid when

$$\frac{2A}{\lambda_{eff}^2} \ln \frac{I_C}{I} \geq 1 \tag{2.46}$$

which is easily satisfied for wires with $A \sim \lambda_{eff}^2$. However, for the wires fabricated in this work, $A/\lambda_{eff}^2 \sim (10\,\text{nm})^2/(100\,\text{nm})^2 \sim 1/100$ so Eq. 2.46 is only satisfied when the measurement current is $I \leq I_C \exp(-50)$, which is not technically feasible. While not applicable to our wires, Duan's work does show that including the effect of the electromagnetic environment can have a strong influence on the rate of QPS.

The theory outlined by Zaikin, et al. [13], and Golubev and Zaikin [14] also examines the interplay between QPS and their environment. This work takes a more microscopic approach than Duan's phenomenological time dependent Ginzburg-Landau formalism and finds that QPS are not suppressed by dissipation to the extent found by Duan. The calculation relies on an effective action technique that includes the action of condensation energy and dissipative currents in the QPS "core", S_{core}, as well as the electromagnetic fields outside this region, S_{out} [13]. The total QPS action, $S_{GZ} = S_{core} + S_{out}$, was found to be [14]

Reproduced with permission of the copyright owner. Further reproduction prohibited without permission.

$$S_{GZ} = A_{GZ} \frac{R_Q}{R_N} \frac{L}{\xi} \tag{2.47}$$

where A_{GZ} is a numerical constant of order unity. The QPS rate is then proportional to $\exp(-S_{GZ}) = \exp\left[-A_{GZ} R_Q L / R_N \xi\right]$ (note that units where $\hbar = 1$ were used in the theory so the rate is written here proportional to $\exp(-S_{GZ})$ as opposed to the usual $\exp(-S_{GZ}/\hbar)$). Although it could not be determined exactly, the exponential prefactor was calculated up to a numerical constant B_{GZ} to be $B_{GZ}\left(R_Q/R_N\right)\left(L^2/\xi^4\right)D$, where $D = v_F \ell/3$ is the diffusion constant. Combining this with the exponential factor gives the QPS rate as

$$\Gamma_{GZ} = B_{GZ} D \frac{R_Q}{R_N} \frac{L^2}{\xi^4} \exp\left(-\frac{A_{GZ} R_Q L}{R_N \xi}\right) \tag{2.48}$$

It is easily seen from Eq. 2.48 that for realistic wires, such as those that we study with $R_N \sim R_Q$, $L \sim 100\,\text{nm}$, $\xi = 7\,\text{nm}$ and $D = 0.5\,\text{cm}^2/\text{s}$ [15], the typical time between QPS predicted by this theory can be $t_{GZ} = \Gamma_{GZ}^{-1} \sim 0.1\,\text{ns}$, demonstrating the difference in results between this work and that of Duan.

2.2.3 Experimental comparison

Lau *et al.* [4] recently performed measurements on MoGe nanowires that had resistive transitions that could not be fully accounted for by the classical LAMH theory (Fig. 2.5). Their wires were fabricated by a molecular templating technique [16], which will be discussed in detail in Chapter 3, and had lengths, widths, and thicknesses of 0.1-1 μm, 10-22 nm, and 4-5 nm, respectively. It was found that they could achieve reasonable agreement between their data and theory if they included a slightly modified version of

Reproduced with permission of the copyright owner. Further reproduction prohibited without permission.

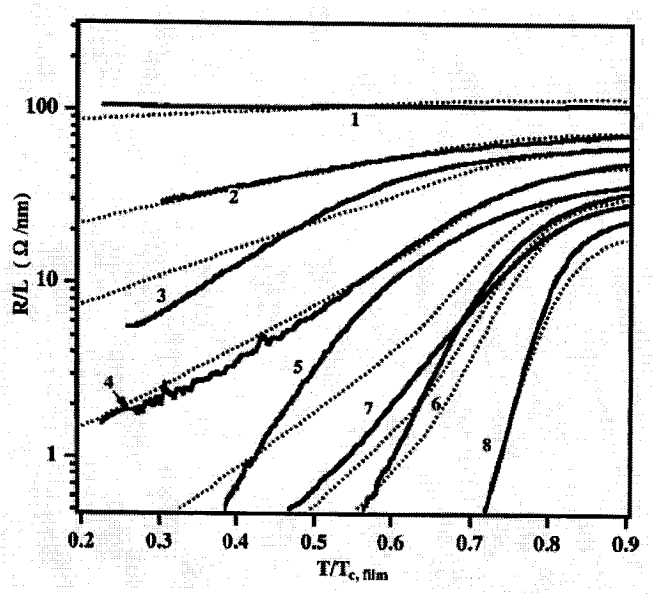

Figure 2.5: Data (solid lines) from Lau *et al.* [4] with fits (dotted lines) to Giordano's model of MQT (Eq. 2.44). The values $a = 7.2$ and $b = 1.3$ were used to fit the entire family of curves.

Giordano's model of MQT using the fitting function $R^{-1} = R_N^{-1} + \left(R_{LAMH} + R_{MQT}^{*}\right)^{-1}$ where $R_{MQT}^{*} = \left[k_B T/(\hbar/\tau_S)\right] R_{MQT}$. Since Giordano's model is heuristic, the modification is not made to the exponential but in the prefactor, and $\left[k_B T/(\hbar/\tau_S)\right]$ only varies between 0.1 and 3.5 throughout the temperature range of their fits, this change is not particularly significant and only mentioned here for completeness. Lau *et al.*'s entire family of data curves was best fit using $a = 7.2$ and $b = 1.3$, both of which are of order unity as they should be. Due to these facts, Lau *et al.* concluded that they were indeed observing the effects of QPS. They also argued that their wires did not suffer from granularity as Giordano's may have because: (i) MoGe is an amorphous material known to form continuous films down to 1 nm [15], (ii) the measured resistivity of their wires is very

Reproduced with permission of the copyright owner. Further reproduction prohibited without permission.

close to the bulk value, and (iii) TEM images of similarly fabricated wires on holey carbon grids showed no indication of granularity.

In her thesis [17], Lau also compared the same experimental results to the microscopic theory of Golubev and Zaikin discussed above [13-14]. The rate calculated in the microscopic theory was done at zero bias current and zero temperature. To derive an expression for the full temperature dependence of the QPS resistance from this rate, Lau began by writing the action as $S_{GZ} = A_{GZ}\left(\Delta F/E_{ch}\right)$, where E_{ch} is some characteristic energy, using Eqs. 2.27, 2.30, and 2.47. She then proceeded as before in the case of the LAMH theory (in analogy to Eqs. 2.31-37) and included the effect of current tilting the free energy landscape to arrive at

$$R_{GZ} = R_Q \frac{\hbar}{E_{ch}} B_{GZ} \frac{R_Q}{R_N} \frac{L^2}{\xi^4} D \exp\left(-\frac{A_{GZ} R_Q L}{R_N \xi}\right) \tag{2.49}$$

The characteristic energy was chosen to be $E_{ch} = \hbar/\tau_0 = \hbar D/\xi^2$ and so

$$R_{GZ} = B_{GZ} R_Q \frac{R_Q}{R_N}\left(\frac{L}{\xi}\right)^2 \exp\left(-\frac{A_{GZ} R_Q L}{R_N \xi}\right) \tag{2.50}$$

Finally, by noting that the only term in Eq. 2.50 that is temperature dependent is the coherence length (Eq. 2.5), Lau arrived at an expression for the full temperature dependence of R_{GZ} as

$$R_{GZ}(T) = B_{GZ} R_Q \frac{R_Q}{R_N}\left[\frac{L}{\xi(0)}\right]^2 \left(1-\frac{T}{T_C}\right) \exp\left[-\frac{A_{GZ} R_Q L}{R_N \xi(0)}\left(1-\frac{T}{T_C}\right)^{1/2}\right] \tag{2.51}$$

The temperature dependence of the exponential factor in Eq. 2.51 is the same as that found by Giordano (Eq. 2.44) and Chang (Eq. 2.45), connecting back to the previous

Reproduced with permission of the copyright owner. Further reproduction prohibited without permission.

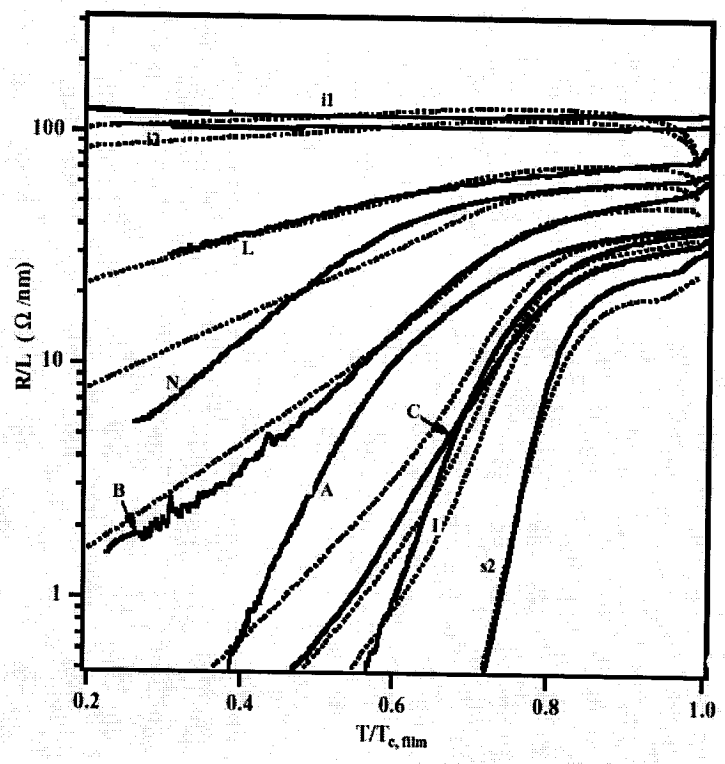

Figure 2.6: Data (solid lines) from Lau [17] with fits (dotted lines) to the microscopic model of QPS (Eq. 2.51). The values $A_{GZ} = 0.52$ and $B_{GZ} = 1.4$ were used to fit the entire family of curves.

work. Not too surprisingly then, Lau was able to fit her data to the microscopic theory using the fitting function $R^{-1} = R_N^{-1} + \left(R_{LAMH} + R_{GZ}\right)^{-1}$ (Fig. 2.6). The entire family of data curves was best fit using $A_{GZ} = 0.52$ and $B_{GZ} = 1.4$, again both of order unity.

A reasonable agreement with the microscopic theory was also observed recently in experiments on 10 μm long Al wires by Zgirski *et al.* [18]. They used a novel technique in which relatively thick ($\sqrt{A} \sim 75$ nm) wires fabricated by standard e-beam lithography were thinned by ion beam sputtering. Through repeated cycles of measurement and *ex situ* thinning they were able to observe the appearance of QPS as cross sectional area was decreased (Fig. 2.7(a)). The onset of QPS occurred when

Reproduced with permission of the copyright owner. Further reproduction prohibited without permission.

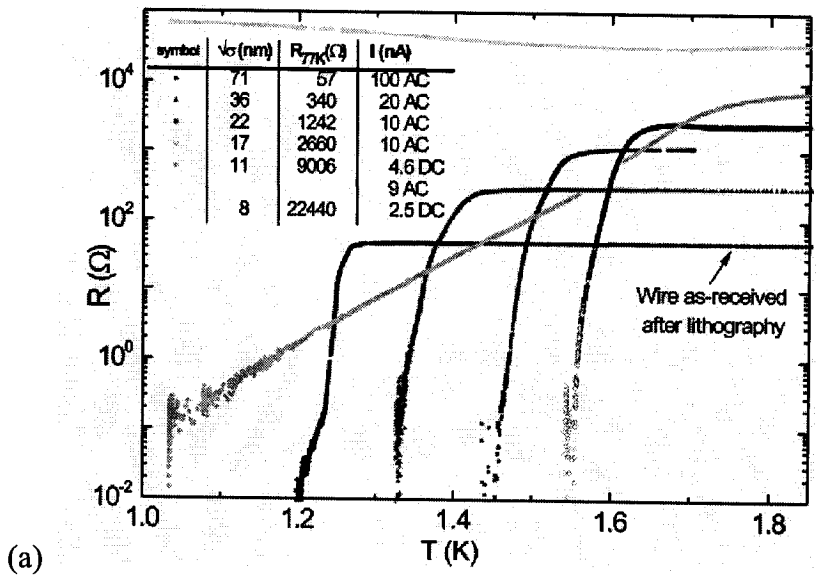

(a)

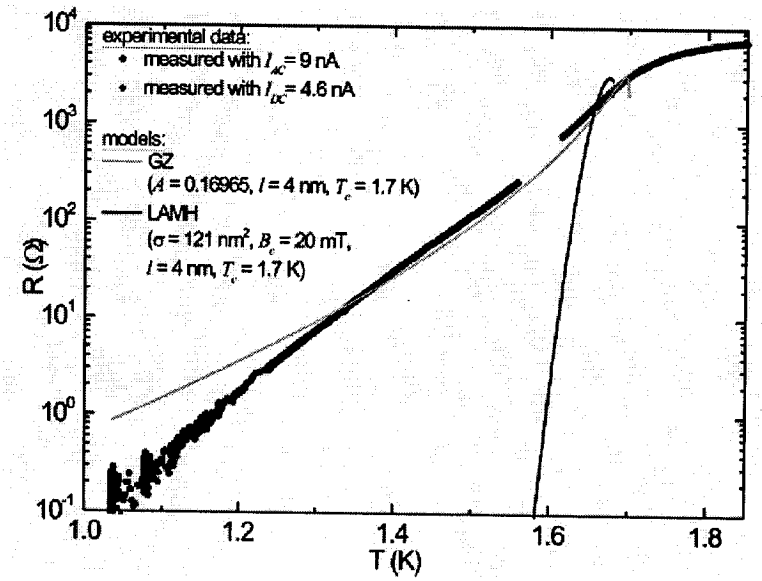

(b)

Figure 2.7: (a) Resistance as a function of temperature from Zgirski *et al.* [18] for the same Al wire. As the wire was made thinner, T_C, increases (known effect for Al) and the wire becomes more homogeneous. When the effective diameter $d = \sqrt{\sigma} = 11\,\text{nm}$ the wire's $R(T)$ behavior shows a resistive "tail" that was attributed to QPS. (b) Theoretical fits (lines) to the data (symbols) show that this "tail" can be somewhat described by a simplified fit (Eq. 2.52) to the microscopic theory of QPS [13-14]. The value $A_{GZ} = 0.16965$ was used in the fit.

Reproduced with permission of the copyright owner. Further reproduction prohibited without permission.

$\sqrt{A} = 11\,\text{nm}$ and was characterized by a resistive "tail", reminiscent of Giordano's results. Theoretical fits to the data using a much less rigorous formula than Lau's of

$$R_{eff} = A_{GZ} R_Q \frac{L}{\xi(0)} \left(1 - \frac{T}{T_C}\right)^{1/2} \exp\left[-\frac{A_{GZ} R_Q L}{R_N \xi(0)} \left(1 - \frac{T}{T_C}\right)^{1/2}\right] \tag{2.52}$$

gave satisfactory fits with $A_{GZ} = 0.16965$ (Fig. 2.7(b)).

2.3 The superconductor-insulator transition

In the preceding sections we have seen how fluctuations break the phase coherence of a superconducting wire, weakening the superconductivity in them and giving rise to resistance. Now we will consider a few other cases in which it appears that superconductivity is destroyed completely.

In 1993, Sharifi, Herzog, and Dynes [19] performed measurements on 6 μm long Pb wires fabricated by evaporation through a shadow mask. Their work was performed with a low temperature evaporator, having the advantage of repeated cycles of measurement and *in situ* evaporation. Using shadow masks of different widths, they found that as the resistance per square increased, deviations in their data from the LAMH theory appeared with the strength of the deviations increasing as wire width decreased. For the thinnest wires fabricated (width of 22 nm), it appeared that superconductivity was destroyed completely when the resistance per square of the wire in the normal state was greater than about 3 kΩ. Subsequent work by Xiong, Herzog, and Dynes [20] on similar wires confirmed the existence of a superconductor-insulator transition (SIT) with a critical resistance per square of the wire in the normal state near R_Q (Fig. 2.8).

Reproduced with permission of the copyright owner. Further reproduction prohibited without permission.

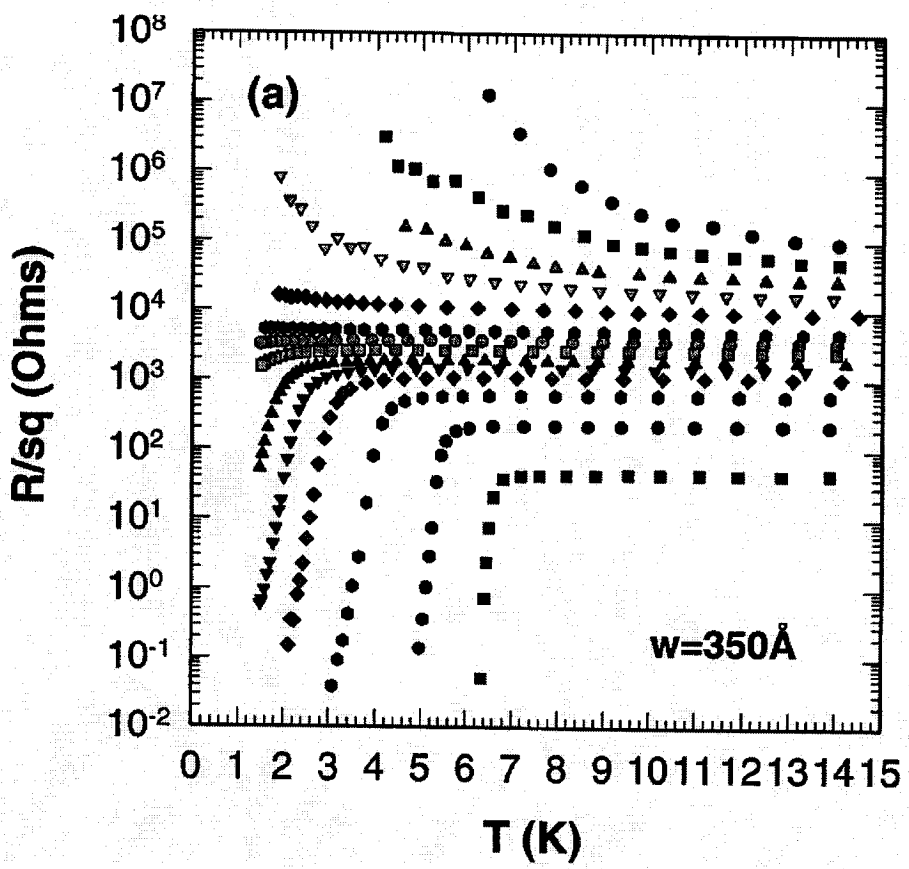

Figure 2.8: Resistance per square vs. temperature data from Xiong, Herzog, and Dynes [20] displays a superconductor-insulator transition near $R/sq \approx R_Q = 6.5\,\mathrm{k}\Omega$.

A few years later, Bezryadin, Lau and Tinkham [16] provided strong evidence for a SIT. They developed a new technique for producing homogenous one-dimensional wires in which suspended carbon nanotubes are used as templates for metal deposition (again, this will be discussed in more detail in Chapter 3). By choosing to deposit an amorphous superconducting MoGe alloy (*a*-MoGe) they were able to fabricate the thinnest wires at the time, with lengths 130-185 nm, widths 11-21 nm, and thickness 5 nm. They observed that as the normal state resistance of their wires

Reproduced with permission of the copyright owner. Further reproduction prohibited without permission.

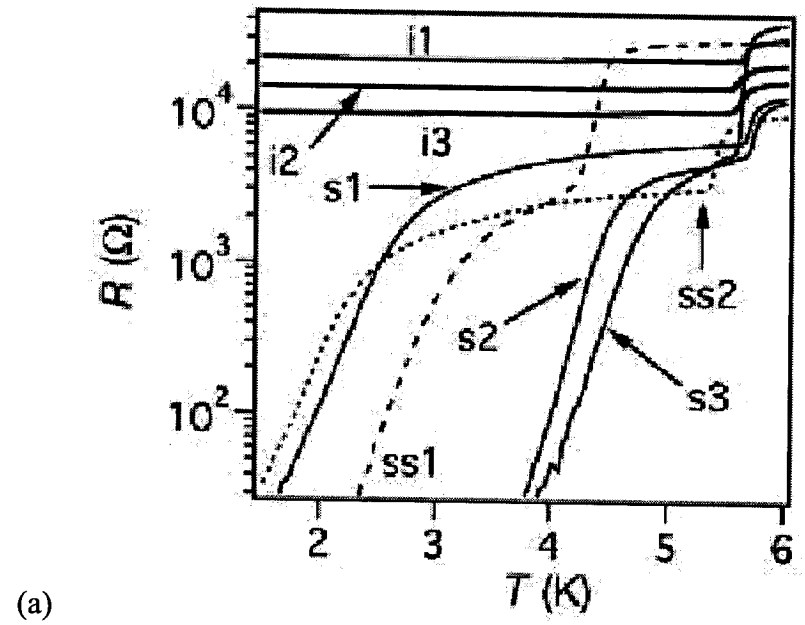

(a)

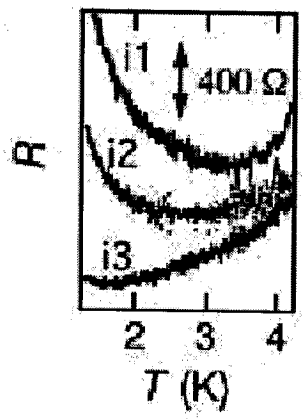

(b)

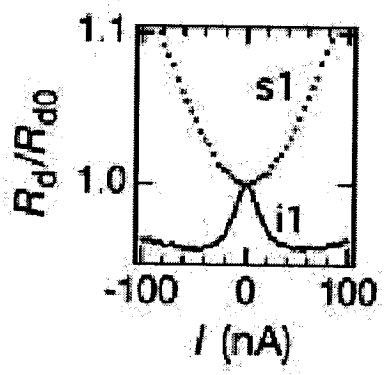

(c)

Figure 2.9: Data from Bezryadin, Lau, and Tinkham [16] shows a clear superconductor-insulator transition. (a) Resistance vs. temperature curves of wires display only superconducting (samples s1, s2, and s3) or insulating behavior (samples i1, i2, and i3). Samples ss1 and ss2 are double-wire samples. Transition occurs when wire normal state resistance is near 6.5 kΩ. (b) Zoomed in resistance vs. temperature curves for the insulating wires demonstrating their low temperature upturns. (c) Differential resistance vs. bias current normalized to its value at zero bias shows superconducting wires display a zero-bias minimum whereas insulating wires show a zero-bias peak.

Reproduced with permission of the copyright owner. Further reproduction prohibited without permission.

increased, a superconductor-insulator transition occurred, in which wires with $R_N < R_Q$ were superconducting with $R \to 0$ as $T \to 0$ (Fig. 2.9(a)). The resistance of wires with $R_N > R_Q$ did not display this same behavior but rather increased with decreasing temperature (Fig. 2.9(b)). The differential resistance, $R_d = dV(I)/dI$, also showed a dichotomy, with superconducting wires having a zero-bias minimum and insulating wires a zero-bias maximum. Due to a variety of facts including: (i) the critical point is at $R_N = R_Q$, (ii) the superconducting and insulating properties become more pronounced as $|R_N - R_Q|$ increases, and (iii) the difference between superconducting and insulating wires becomes stronger as $T \to 0$, the observed SIT was interpreted as a dissipative phase transition, similar to that observed in shunted Josephson junctions [21]. The superconducting state then was described as one in which QPS are nonexistent, being damped [22] away by the high conductance of these wires, whereas the insulating state occurs because the damping in those wires is weak and a proliferation of QPS completely destroys the superconductivity.

Using the QPS rate given by Eq. 2.48, Golubev and Zaikin [14] calculated the typical time, $t_{GZ} = \Gamma_{GZ}^{-1}$, between QPS for the set of MoGe wires studied by Bezryadin, Lau, and Tinkham and found that a dissipative phase transition is not necessarily needed to explain their results. By setting $A_{GZ} = 1$, Golubev and Zaikin found that $10^{-11}\,\mathrm{s} \le t_{GZ} \le 10^{-9}\,\mathrm{s}$ for the insulating samples and $10^{-6}\,\mathrm{s} \le t_{GZ} \le 10^{0}\,\mathrm{s}$ for the superconducting samples and so relative to the experiment time, of order 1 s, the effects of QPS should be readily apparent in *all* wires. Therefore, a dissipative phase transition is indeed needed to explain the results of Bezryadin, Lau, and Tinkham. However, when

Reproduced with permission of the copyright owner. Further reproduction prohibited without permission.

Golubev and Zaikin used $A_{GZ} = 2$ they found that $10^{-8}\ \mathrm{s} \leq t_{GZ} \leq 10^{-4}\ \mathrm{s}$ for the insulating samples and $10^{-1}\ \mathrm{s} \leq t_{GZ} \leq 10^{14}\ \mathrm{s}$ for the superconducting samples, indicating that the insulating samples are insulating due to high QPS rate but that the superconducting samples only appear superconducting because the QPS rate is much too low to have any effect. In light of the previously discussed results by Lau *et al.* [4] obtained on a larger set of MoGe wires that did not observe a SIT but rather behavior that was attributed to the QPS rate in each individual wire, perhaps a low QPS rate in the those wires identified as superconducting in Ref. [16] is a more reasonable explanation. Due to this and the uncertainty in knowing the numerical factor A_{GZ} precisely it becomes hard to conclude whether or not the dichotomy observed by Bezryadin, Lau, and Tinkham is truly due to a dissipative phase transition or not.

Finally, we should like to note the recent work by Rogachev and Bezryadin [23] that fuels the controversy over whether a superconductor-insulator transition takes place in one-dimensional superconductors. Results (Fig. 2.10) very similar to Ref. [16] were obtained in this work with Nb nanowires, also fabricated by the molecular templating technique, that had lengths 110-235 nm and widths 10-20 nm. Two important differences of this work however are that the Nb wires used in Ref. [22] are not quite as homogeneous as those in Ref. [16] fabricated with *a*-MoGe, showing signs of polycrystallinity under TEM investigation. Also, the critical resistance was found to be at a higher value of 10 kΩ, suggesting that, if a SIT in one dimension does exist, $R_N = R_Q$ may not be a universal condition.

Reproduced with permission of the copyright owner. Further reproduction prohibited without permission.

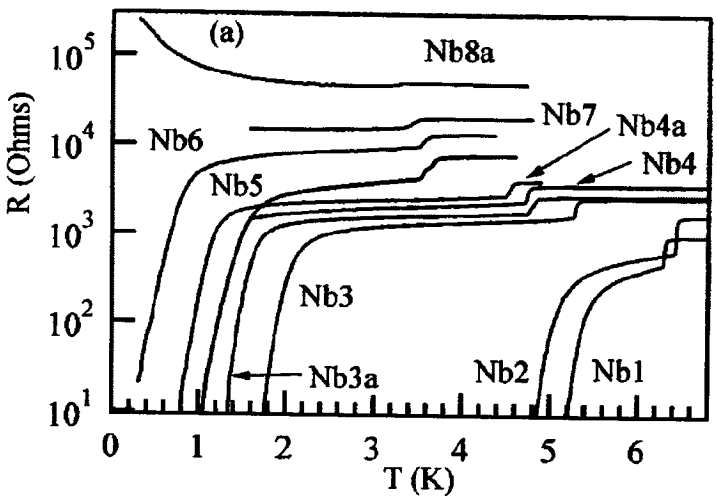

Figure 2.10: Data from Rogachev and Bezryadin [22] show superconductor-insulator transition when wire normal state resistance is near 10 kΩ.

2.4 References

[1] V. L. Ginzburg and L. D. Landau, Zh. Eksperim. i. Teor. Fiz. **20**, 1064 (1950).

[2] W. A. Little, Phys. Rev. **156**, 398 (1967).

[3] J. S. Langer and V. Ambegaokar, Phys. Rev. **164**, 498 (1967).

[4] C. N. Lau, N. Markovic, M. Bockrath, A. Bezryadin, and M. Tinkham, Phys. Rev. Lett. **87**, 217003 (2001).

[5] D. E. McCumber and B. I. Halperin, Phys. Rev. B **1**, 1054 (1970).

[6] J. E. Lukens, R. J. Warburton, and W. W. Webb, Phys. Rev. Lett. **25**, 1180 (1970).

[7] R. S. Newbower, M. R. Beasley, and M. Tinkham, Phys. Rev. B **5**, 864 (1972).

[8] N. Giordano, Phys. Rev. Lett. **61**, 2137 (1988).

[9] A. J. Van Run, J. Romijn, and J. E. Mooij, Jpn. J. Appl. Phys. **26**, 1765 (1987).

[10] J. M. Martinis, M. H. Devoret, and J. Clarke, Phys. Rev. B **35**, 4682 (1987).

[11] J. M. Duan, Phys. Rev. Lett. **74**, 5128 (1995).

Reproduced with permission of the copyright owner. Further reproduction prohibited without permission.

[12] Y. Chang, Phys. Rev. B **54**, 9436 (1996).

[13] A. D. Zaikin, D. S. Golubev, A. van Otterlo, G. T. Zimányi, Phys. Rev. Lett. **78**, 1552 (1997).

[14] D. S. Golubev and A. D. Zaikin, Phys. Rev. B **64**, 014504 (2001).

[15] J. M. Graybeal and M. R. Beasley, Phys. Rev. B **29**, 4167 (1984); J. M. Graybeal, Ph.D. thesis, Stanford University, 1985.

[16] A. Bezryadin, C. N. Lau, and M. Tinkham, Nature **404**, 971 (2000).

[17] C. N. Lau, Ph.D. thesis, Harvard University, 2001.

[18] M. Zgirski, K. -P. Riikonen, V. Touboltsev, and K. Arutyunov, Nano Lett. **5**, 1029 (2005).

[19] F. Sharifi, A. V. Herzog, and R. C. Dynes, Phys. Rev. Lett. **71**, 428 (1993).

[20] P. Xiong, A. V. Herzog, and R. C. Dynes, Phys. Rev. Lett. **78**, 927 (1997).

[21] J. S. Penttilä, Ü. Parts, P. J. Hakonen, M. A. Paalanen, and E. B. Sonin, Phys. Rev. Lett. **82**, 1004 (1999).

[22] A. O. Caldeira and A. J. Leggett, Phys. Rev. Lett. **46**, 211 (1981).

[23] A. Rogachev and A. Bezryadin, Appl. Phys. Lett. **83**, 512 (2003).

Reproduced with permission of the copyright owner. Further reproduction prohibited without permission.

Chapter 3

Fabrication and Measurement of Superconducting Nanowires

Superconducting wires have been fabricated in the past by a number of different means. Some of the earliest work relied on using single crystals of tin, known as whiskers, to study one-dimensional superconductivity [1, 2]. As fabrication technology improved, wires of increasingly smaller cross-sectional area were made using step edge [3] and stencil mask techniques [4]. These methods hinted at possible quantum effects, such as quantum phase slips [3] and quantum phase transitions [4], which may exist in superconducting wires of reduced dimensions.

To make wires with diameters that are small enough (< 20 nm) to explore these effects we have used the method of molecular templating [5]. The basic idea behind this technique is to deposit superconducting metal onto a free-standing molecule. Since the width of a molecule is on the order of a nanometer, the wire formed on top of the molecule will have a comparable width. This method has the advantage that the diameter of the wire depends on the amount of deposited material, which is a quantity that is easily controlled during the sputtering process. Also, many wires are fabricated on the same substrate, allowing us to choose the best (based on apparent homogeneity, desired dimensions, etc.) for measurement. It should be noted that this technique is not limited to

Reproduced with permission of the copyright owner. Further reproduction prohibited without permission.

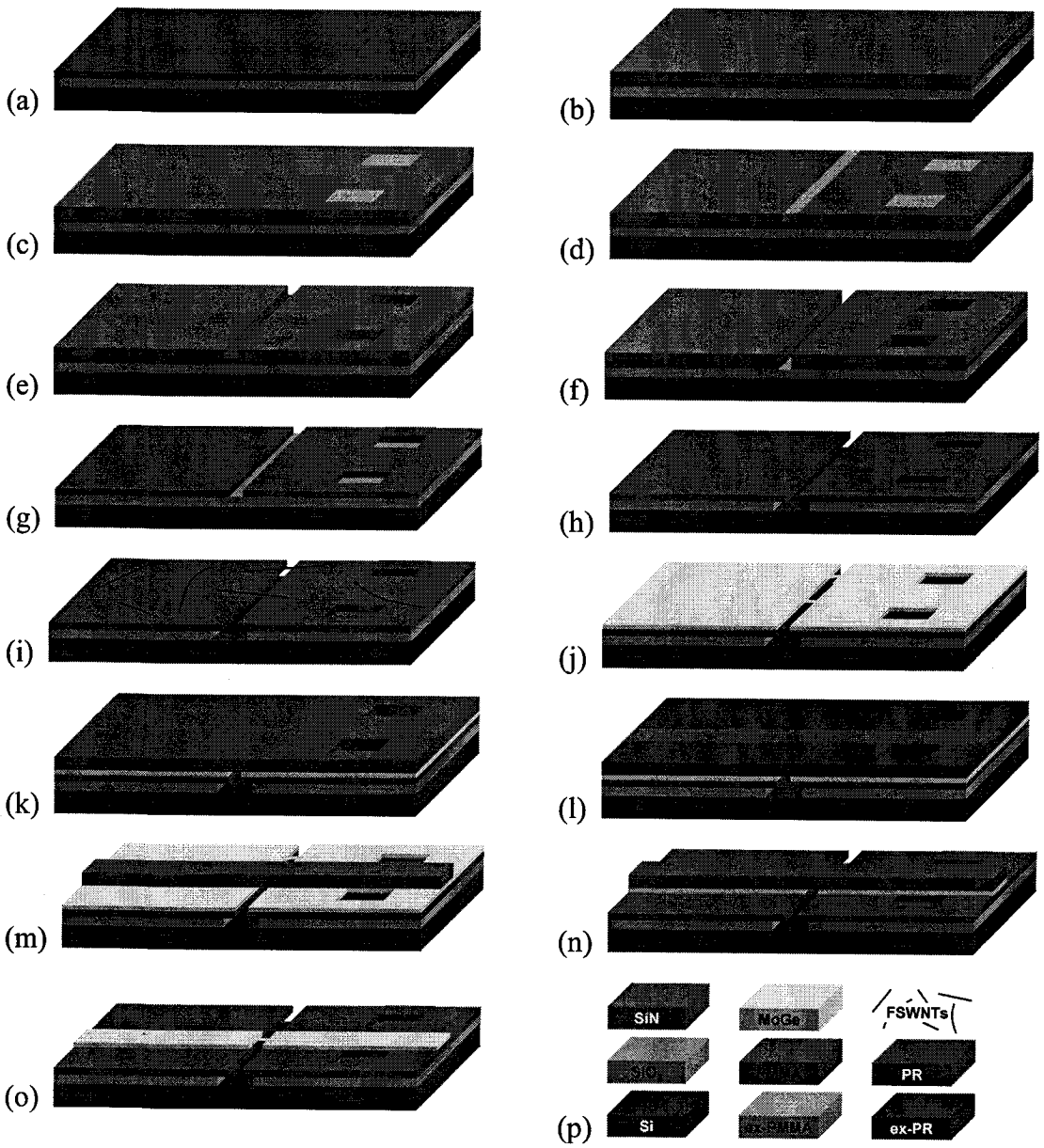

Figure 3.1: Diagram of steps involved in the fabrication of superconducting nanowires by molecular templating. (a) Begin with initial $Si/SiO_2/SiN$ substrate. (b) Spin on e-beam resist. (c) Write alignment markers. (d) Write trench line. (e) Develop e-beam resist. (f) Transfer pattern into SiN layer with RIE using SF_6 gas. (g) Remove e-beam resist using procedure described in the text. (h) Wet etch SiO_2 layer with HF. (i) Deposit FSWNTs. (j) Sputter MoGe. (k) Spin on photoresist. (l) Mask off selected wire and expose photoresist. (m) Develop photoresist. (n) Wet etch extra wires and film with H_2O_2. (o) Remove photoresist with acetone. (p) Legend.

Reproduced with permission of the copyright owner. Further reproduction prohibited without permission.

making superconducting wires – by using different metals (and perhaps an appropriate sticking layer) normal metal and ferromagnetic wires can also be fabricated [6].

3.1 Fabrication of superconducting nanowires

3.1.1 Preparing the substrate

The first step in making our superconducting nanowires is to prepare a substrate suitable for deposition of free-standing molecules. We begin with a 4 inch wafer that is composed of three layers: a 500 μm Si base layer, a 0.5 μm SiO_2 middle layer grown by dry (0.1 μm) and wet (0.4 μm) oxidation, and a 60 nm low stress SiN top layer deposited by low-pressure chemical vapor deposition (Fig. 3.1(a)). The wafer is covered with e-beam resist (Fig. 3.1(b)) and the entire wafer is written with a repeated 4.8 mm × 4.8 mm pattern that consists of a fine line written down the middle of each individual pattern (Fig. 3.1(c)) as well as alignment markers off to the side of this line (Fig. 3.1(d)). The fine line will become the trench across which molecules will be deposited and its width will help define the length of the subsequently fabricated nanowires. To study a variety of nanowire lengths we used patterns with line widths of 50, 100, and 450 nm. The alignment markers are numbered, spaced 20 μm apart, and are used later in the fabrication process to help locate the desired wire along the 4.8 mm long trench.

After developing the patterns (Fig. 3.1(e)) parts of the SiN layer are exposed and the pattern in transferred into this layer by reactive ion etching with an SF_6 plasma (Fig. 3.1(f)). The e-beam resist is then removed with acetone and the entire wafer is coated with photoresist. An automated dicing saw is used to cut the wafer into individual 4.8 mm × 4.8 mm patterned chips. The previous photoresist deposition ensures that the

Reproduced with permission of the copyright owner. Further reproduction prohibited without permission.

silicon "dust" created by the dicing does not land on the SiN layer as this dust is rather hard to remove from SiN but is easily washed away when the photoresist is removed. To remove the photoresist we sonicate the chip in acetone for 10 min. followed by rinsing in deionized water for ~ 30 sec. The chip is then sonicated in nitric acid for 10 min. followed by another rinse in deionized water for ~ 30 sec.

At this point (Fig. 3.1(g)) the chip is immersed in hydrofluoric acid for 10 sec. which creates an undercut in the SiO_2 layer due to the much greater etching rate of SiO_2 compared to SiN (Fig. 3.1(h)). This is followed by rinsing in deionized water for ~ 30 sec., soaking in nitric acid for 2 min. to remove any residual organics, rinsing in deionized water for ~ 30 sec, rinsing in isopropanol for ~ 30 sec., and then blowing the chip dry with forced nitrogen gas.

3.1.2 Depositing fluorinated single walled carbon nanotubes

The molecules used in this project as nanowire templates are fluorinated single walled carbon nanotubes (FSWNTs). These molecules are ideal templates for wires as they are known to be insulating [7], which eliminates the possibility of any parallel conduction through them that may unnecessarily complicate data analysis. Their insulating nature also insures that we do not place any dissipative reservoir in close proximity with the wires that could affect any quantum phase slip processes. The FSWNTs can also be easily dissolved in isopropanol, which makes depositing them from solution rather simple. Finally, as these molecules are commercially available (Carbon Nanotechnologies, Inc.) they are easily acquired and do not need to be grown by the user.

When starting with FSWNTs as received from the manufacturer the first step is to make a "master" solution from which an optimum solution can be obtained. This entails

Reproduced with permission of the copyright owner. Further reproduction prohibited without permission.

sonicating a small piece (about 1 mm^3) of bulk FSWNTs in isopropanol (about 12 ml) for 20 min. The sonication will help to break up the FSWNTs and promote their dissolving. After sonication the master solution should be nearly transparent with a slight grey color to it. No visible clusters of FSWNTs should remain, but if they do the solution should be sonicated further before using.

Once the master solution is made, a separate diluted solution can be obtained from it for depositing FSWNTs. If the master solution has been stored for some time it is usually a good idea to sonicate it for about 5 min. to ensure the FSWNTs are well dispersed before making the diluted solution. A typical dilution is 1:10 to 1:20 parts master solution to isopropanol by volume, though this can vary somewhat depending on how rich the master solution was made. The dilution is tested by making a diluted solution, depositing a drop of it onto a chip with a trench in it, letting the drop sit for 1 min., blowing the excess off with forced nitrogen gas, and then examining the chip under an SEM. What we ideally would like to see is one nanotube crossing the trench about every 20 μm. This allows for an easier alignment when doing the later photolithography steps. Once we have calibrated the proper dilution we can use it each time for the same master solution.

To deposit FSWNTs for use as templates we first make a fresh diluted solution using the calibration outlined in the preceding paragraph. To deposit the FSWNTs we then proceed as before: placing one drop of diluted solution from a pipette onto the surface of a freshly undercut and cleaned chip, waiting for 1 min., and blowing the excess off with forced nitrogen gas. It is very important that we do not attempt to clean the chip any further with isopropanol as this will remove the FSWNTs that we have just

Reproduced with permission of the copyright owner. Further reproduction prohibited without permission.

deposited. Since the length of the FSWNTs is of the order of a few microns or more some will be deposited to one side or the other of the trench but some will span the trench providing templates for the nanowires (Fig. 3.1(i)).

3.1.3 Sputtering MoGe

As with any fabrication method, the choices of which metal to use and how to deposit it have a strong influence on the resultant wires made using molecular templating. We wanted to make superconducting wires that were as thin as possible and yet still continuous and homogeneous. We also preferred for them to have a critical temperature, T_C, that was high enough that we could easily measure their properties using standard liquid ^{4}He and ^{3}He cryostats.

To obtain wires with these minimum of requirements we use the alloy $Mo_{0.79}Ge_{0.21}$. The $Mo_{1-x}Ge_x$ system has been shown to undergo a structural phase transition from a BCC phase to an amorphous phase at $x = 0.195$ [8-10]. For $x < 0.195$,

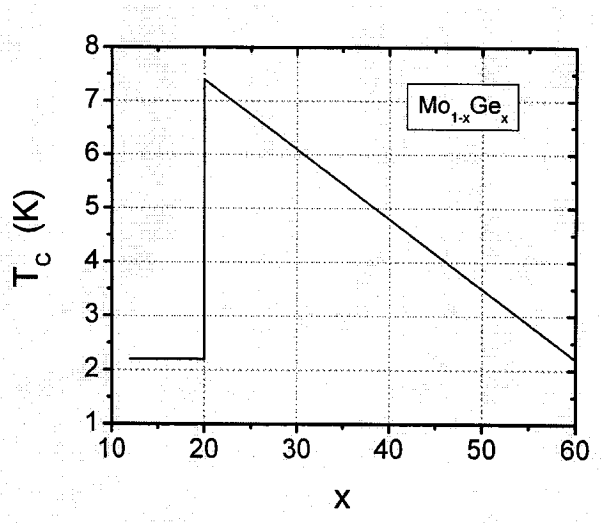

Figure 3.2: Bulk T_C as a function of germanium content, x, for $Mo_{1-x}Ge_x$.

Reproduced with permission of the copyright owner. Further reproduction prohibited without permission.

Mean Free Path (ℓ)	3 Å [*]
Density (ρ)	9.7 g / cm^3 [†]
Resistivity (ρ)	180 μΩ-cm [*]
Fermi Velocity (v_F)	10^6 m/s [*]
Fermi Wavevector ($k_F = mv_F/\hbar$)	0.863 Å^{-1}
Critical Temperature (T_c)	7.36 K (bulk) [*] 5.62 K (film) [*]
Energy Gap ($\Delta(0)$)	1.1 meV (bulk) [*] 1.0 meV (film) [*]
Ginzburg-Landau Coherence Length ($\xi(0)$)	4.4 nm (bulk) [*] 4.9 nm (film) [*]
Pippard (BCS) Coherence Length ($\xi_0 = \hbar v_F/\pi\Delta(0)$)	210 nm (film)
London Penetration Depth ($\lambda_L(0) = \lambda_{eff}(0)(1.33\ \ell/\xi_0)^{1/2}$)	18.5 nm (film)
Effective Penetration Depth ($\lambda_{eff}(0)$)	424 nm (film) [*]
Ginzburg-Landau Parameter ($\kappa = \lambda_{eff}(0)/\xi(0)$)	86.5
Lower Critical Field ($H_{C1} = (H_{C2} \ln \kappa)/2\kappa^2$)	2 mT (film)
Upper Critical Field (H_{C2})	12.2 T (bulk) [*] 6.7 T (film) [*]
Surface Critical Field ($H_{C3} = 1.695\ H_{C2}$)	11.4 T (film)
Thermodynamic Critical Field ($H_C = H_{C2}/\sqrt{2}\kappa$)	55 mT (film)
Debye Temperature (Θ_D)	266 K [‡]
Electron-Phonon Coupling Constant ($\lambda_{e\text{-}p}$)	0.672 [‡]
Bare Density of States ($N_B(0)$)	0.775 states / eV-atom [‡]
Electronic Specific Heat Coefficient (γ)	3.05 mJ / mol-K^2 [‡]
Velocity of Mooij-Schon Mode (c_{MS})	2 eV-Å [§]

Table 3.1: Measured and derived physical parameters for MoGe. For derived values, the equation used is indicated.

[*] Ref. [8].

[†] Extrapolation to $Mo_{0.79}Ge_{0.21}$ from Ref. [10].

[‡] Data for $Mo_{0.73}Ge_{0.27}$ from Ref [9].

[§] Ref. [13].

Reproduced with permission of the copyright owner. Further reproduction prohibited without permission.

the bulk T_C of the alloy remains essentially constant at $T_C = 2.2$ K [8]. At the structural phase transition, the bulk T_C jumps suddenly to $T_C = 7.36$ K and then decreases with increasing Ge content (Fig. 3.2). Other known physical parameters are listed in Table 3.1.

In light of the above observations, we see that the particular alloy that we use, $Mo_{0.79}Ge_{0.21}$, is an ideal material from which to fabricate our wires. By choosing a Ge content close to the structural phase transition we essentially maximize the bulk T_C while still maintaining a safe distance from the transition. If the Ge content of our alloy was very close to the structural phase transition we would run the risk that the local Ge content variation would be sufficient to cause some granularity in our wires as part of the MoGe would come together in small BCC crystals. With our selected MoGe alloy

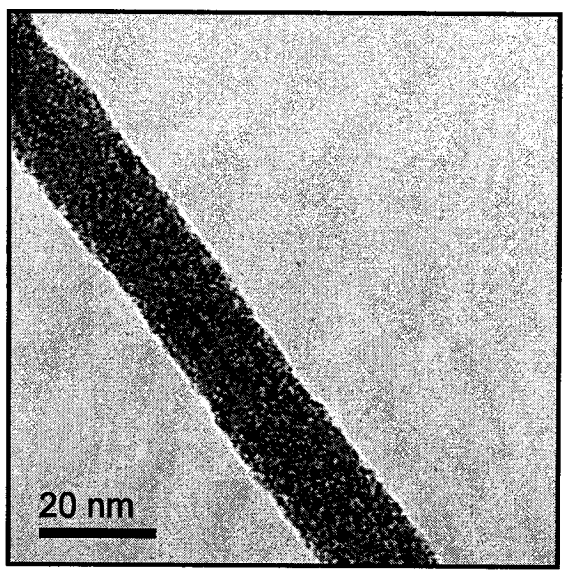

Figure 3.3: TEM image of a MoGe wire demonstrating the amorphous structure of the MoGe alloy.

Reproduced with permission of the copyright owner. Further reproduction prohibited without permission.

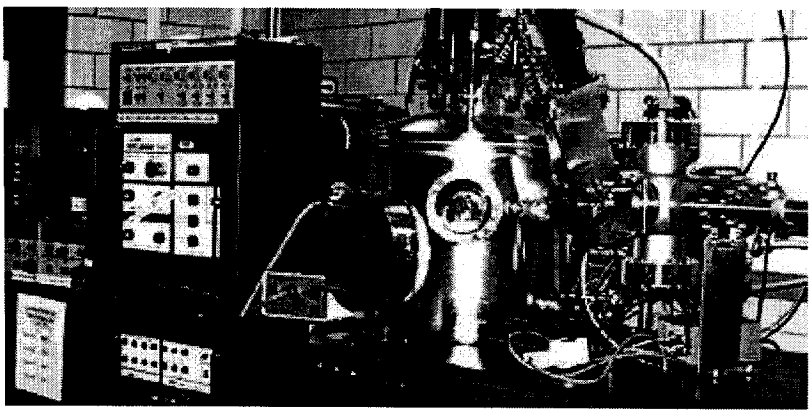

Figure 3.4: The AJA sputtering system of the Materials Research Laboratory's Microfabrication and Crystal Growth Facility.

deposited by sputtering we are ensured that our wires remain in the amorphous structural phase, as has been confirmed by TEM imaging (Fig. 3.3)

The sputtering is done in the AJA sputtering system (Fig. 3.4) of the Materials Research Laboratory's Microfabrication and Crystal Growth Facility. The main vacuum chamber is equipped with a liquid nitrogen cold trap that was found to be essential for depositing high quality films. Films grown without using the cold trap have reduced critical temperatures due to oxygen contamination as revealed by Auger analysis. This is most likely due to the target-substrate separation of ~12 cm, which results in a lower sputtering rate than in other systems where the target-substrate separation is much less. The decreased sputtering rates allow for a larger level of contamination if the cold trap is not used.

Each time the MoGe target is used it is presputtered for 15 min without any substrate inside the main chamber to remove any oxidation or other surface contaminants. The substrates are then placed into the main chamber without breaking vacuum through a load lock chamber. The stage to which the substrates are attached is rotated at ~20 rpm

Reproduced with permission of the copyright owner. Further reproduction prohibited without permission.

to help increase the uniformity of the deposited metal. With the cold trap, base chamber pressures < 1×10^{-7} Torr are routinely acquired. The MoGe target is sputtered at 150 W in the presence of 4 mTorr of argon gas introduced into the chamber at a rate of 20 sccm resulting in a sputtering rate of 1.25 Å/s as determined from profilometry.

3.1.4 Scanning electron microscopy

Once the substrate is coated with MoGe (Fig. 3.1(j)) many wires connecting the films on either side of the trench exist. Using the Hitachi S-4700 scanning electron microscope (SEM) (Fig. 3.5) of the Center for Materials Microanalysis we examine a large fraction of these wires until an appropriate one is found. Suitable wires should be straight and have an apparent width that does not vary along the length of the wire (Fig. 3.6). Also, the ends of the wires should show good contact to the films, without any darkened area at the ends that are indicative of weak links. Once a good wire is found its location relative to a nearby alignment marker (Fig. 3.7) is noted the area in the wire's immediate vicinity (about 20 μm on both sides of the wire) is examined carefully to make

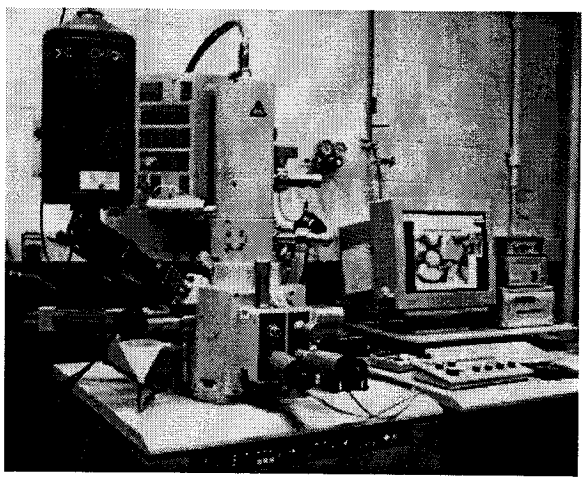

Figure 3.5: The Hitachi S-4700 SEM of the Center for Materials Microanalysis.

Reproduced with permission of the copyright owner. Further reproduction prohibited without permission.

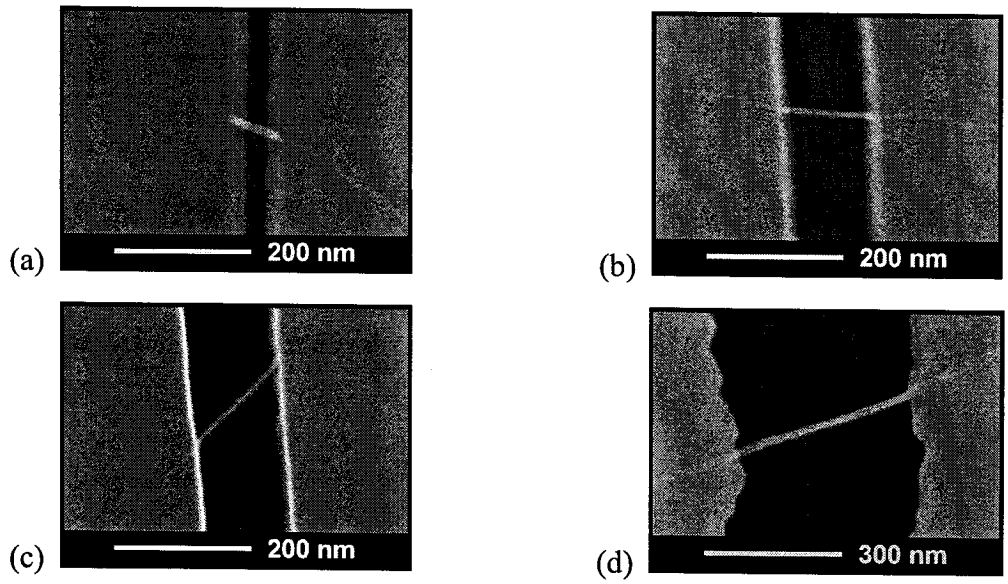

Figure 3.6: SEM images of (a) short length wire (50 nm trench width substrate), (b, c) standard length wires (100 nm trench width substrate), and (d) long length wire (450 nm trench width substrate). SEM measured wire widths are (a) 14.4 nm, (b) 8.8 nm, (c) 10.4 nm, and (d) 19.94 nm.

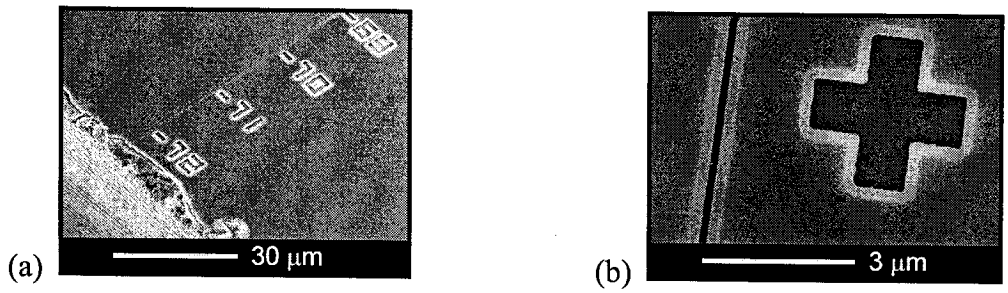

Figure 3.7: SEM images of (a) alignment markers and (b) a wire relative to an alignment marker.

sure that no other wires or otherwise undesirable parallel connection exists between the thin films. If something does happen to be found its location is also noted so that in the following photolithography step the mask can be aligned such as to exclude the defect from the final device structure.

Reproduced with permission of the copyright owner. Further reproduction prohibited without permission.

3.1.5 Photolithography and etching

A standard photolithography process, performed in the Materials Research Laboratory's class 100 cleanroom, is employed to mask off the single desired wire. The sample is prebaked at 100°C for 5 min. followed by a fine coating of hexamethyldisilizane (HMDS) that serves as a primer for photoresist application. The resist (AZ-5214) is spun on for 20 sec. at 7000 rpm and then softbaked for 40 sec. also at 100°C (Fig. 3.1(k)).

The mask alignment and exposure (Fig. 3.1(l)) is done with a Suss Microtech Inc. MJB3 mask aligner (Fig. 3.8) fitted with a high pressure mercury bulb that emits UV radiation with a wavelength of 365 nm. A diagram of the mask that is used is shown in Fig. 3.9. The exposed photoresist is developed (Fig. 3.1(m)) with either AZ Developer for 20 sec or with a solution consisting of 1 part by volume AZ 351 Developer and 5 parts by volume deionized water for 40 sec (despite the similarity of the names these are two different developers). After development, excess developer is rinsed away with deionized water.

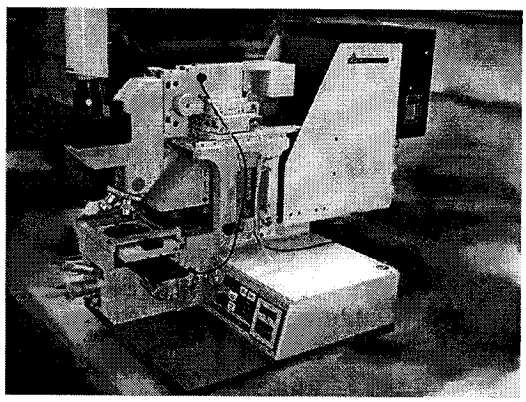

Figure 3.8: The Materials Research Laboratory's Suss Microtech Inc. MJB3 mask aligner.

Reproduced with permission of the copyright owner. Further reproduction prohibited without permission.

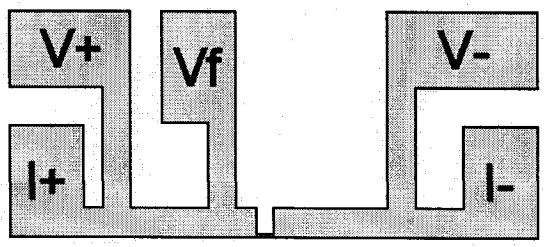

Figure 3.9: Diagram of electrode pad photolithography mask. The thin bridge, which is 5, 10, 15, or 20 μm wide depending on the specific mask that is used, located at bottom center masks off the selected nanowire sample. After fabrication and mounting, current will be passed between the resulting I+ and I- leads and voltage is measured between the V+ and V- leads. Alternatively, the voltage drop across a section of the thin film electrodes only can be measured between the V+ and Vf leads.

Once the desired wire is masked off there are two options for etching away the extra wires and sections of thin film: wet etching and plasma etching. We have found that plasma etching MoGe in a reactive ion etching (RIE) system with SF_6 gas frequently destroys the wires, presumably because the RF field in the chamber induces some voltage across the wire that is large enough to "burn" it. The RIE system we have available to us, however, will not ignite the plasma for powers less than 20 W and it is known that samples plasma etched elsewhere with low power (2-5 W) survived [5, 11, 12].

Instead of the plasma etching then we use a wet etch with 3% H_2O_2, which has an etching rate of about 1 nm/sec. The samples are immersed in H_2O_2 for a time consistent with their film thickness and then immediately rinsed with deionized water (Fig. 3.1(n)). The final step is to remove the photoresist by soaking the sample in acetone for 2 min. After the photoresist is removed (Fig. 3.1(o)), the excess acetone is blown from the surface of the sample with forced nitrogen gas perpendicular to the trench so that the acetone flow is parallel to the wire. Obviously, from this point on the sample should be

Reproduced with permission of the copyright owner. Further reproduction prohibited without permission.

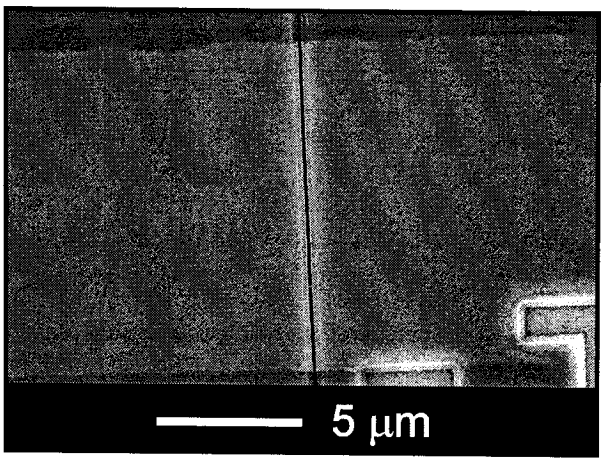

Figure 3.10: SEM image of a finished device. The trench in the picture is the dark line that is nearly vertical. The thin film electrodes are clearly distinguishable from the areas of substrate where the films have been etched away and are aligned with the marker. The wire they are connected to is just visible at a position along the trench at about the same level as the top of the large "7" in the lower left corner.

kept from coming into contact with H_2O_2, but even water is known to slowly etch MoGe so samples should be kept free from any moisture whatsoever. This is most easily accomplished by storing the finished samples (Fig. 3.10) under vacuum in a pumped dessicator box, which will also slow the aging of the samples due to oxidation.

3.2 Measurement of superconducting nanowires

3.2.1 Mounting the sample

To connect the samples to the measurement electronics, we use a chip carrier made from a 6 pin forked dip header. The sample is attached to the dip header with carbon tape as this type of tape retains its adhesion down to very low temperatures. Thin gold wires are connected to the dip header's forks using silver paste and to the sample by indium dots.

Reproduced with permission of the copyright owner. Further reproduction prohibited without permission.

Special care must be taken while making connections to the sample since they are very sensitive to static electricity. The pins of the chip carrier should be connected together and grounded with a special socket made for this purpose. The person mounting the sample should also ground themselves with a grounding strap. Extra measures, such as a grounded tool for pressing the indium dots, wearing insulating gloves, and spraying the work area with anti-static spray are also a good idea.

3.2.2 Cryostats

Once the sample is mounted in a chip carrier, the chip carrier is inserted into a socket in of the three cryostats we use to measure the samples. All samples in this study were measured with a ^{4}He dipstick, which reaches temperatures of 1.5 K. Samples that appeared to show interesting behavior below this temperature or that we wanted to apply

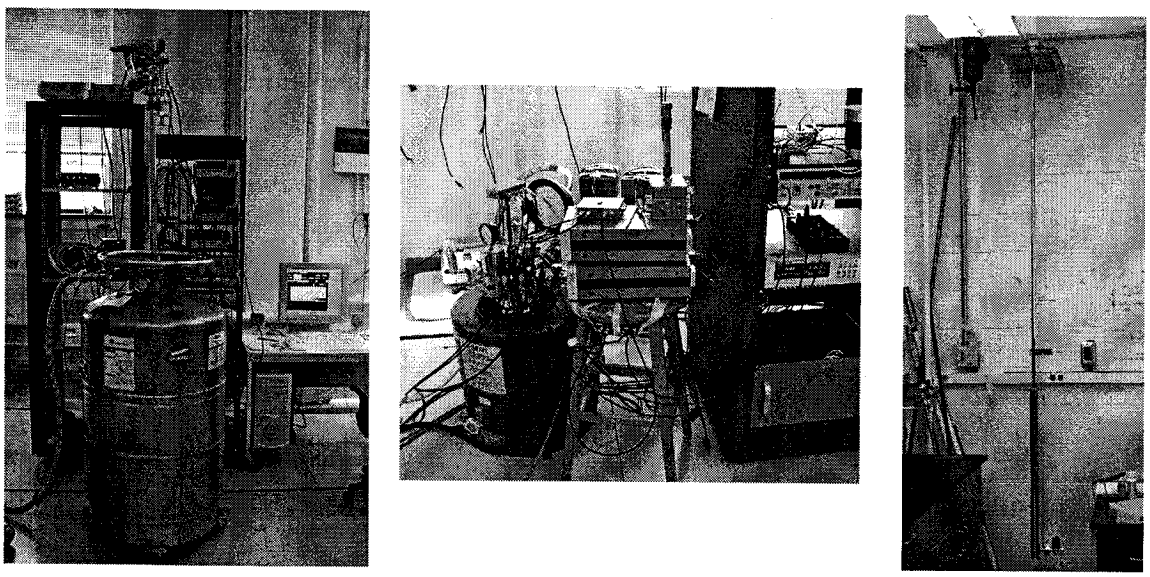

(a) (b) (c)

Figure 3.11: Pictures of (a) the ^{4}He dipstick being used in a transport dewar, (b) the ^{3}He system, and (c) the dilution refrigerator insert.

Reproduced with permission of the copyright owner. Further reproduction prohibited without permission.

a magnetic field to were then measured with a ^{3}He system, which allowed us to measure down to 0.28 K. A few samples were further measured in a dilution refrigerator down to 10 mK.

The ^{4}He dipstick (Fig. 3.11(a)) is a relatively simple system in which the chip carrier is inserted into a socket located at the bottom of the dipstick. The eight measurement leads connected to the socket are thermally anchored to a copper block that the socket is attached to by silver paste. Embedding the wires in silver paste also provides some filtering of high frequency noise. A calibrated Cernox thermometer is attached very close to the socket on the copper block and the socket/copper block section in enclosed in a copper can that has been counter wound with high resistance wire that serves as a heater. The entire dipstick is enclosed in an outer vacuum can that is evacuated and then ^{4}He exchange gas is introduced into it. The dipstick is pre-cooled in a liquid nitrogen dewar to lower the temperature from room temperature to 77 K and then slowly lowered into a transport dewar that has ~15 L of liquid ^{4}He in it to get to 4.2 K. Finally, the transport dewar is pumped on for many hours (usually overnight) to achieve the base temperature of 1.5 K. Once there, the temperature can remain at 1.5 K for about 24 hours.

The ^{3}He system (Fig. 3.11(b)) is a sample in vacuum series ^{3}He system made by Janis Research Company. The measurement leads coming down from the top of the cryostat are high resistance wires thermally anchored to the 1K pot to minimize heat transfer from room temperature to the 1K pot. High resistance wires are also located between the 1K pot and the ^{3}He pot and between the ^{3}He pot and RC filters located at the top of the copper measurement attachment that is mounted directly to the ^{3}He pot. About

Reproduced with permission of the copyright owner. Further reproduction prohibited without permission.

1 m of lower resistance wires are then used after the RC filters. These wires are wrapped many times around the attachment and thermally anchored with silver paste, which again also serves as a high frequency filter. These wires then connect to two sample sockets that are shielded by a copper can and oriented perpendicularly to each other for parallel and perpendicular magnetic field arrangements. Lower resistance wires are used here to make it easier for the sample to thermalize through them. The sample is placed in one of the sockets and a calibrated ruthenium oxide thermometer that is mounted in a chip carrier is placed in the other socket. In this way, the sample and thermometer are cooled in the same manner and thus should be at the same temperature. The liquid ^{4}He dewar that the ^{3}He system is placed in is fitted with a 9 T superconducting magnet for field measurements. Lowering the temperature of the liquid ^{4}He bath below 2.2 K by pumping on it allows us to energize the magnet further, achieving fields of 11.16 T.

For measurements at the lowest temperatures, an insert (Fig. 3.11(c)) was used for a top loading Oxford Instruments Kelvinox dilution refrigerator that is located in Dale van Harlingen's laboratory and maintained by his research group. The insert is again fitted with two sockets oriented perpendicularly to each other that can accommodate two samples as well as chip carrier mounted ruthenium oxide thermometer. The thermometer is factory calibrated down to 50 mK, below which we rely on an interpolated calibration we performed ourselves using temperature data obtained by the thermometer located on the mixing chamber. The samples and thermometer are shielded by a copper can and low temperature filtering is performed by 2 m of thermocoax cable.

Reproduced with permission of the copyright owner. Further reproduction prohibited without permission.

3.2.3 Electrical measurements

The electrical transport properties that we examine include resistance as a function of temperature, $R(T)$, voltage as a function of current, $V(I)$, and the differential resistance as a function of current, $dV(I)/dI$. An ultralow distortion frequency generator (Stanford Research Systems model DS360) is used to bias the samples through a large standard resistor (usually 1 MΩ) that is in series with the sample (Fig. 3.12). The voltage across the sample and across the standard resistor are amplified

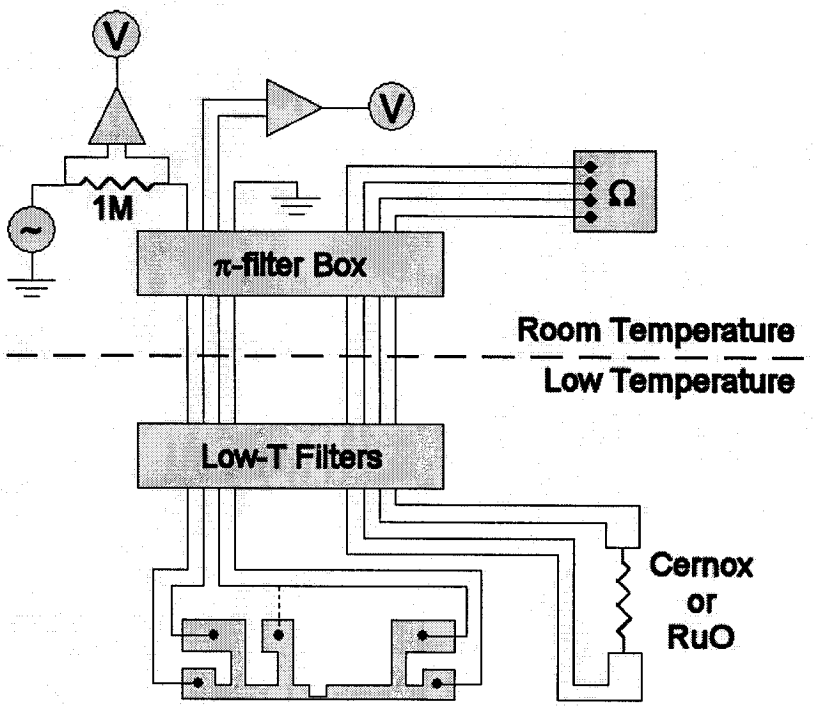

Figure 3.12: Circuit diagram for measurements of nanowires. The sample is biased with a function generator through a 1 MΩ resistor in series with the sample and measured using pre-amps. Appropriate use of π-filters at room temperature as well as low temperature filters are employed to reduce high frequency noise. The 4-probe resistance of a calibrated Cernox or ruthenium oxide thermometer (depending on the cryostat) is used for temperature measurements.

Reproduced with permission of the copyright owner. Further reproduction prohibited without permission.

with battery powered pre-amps (Stanford Research Systems Model SR560 and Princeton Applied Research model 113) that have input resistances of 100 MΩ. The output of the pre-amps are measured with a data acquisition card (National Instruments model PCI-MIO-16XE-10) installed in one of the PCI slots of the computer that runs the LabVIEW software that controls the measurement.

The $R(T)$ data is determined by a linear fit to $V(I)$ curves taken near zero-bias. The amplitude of the sinusoidal signal coming from the function generator set at about 1 mV_{p-p} so that the current through the nanowire oscillates between -1 nA to +1 nA. Generally, this level of current is acceptable for measurements down to 0.3 K. For superconducting samples, the LAMH theory (see Chapter 2) predicts linear response for currents less than 13 nA/K. The maximum measurement current to supply to insulating samples do not follow this rule of thumb as their behavior is determined by different physics but by looking at $dV(I)/dI$ data on these samples one can verify whether their measurement current is small enough or not by insuring that the bias currents stay near the top of the zero-bias peak observed in this class of samples. Also, multiple $R(T)$ curves can be taken with different measurement to verify the correct measurement current is chosen. The frequency of the sinusoidal signal from the function generator is selected so as not to be a multiple of 60 Hz – typically, 11.574 Hz was used.

When measuring $V(I)$ curves a much larger signal amplitude is needed. One must be careful not to supply too much current, however, so that the wires do not burn and also so the pre-amps do not overload. For most samples, the interesting features on a $V(I)$ can be measured with a current in the range $-1\,\mu A \le I \le 1\,\mu A$. The signal

Reproduced with permission of the copyright owner. Further reproduction prohibited without permission.

frequency should also be turned set as low as possible so that any rapid change in the $V(I)$ curve, such as at the switching current of a superconducting sample, is measured correctly. The $dV(I)/dI$ measurements proceed similarly to the $R(T)$ with a small signal amplitude at a frequency that is not a multiple of 60 Hz. A DC offset is supplied by the function generator and stepped through the same range of currents measured in the $V(I)$ curves. Since the high bias portion of a $dV(I)/dI$ measurement is typically featureless, two $dV(I)/dI$ measurements with different bias current step spacing may be performed to ensure the features are measured accurately and to save some time. The temperature is fixed to within a couple milliKelvin during $V(I)$ and $dV(I)/dI$ measurements with a LabVIEW controlled feedback loop when using the ^{4}He dipstick, the PID control of an AC resistance bridge (Lakeshore model 370) when using the ^{3}He system, or by fixing the mixing chamber temperature with the Oxford Instruments KelvinoxIGH gas and heat handling system when using the dilution refrigerator insert.

3.3 References

[1] J. E. Lukens, R. J. Warburton, and W. W. Webb, Phys. Rev. Lett. **25**, 1180 (1970).

[2] R. S. Newbower, M. R. Beasley, and M. Tinkham, Phys. Rev. B **5**, 864 (1972).

[3] N. Giordano, Phys. Rev. Lett. **61**, 2137 (1988).

[4] F. Sharifi, A. V. Harzog, and R. C. Dynes, Phys. Rev. Lett. **71**, 428 (1993).

[5] A. Bezryadin, C. N. Lau, and M. Tinkham, Nature **404**, 971 (2000).

[6] Y. Zhang and H. Dai, Appl. Phys. Lett. **77**, 3015 (2000).

Reproduced with permission of the copyright owner. Further reproduction prohibited without permission.

[7] E. T. Mickelson, C. B. Huffman, A. G. Rinzler, R. E. Smalley, R. H. Hauge and J. L. Margrave, Chem. Phys. Lett. **296**, 188 (1998).

[8] J. M. Graybeal and M. R. Beasley, Phys. Rev. B **29**, 4167 (1984); J. M. Graybeal, Ph.D. thesis, Stanford University, 1985.

[9] D. Mael, W. L. Carter, S. Yoshizumi, and T. H. Geballe, Phys. Rev. B **32**, 1476 (1985).

[10] J. B. Kortright and A. Bienenstock, Phys. Rev. B **37**, 2979 (1988).

[11] C. N. Lau, Ph.D. thesis, Harvard University, 2001.

[12] A. Bezryadin (private communication).

[13] S. Khlebnikov (private communication).

Reproduced with permission of the copyright owner. Further reproduction prohibited without permission.

Chapter 4

Properties of Superconducting Nanowires

The main result of the work presented in this dissertation is the observation and characterization of a superconductor-insulator transition (SIT) in one-dimensional nanowires. As will be shown in Chapter 6, the homogeneity of the nanowires is very important as granularity can smear the SIT considerably. Also, the theories that we will be comparing our data to are formulated for the case of homogeneous wires. Therefore, in this chapter we will begin by examining some basic results that augment the SEM and TEM results presented in Chapter 3 that provide additional evidence that the wires used in this work are indeed homogeneous and not granular. The bulk of the chapter will then be dedicated to investigating the data taken on wires that are in the superconducting regime of the SIT and their properties.

4.1 Homogeneity of nanowires

4.1.1 Resistance vs. temperature curves

One of the main features that we use to distinguish between superconducting and insulating nanowires is their resistance as a function of temperature behavior, $R(T)$. In

Reproduced with permission of the copyright owner. Further reproduction prohibited without permission.

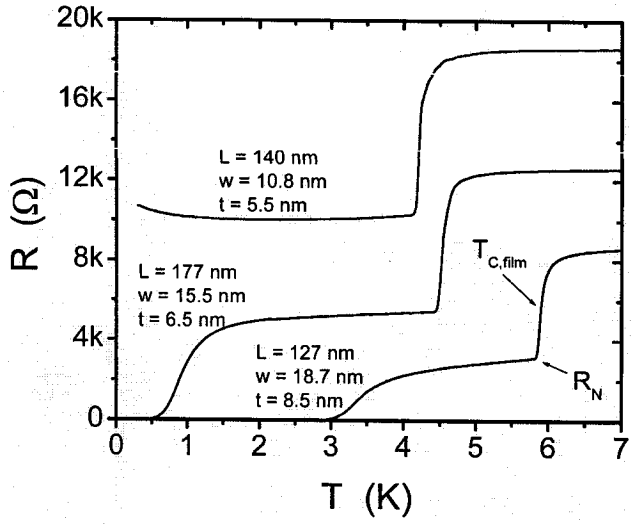

(a)

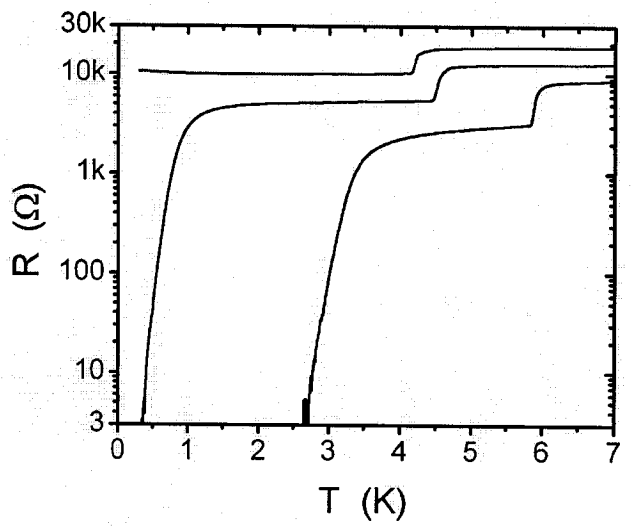

(b)

Figure 4.1: Resistance vs. temperature curves for representative nanowires in the (a) linear-linear and (b) log-linear representations. In (a), SEM measured lengths (L) and widths (w) are given as are the sputtered MoGe thicknesses (t). The film electrode's critical temperature ($T_{C,film}$) is defined to be at the midpoint of the film's superconducting transition. The normal state resistance of wires (R_N) is taken to be the resistance just after the film has become superconducting.

Reproduced with permission of the copyright owner. Further reproduction prohibited without permission.

Fig. 4.1 we show $R(T)$ curves for a few representative nanowires. Superconducting wires have a decreasing resistance as temperature is lowered with negative curvature ($d^2 \log(R)/dT^2 < 0$) in the log-linear representation (Fig. 4.1(b)). Insulating wires, on the other hand, show upturns at the lowest temperatures, with increasing resistance as temperature is lowered and positive curvature. For all of the $R(T)$ curves, a superconducting transition is observed at temperatures ~ 4-6 K that is the superconducting transition of the thin film electrodes in series with the nanowires. Below this transition the films are superconducting and we measure only the resistance of the wires themselves. We define the critical temperature of the film electrodes, $T_{C,film}$, to be the temperature at the midpoint of their superconducting transitions. The normal state resistance, R_N, of the nanowires is taken as the resistance just after the electrodes have become superconducting. Both $T_{C,film}$ and R_N are indicated in Fig. 4.1(a) for one of the nanowires.

4.1.2 Critical temperature of film electrodes

The simplest test of the quality of the sputtered MoGe films is to compare their transition temperatures with known values as significant amounts of impurities would reduce the critical temperature. In Fig. 4.2(a) we show our measurements for $T_{C,film}$ vs. the sputtered MoGe film thickness, t, compared to results obtained on MoGe thin films by Graybeal [1]. The agreement between the two data sets is good, although for our films there is a considerable amount of spread in the measured critical temperatures. This is due to the fact that we do not use a Si top layer as a barrier against oxidation in our

Reproduced with permission of the copyright owner. Further reproduction prohibited without permission.

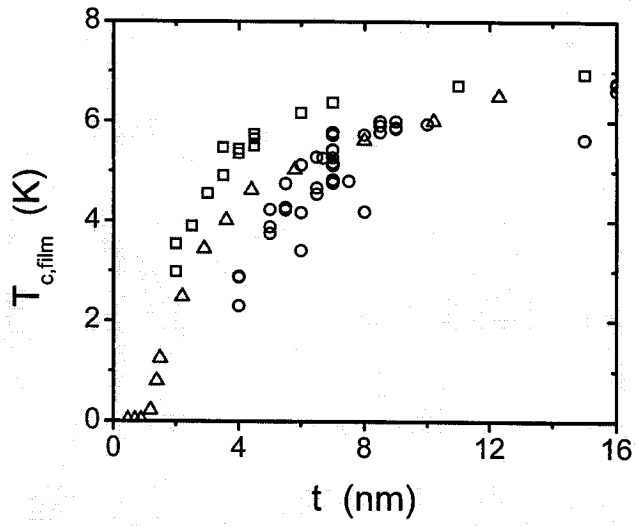

(a)

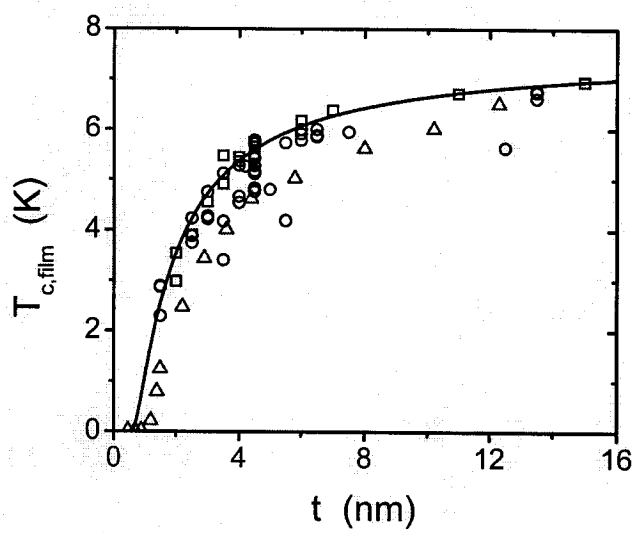

(b)

Figure 4.2: Comparison of film critical temperature vs. film thickness for bare MoGe films (○), Si coated MoGe films (□), and Si coated MoGe films from Graybeal's thesis (△) [1]. In (b), the film thickness for the bare MoGe films is shifted by 2.5 nm. Solid line is a fit to theory by Oreg and Finkel'stein [5].

samples as Graybeal did. The reason we do not is that it was found that top coating with Si produces significantly less homogeneous nanowires, as will be discussed in Chapter 6.

Reproduced with permission of the copyright owner. Further reproduction prohibited without permission.

Typically a few samples are sputtered together at the same time during fabrication but are measured one-by-one. Therefore, each sample ages for a different amount of time before measurement leading to different effective thicknesses due to the slow oxidation of the "bare" MoGe. This is the cause of the spread in our data. We can rule out the possibility that the sputtering equipment or methods we used are poor by observing that test films we fabricate that do have a Si top layer show higher critical temperatures than Graybeal's films (Fig. 4.2(a)). This implies that we are able to produce MoGe films that are actually of *better* quality than Graybeal's. We estimate that the average effective thickness for our samples is reduced by 2.5 nm from the sputtered thickness as shifting the entire data set by this amount yields good agreement between our nanowire samples and the test films with Si top coating (Fig. 4.2(b)).

The morphology of a film is also known to affect its critical temperature. As sheet resistance increases, i.e. film thickness decreases, $T_{C,film}$ is observed to decrease for homogeneous films but remain constant for granular ones [2-4]. In Fig. 4.2(b) it is clear that the critical temperature of our films decreases with film thickness. Furthermore, we also show that our $T_{C,film}$ vs. t data can be fit by a theory of critical temperature suppression due to increased Coulomb repulsion in homogeneously disordered systems [5]. In the case of 2D films, the suppression is given by

$$\ln\left(\frac{T_{C,film}}{T_{C0}}\right)=\frac{1}{|\gamma|}-\frac{1}{2\sqrt{ut_{OF}}}\ln\frac{1+\sqrt{ut_{OF}}/|\gamma|}{1-\sqrt{ut_{OF}}/|\gamma|} \tag{4.1}$$

where T_{C0} is the bulk critical temperature, $t_{OF}=\left(e^2/2\pi^2\hbar\right)R_{\square}$ with $R_{\square}$ being the sheet resistance, u is a parameter describing the amplitude of the electron-electron interactions and is equal to 1/2 for MoGe [5], and γ is a parameter describing the amplitude of

Reproduced with permission of the copyright owner. Further reproduction prohibited without permission.

electron scattering in the Cooper channel. We took $|\gamma|$ as the only fitting parameter in our fit shown in Fig. 4.2(b) and found $|\gamma| = 0.143$, which is very similar to the case of amorphous Pb for which $|\gamma| = 0.16$ [5]. As the theory is constructed for homogeneous systems, we take such good agreement between data and theory as further proof of the non-granularity of our MoGe films.

4.1.3 Nanowire resistivity

Another way we can test the quality of our samples is to examine their resistivity. To do this we need to know their lengths, L, and cross-sectional areas, A. The shape of the wires' cross-section, however, remains unclear and can vary from sample to sample as the underlying template may be constructed of a single fluorinated single walled carbon nanotube (FSWNT) or a rope of many FSWNTs. If the template were a single FSWNT one might expect that the width, w, measured under SEM would be about twice the sputtered MoGe thickness. In the inset to Fig. 4.3, we plot width vs. thickness and find that this is not strictly the case, although the *range* of widths is about twice the range of thicknesses. Usually w is found to be a little larger than $2t$, indicating that frequently the templates are ropes of FSWNTs.

Even though we cannot determine it exactly we can estimate the cross-sectional area by $A = wt$. In Fig. 4.3 we show R_N/L vs. wt where the effect of oxidation described in the preceding section has been taken into account by reducing the widths and thicknesses by the appropriate amounts of 5 nm and 2.5 nm, respectively. A fit of the form $R_N/L = \rho/wt$ is also shown in Fig. 4.3 from which we determine $\rho = 174.9 \pm 12.2$ μΩ-cm. This is in excellent agreement with previously published values

Reproduced with permission of the copyright owner. Further reproduction prohibited without permission.

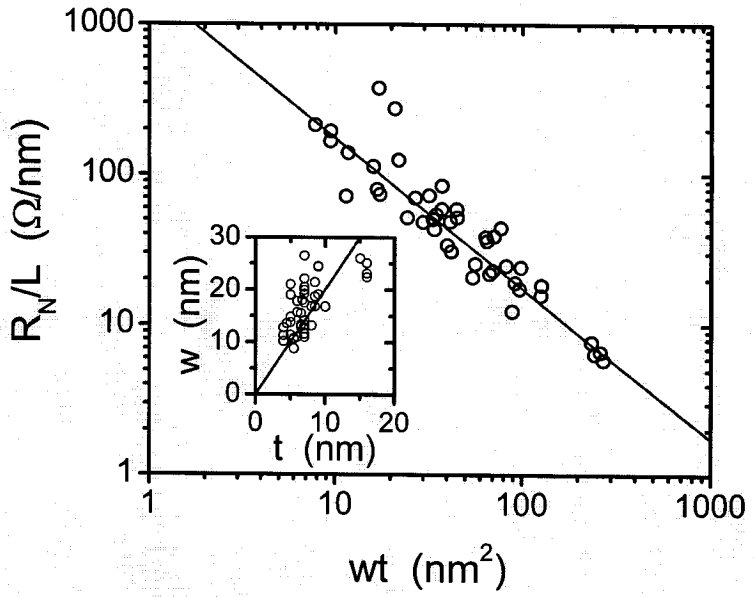

Figure 4.3: Normal state resistance divided by length vs. width times thickness for all nanowires (symbols). The effect of oxidation has been included as described in the text. The line is a fit of the form $R_N/L = \rho/wt$ where the resistivity was determined to be 174.9 ± 12.2 μΩ-cm. (inset) Width vs. thickness for all samples (symbols). Solid line is $w = 2t$.

of resistivity for bulk MoGe, MoGe thin films, and MoGe nanowires fabricated by molecular templating where the resistivity was reported to be 165 μΩ-cm [1], about 170 μΩ-cm (depending on film thickness) [1], and 180 μΩ-cm [6], respectively. The agreement between these values indicates that the wires we fabricate are indeed of good quality and free of excessive impurities or granularity.

4.2 R(T) behavior of superconducting nanowires

Now that we have established the quality of our samples we turn our attention to the results on superconducting nanowires. As mentioned above, one of the defining

Reproduced with permission of the copyright owner. Further reproduction prohibited without permission.

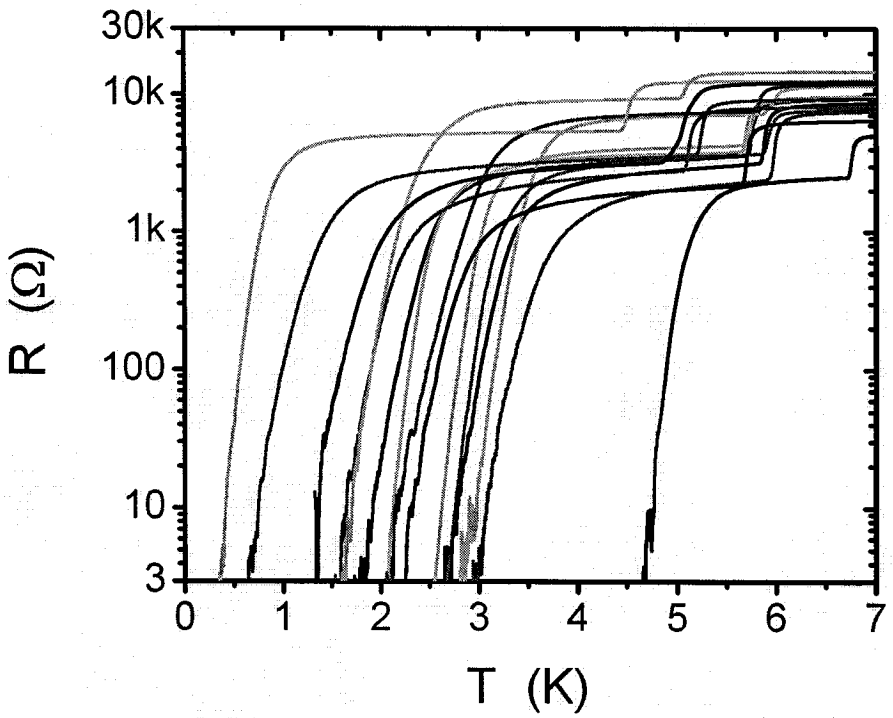

Figure 4.4: Resistance vs. temperature curves for the superconducting samples.

characteristics of the wires that is used to determine what state they are in is their $R(T)$ behavior. We have measured the $R(T)$ curves for a large set of MoGe nanowires as described in Chapter 3. The resistance vs. temperature data for those wires in the superconducting phase of the SIT are shown in Fig. 4.4. All samples show resistance that decreases faster than exponentially as temperature is lowered, with no observation of any resistive "tails" at the lowest temperatures. The behavior that they display is very similar to that observed in the experiments on a smaller set of MoGe nanowires by Bezryadin, Lau, and Tinkham [6] and on Nb nanowires by Rogachev and Bezryadin [7], both experiments we discussed previously (Figs. 2.9(a) and 2.10). In what follows we

Reproduced with permission of the copyright owner. Further reproduction prohibited without permission.

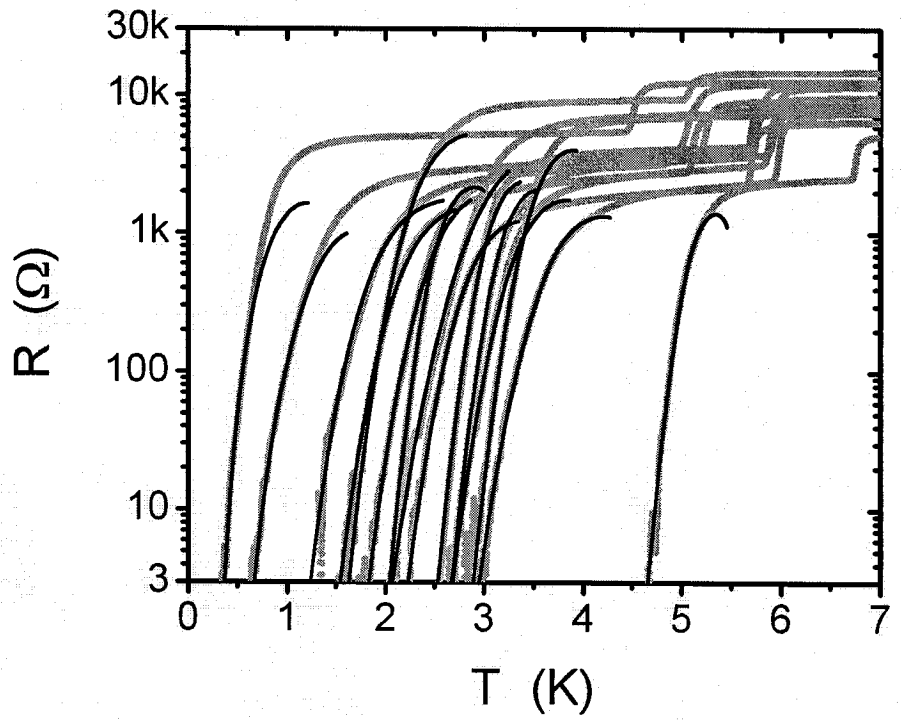

Figure 4.5: Comparison of resistance vs. temperature data (symbols) to the predictions of the LAMH theory (lines) for the superconducting samples.

compare our data with theories of thermally activated phase slips (TAPS) and quantum phase slips (QPS).

4.2.1 Comparison with the LAMH theory

The first theory we will compare our data to is that by Langer, Ambegaokar, McCumber, and Halperin (LAMH) for thermally activated phase slips. The theoretical derivation was discussed at length in Chapter 2 and we simply restate here that the resistance predicted by the LAMH theory is (Eq. 2.40)

$$R_{LAMH}(T) = \frac{8L\sqrt{c}}{\pi\xi(0)} R_Q \left(\frac{T}{T_C}\right)^{-3/2} \left(1-\frac{T}{T_C}\right)^{9/4} \exp\left[-c\frac{T_C}{T}\left(1-\frac{T}{T_C}\right)^{3/2}\right] \qquad (4.2)$$

Reproduced with permission of the copyright owner. Further reproduction prohibited without permission.

where L is the length of the wire, $\xi(0)$ is the Ginzburg-Landau coherence length at zero temperature, $R_Q = h/4e^2$ is the quantum of resistance for Cooper pairs, and the parameter c was defined in Eq. 2.30 as

$$c \equiv \frac{\sqrt{2}\pi}{3e^{\gamma}} \frac{R_Q}{R_N} \frac{L}{\xi(0)} \simeq 0.83 \frac{R_Q}{R_N} \frac{L}{\xi(0)} \tag{4.3}$$

In Fig. 4.5 we show the measured $R(T)$ curves from Fig. 4.4 along with fits to the LAMH theory using the function $R^{-1}(T) = R_N^{-1}(T) + R_{LAMH}^{-1}(T)$ [10]. An excellent agreement with the predictions of the LAMH theory is found for all samples, strongly suggesting that the only mechanism responsible for resistance in these wires is from TAPS. Only two fitting parameters were used in these fits – the critical temperature of the wire, T_C, and the Ginzburg-Landau coherence length at zero temperature, $\xi(0)$. The fitting parameters used are shown in Fig. 4.6. For samples with $R_N < 6\,\text{k}\Omega$, T_C is found to decrease approximately linearly with increasing R_N (Fig. 4.6(a)). The coherence lengths vary somewhat from sample to sample but most are found to be about ~7 nm, which is close to the value $\xi(0) = 4.9$ nm obtained for thin MoGe films [1].

Usually, the temperature dependence for the thermodynamic critical field near T_C, $H_C(T) \propto 1 - T/T_C$ (Eq. 2.5), was used in the equation for the LAMH free energy barrier (Eq. 2.4)

$$\Delta F(T) = \frac{8\sqrt{2}}{3} \frac{H_C^2(T)}{8\pi} A\xi(T) \tag{4.4}$$

where A is the cross-sectional area of the wire, to obtain the temperature dependence $\Delta F(T) \propto (1 - T/T_C)^{3/2}$ (since $\xi(T) \propto (1 - T/T_C)^{-1/2}$). One slight modification was made

Reproduced with permission of the copyright owner. Further reproduction prohibited without permission.

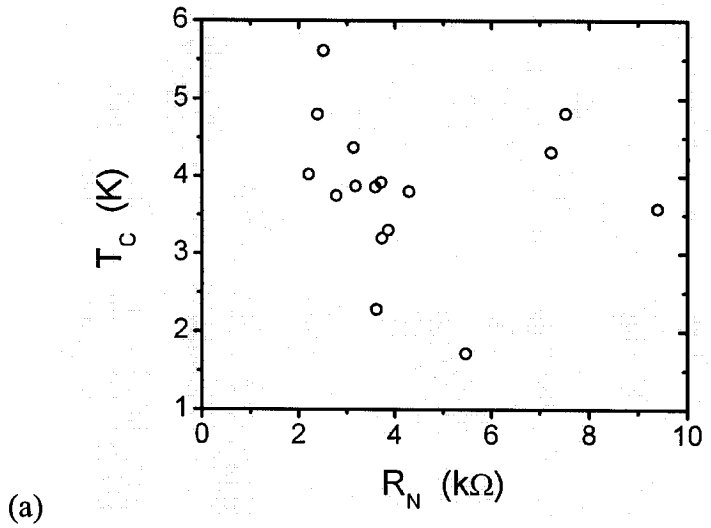

(a)

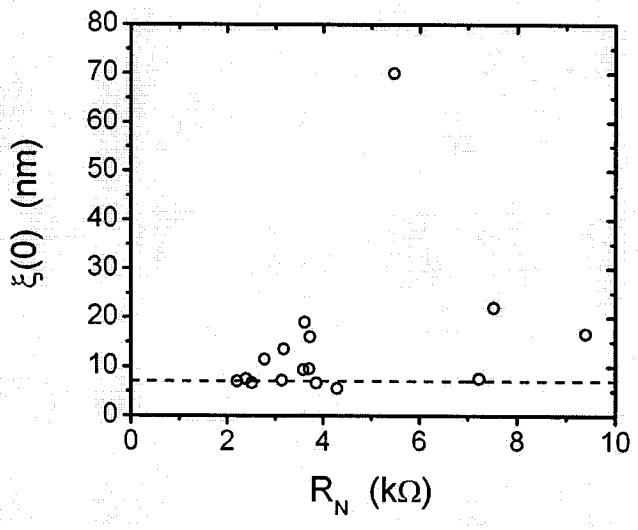

(b)

Figure 4.6: Fitting parameters used in fits to LAMH theory. (a) Critical temperature vs. normal state resistance. (b) Ginzburg-Landau coherence length at zero temperature vs. normal state resistance. The dashed line is $\xi(0) = 7$ nm.

here for the two samples with the lowest T_C. For these samples we have used $H_C(T) \propto 1-(T/T_C)^2$ [11]. This form is more appropriate over a larger range of values for T/T_C, which is the case for these two samples. The reason we made this change over

Reproduced with permission of the copyright owner. Further reproduction prohibited without permission.

the traditionally used formula is that fits using the traditional formula required unrealistic fitting parameters, namely $T_C \approx T_{C,film}$ and $\xi(0) \approx L$.

4.2.2 Comparison with QPS theories

The excellent agreement with the LAMH theory seems to indicate that quantum phase slips do not provide any contribution to the resistance. However, we should like to compare our data to the models of QPS by Giordano [12] and Golubev and Zaikin [13] to verify that this is the case.

In Chapter 2 we found that the resistance due to QPS according to the model of Giordano [12] was given as (Eq. 2.44)

$$R_{MQT} = aR_Q \frac{\hbar}{k_B T} \frac{L}{\xi} \left(\frac{\Delta F}{\hbar/\tau_S} \right)^{1/2} \frac{1}{\tau_S} \exp\left(-\frac{b\Delta F}{\hbar/\tau_S} \right) \tag{4.5}$$

where $\tau_S = \pi\hbar/8k_B(T_C - T)$ is the Ginzburg-Landau time and a and b are numerical constants of order unity. In Fig. 4.7 we show the measured $R(T)$ curves from Fig. 4.4 along with fits to Giordano's model using the function $R^{-1}(T) = R_N^{-1}(T) + \left(R_{LAMH}(T) + R_{MQT}(T)\right)^{-1}$ [14, 15]. For these fits we use the values for T_C and $\xi(0)$ obtained from the fits to LAMH theory. In Fig. 4.7(a) we set $a = b = 1$ whereas in Fig. 4.7(b) we use $a = 7.2$ and $b = 1.3$, which are the values that were found by Lau *et al.* [14] that best fit their data on MoGe nanowires. It is clear that the model of Giordano does not describe the $R(T)$ behavior of our wires very well at all as it predicts resistive "tails" at the lowest temperatures, which are not observed in our measurements.

Reproduced with permission of the copyright owner. Further reproduction prohibited without permission.

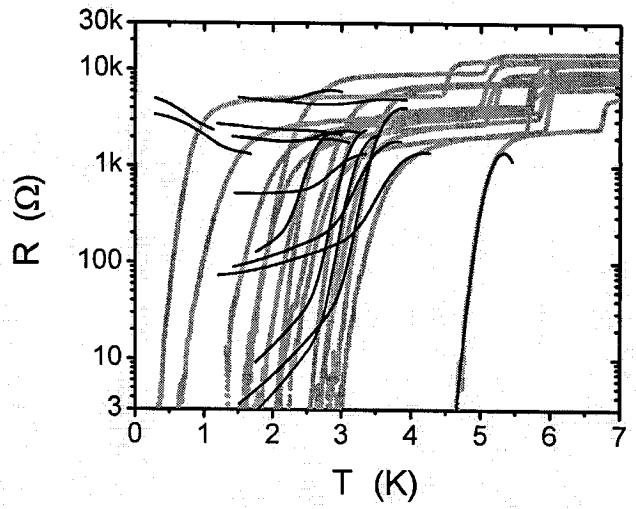

(a)

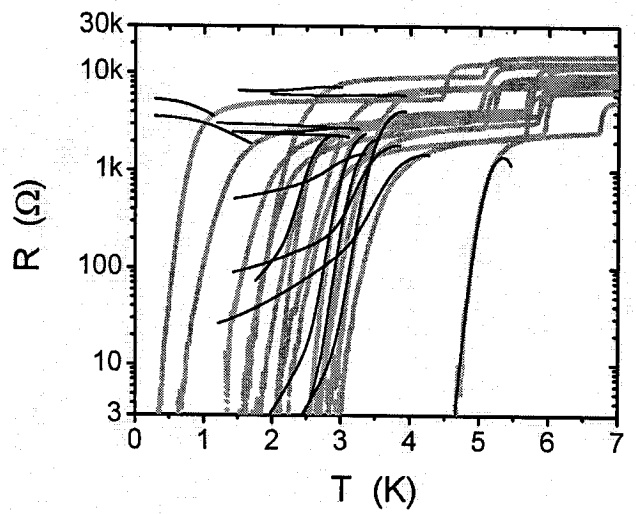

(b)

Figure 4.7: Resistance vs. temperature data (grey symbols) compared to predictions of Giordano's model of MQT (black lines). (a) The values $a=1$ and $b=1$ were used in fitting all the curves. (b) The values $a=7.2$ and $b=1.3$ were used.

A similar disagreement is found for the theory of QPS by Golubev and Zaikin [13]. In Fig. 4.8 we show the measured $R(T)$ curves from Fig. 4.4 along with fits to their theory using the function $R^{-1}(T)=R_N^{-1}(T)+\left(R_{LAMH}(T)+R_{GZ}(T)\right)^{-1}$ [15]. Here we

Reproduced with permission of the copyright owner. Further reproduction prohibited without permission.

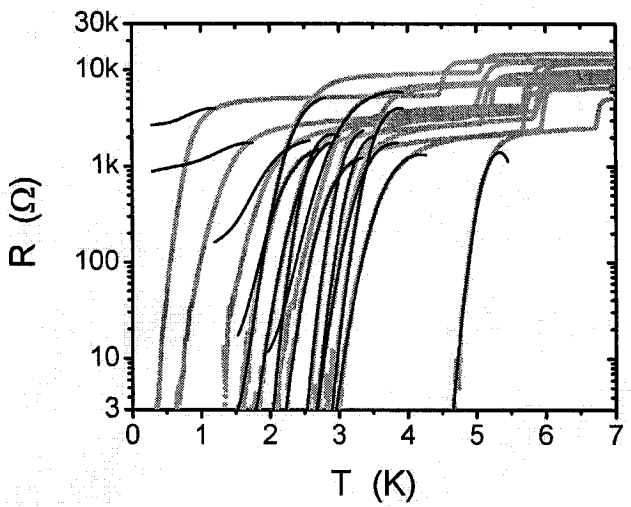

(a)

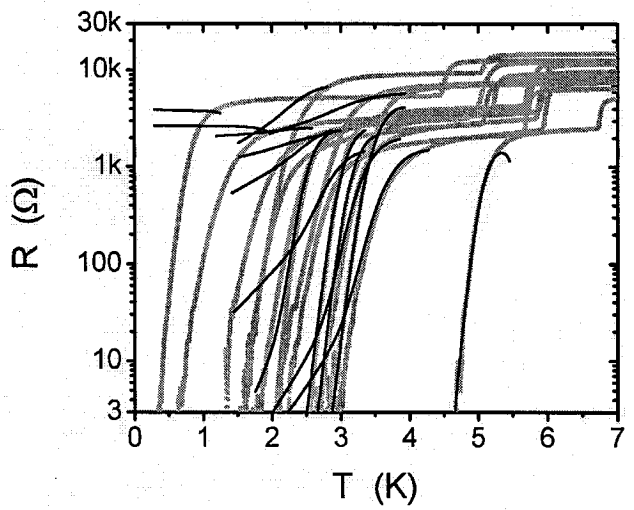

(b)

Figure 4.8: Resistance vs. temperature data (grey symbols) compared to predictions of Golubev and Zaikin's model of QPS (black lines). (a) The values $A_{GZ}=1$ and $B_{GZ}=1$ were used in fitting all the curves. (b) The values $A_{GZ}=0.52$ and $B_{GZ}=1.4$ were used.

follow Lau's [15] example and use (Eq. 2.51)

$$R_{GZ}(T)=B_{GZ}R_Q\frac{R_Q}{R_N}\left[\frac{L}{\xi(0)}\right]^2\left(1-\frac{T}{T_C}\right)\exp\left[-\frac{A_{GZ}R_QL}{R_N\xi(0)}\left(1-\frac{T}{T_C}\right)^{1/2}\right] \qquad (4.6)$$

Reproduced with permission of the copyright owner. Further reproduction prohibited without permission.

where A_{GZ} and B_{GZ} are constants of order unity. Again, we use the values for T_C and $\xi(0)$ obtained from the fits to LAMH theory. In Fig. 4.8(a) we set $A_{GZ} = B_{GZ} = 1$ whereas in Fig. 4.8(b) we use $A_{GZ} = 0.52$ and $B_{GZ} = 1.4$, which are the values that were found by Lau [15] that best fit her data on MoGe nanowires. Again, the theory predicts tails due to extra dissipation from QPS that are not observed in our wires.

In conclusion, the $R(T)$ behavior of our nanowires is best described by the LAMH theory of thermally activated phase slips. The quantum phase slip models predict additional resistance from QPS at the lowest temperatures that we do not observe, suggesting that QPS do not occur in our wires. It could be the case that the length of the nanowire is an important factor in observing QPS. Our wires are relatively short compared to the wires used in studies that reported finding QPS [14 - 18] in which the wires had lengths $L \geq 1\ \mu m$.

4.3 V(I) behavior of superconducting nanowires

The voltage as a function of current, $V(I)$, behavior is another measure we can use to determine the state of a nanowire. Actually, it is the differential resistance, $dV(I)/dI$, that shows the dichotomy between the superconducting and insulating states best. In this section we will examine some of the $V(I)$ and $dV(I)/dI$ characteristics of superconducting nanowires.

4.3.1 V(I) curves

The $V(I)$ behavior at different temperatures of a representative superconducting nanowire is shown in Fig. 4.9(a). Other superconducting samples showed qualitatively

Reproduced with permission of the copyright owner. Further reproduction prohibited without permission.

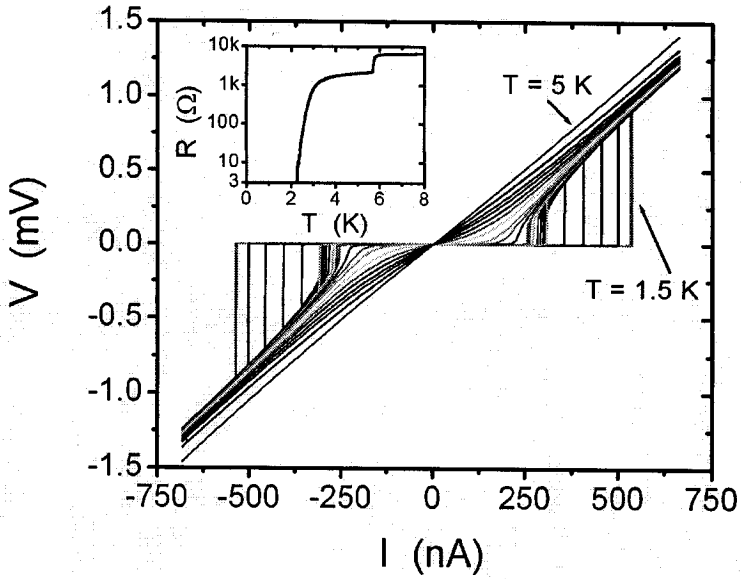

(a)

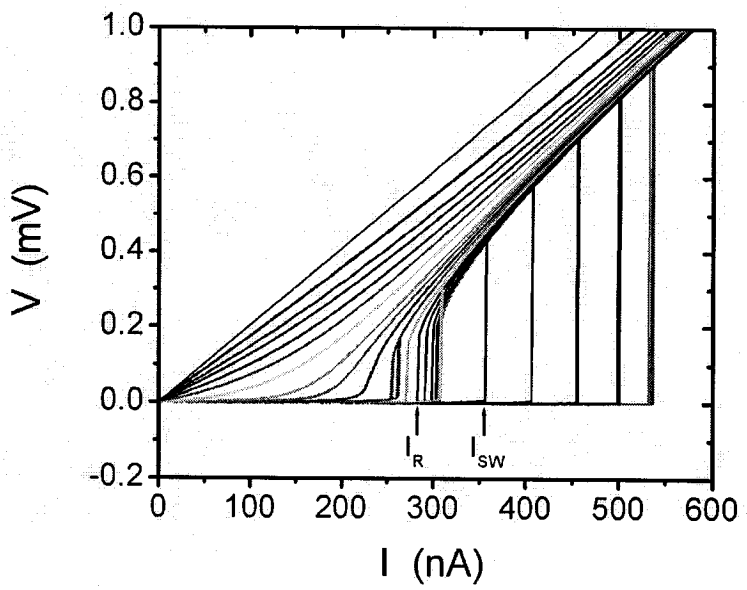

(b)

Figure 4.9: Voltage vs. current curves for sample 121204f. Temperatures are 1.5, 1.6, 1.7, 1.8, 1.9, 2.0, 2.1, 2.2, 2.3, 2.4, 2.6, 2.8, 3.0, 3.25, 3.5, 4.0, and 5.0 K. (a) Full scale $V(I)$ curves. (Inset) Resistance vs. temperature for same sample. (b) Zoomed in voltage vs. current curves from (a). The switching current, I_{SW}, and retrapping current, I_R, are shown for the curve taken at 1.9 K.

Reproduced with permission of the copyright owner. Further reproduction prohibited without permission.

the same behavior. At the highest temperature shown the wire is in the normal state and the $V(I)$ curve is essentially linear. As temperature decreases, the $V(I)$ curve becomes nonlinear and eventually develops a hysteresis loop at the lowest temperatures. This loop can be seen in more detail in Fig. 4.9(b) where we plot the same data from Fig. 4.9(a) just zoomed in. Upon first inspection these $V(I)$ curves look very similar to the case of an underdamped Josephson junction. As current increases from $I = 0$, the voltage remains immeasurably low (but not exactly zero due to thermal fluctuations) until at some high current, I_{SW}, the system switches to a resistive state, with a slope $dV(I)/dI \approx R_N$ at higher current. As current is then decreased back towards $I = 0$, the system remains in this resistive state until some retrapping current, I_R, is reached, below which the voltage becomes immeasurably low again. These two currents are shown in Fig. 4.9(b) for the curve taken at 1.9 K. Two important differences exist, however, between underdamped Josephson junctions and superconducting nanowires. First, the distribution of switching currents becomes narrower as temperature is lowered for the underdamped Josephson junctions [11] but it becomes wider for the superconducting nanowires. Second, again as temperature is lowered, the retrapping current decreases for Josephson junctions [11] but is found to increase for nanowires.

4.3.2 Retrapping and switching currents

A possible explanation for the difference in retrapping current behavior comes from Song [19]. When decreasing the current from some very high value back towards $I = 0$, once $I < I_{SW}$ the kinetic energy of the current is less than the depairing energy and so Cooper pairs should be able to form in a time $\tau_P \sim h/\Delta(T)$, where $\Delta(T)$ is the energy

Reproduced with permission of the copyright owner. Further reproduction prohibited without permission.

gap. However, Josephson oscillations occur with a period $\tau_J = h/2eV$ that accelerate the newly formed pairs to the critical depairing velocity and they are broken. When $\tau_P > \tau_J$ pairs are broken more quickly than they can form and so the condensate is destroyed. On the other hand, when $\tau_P < \tau_J$ pairs form at a rate that is quicker than they are broken and so condensation takes place and voltage drops to zero. The condition for this to occur then is $V < \Delta(T)/2e$. Since the energy gap for MoGe is about 1 meV this means retrapping should occur when $V \sim 0.5$ mV, which is what is observed in the experiments. Also, since $\Delta(T)$ increases quickly as temperature is lowered below T_C but then remains essentially constant for $T < 0.6T_C$, this explains why $I_R(T) \propto \Delta(T)$ increases for decreasing temperature and then remains constant for the lowest temperatures.

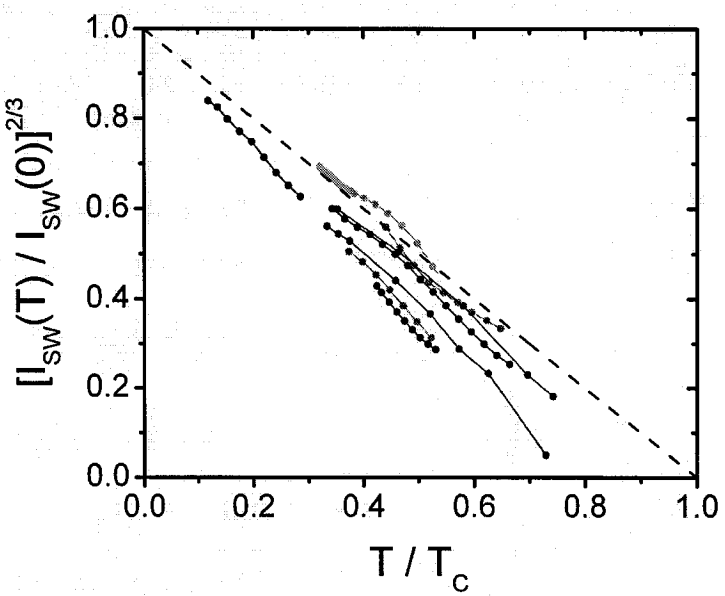

Figure 4.10: Switching current vs. temperature. Dashed line is $\left[I_{SW}(T)/I_{SW}(0)\right]^{2/3} = 1 - T/T_C$.

Reproduced with permission of the copyright owner. Further reproduction prohibited without permission.

The switching current for various samples as a function of temperature is shown in Fig. 4.10. The switching current at zero temperature was taken from extrapolation of I_{SW} vs. T curves and T_C was taken from LAMH fits. Given the uncertainty in determining $I_{SW}(0)$, the curves follow a $\left[I_{SW}(T)/I_{SW}(0)\right]^{2/3} = 1 - T/T_C$ rather nicely. This form comes from standard Ginzburg-Landau theory, by identifying the switching current with the critical current of the wire, for which it is expected that $I_C \propto (1 - T/T_C)^{3/2}$ [11]. The issue of the broadened switching current distribution is less understood and will be the basis for future work.

4.3.3 Differential resistance curves

Besides the zero-bias resistance, the differential resistance behavior of nanowires is the other trait we use to distinguish between superconducting and insulating samples. As indicated by their $V(I)$ behavior, superconducting wires always show a minimum near zero-bias on $dV(I)/dI$ curves, as opposed to the zero-bias maximum observed for insulating samples (Chapter 5). In Fig. 4.11 we show the $dV(I)/dI$ behavior for sample 121204f taken at 1.9 K. The switching current is seen as a jump-wise step up to the resistive state, preceded by a small upturn. This upturn is described more fully in the next section. The retrapping current also appears at a jump down to the low voltage state, preceded by a sharp increase in $dV(I)/dI$ that is clear from the $V(I)$ behavior.

Reproduced with permission of the copyright owner. Further reproduction prohibited without permission.

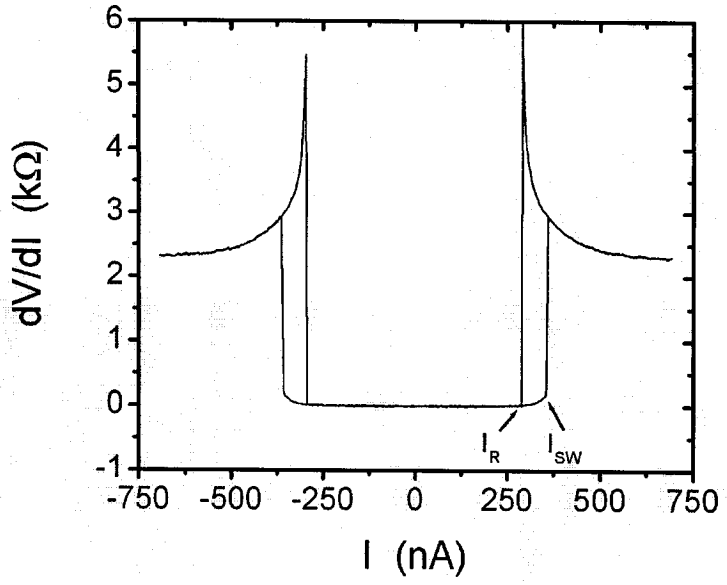

Figure 4.11: Differential resistance vs. bias current for sample 121204f at 1.9 K. The switching current, I_{SW}, and retrapping current, I_R, are indicated.

4.4 Effect of magnetic field on superconducting nanowires

The results and text of this section were published under the title "Influence of High Magnetic Fields on the Superconducting Transition of One-Dimensional Nb and MoGe Nanowires" and are repeated here. Reprinted with permission from Andrey Rogachev, Anthony T. Bollinger, and Alexey Bezryadin, Physical Review Letters **94,** 017004 (2005). Copyright 2005 by the American Physical Society.

The problem of superconductivity in one-dimensional (1D) systems attracts much attention since it involves such fundamental phenomena as macroscopic quantum tunneling, quantum phase transitions, and environmental effects [6, 7, 12-14, 20-30]. It is expected that a strong magnetic field can be used to control these phenomena. Indeed, the microscopic theory predicts that a magnetic field, acting on a superconducting condensate, lifts the time reversal symmetry of the spin and orbital states of paired

Reproduced with permission of the copyright owner. Further reproduction prohibited without permission.

electrons and suppresses the critical temperature, T_C [11, 31-33]. A strong enough field destroys superconductivity. The magnetic field pair-breaking effects were studied in depth in two and zero-dimensional systems, i.e., thin films [34, 35] and nanograins [36-38]. However, an experimental verification of the pair-breaking effects in 1D superconductors is long overdue.

A distinct feature of 1D superconductors is the absence of the phase coherence. Because of fluctuations the amplitude of the order parameter has a finite probability to reach zero at some point along the wire, allowing the phase of the order parameter to slip by 2π [39]. The theory of thermally activated phase slips was developed by Langer, Ambegaokar, McCumber, and Halperin (LAMH) [8, 9]. However, the effect of the magnetic field on the phase slippage process is not established. It is also unknown whether the magnetic field can change the relative contributions of quantum and thermally activated phase slips in thin wires [7, 14].

In this Letter we study the effects of the magnetic field on the phase slippage rate and the critical temperature of thin wires. It is found that the LAMH theory provides a good description for 1D superconductors in magnetic fields up to 11 T. The dependence of the critical temperature on the magnetic field, $T_C(B)$, agrees well with the theory of pairbreaking perturbations that takes into account both spin and orbital contributions [11, 31-33]. This is our main result. No significant contribution of quantum phase slips has been detected in the studied samples.

The samples were made by sputter coating of suspended fluorinated carbon nanotubes with Nb or $Mo_{79}Ge_{21}$. Transport measurements were performed in a He-3 cryostat, as described previously [6, 7, 24]. The magnetic field was oriented

Reproduced with permission of the copyright owner. Further reproduction prohibited without permission.

perpendicular to the wire and parallel to the thin film electrodes connected in series with the wire.

A series of resistance versus temperature $R(T)$ curves measured at different magnetic fields is shown in Fig. 4.12. For each curve, a resistance drop at higher temperature corresponds to a superconducting transition in the film electrodes. The resistance value immediately below the drop is taken as the wire normal resistance, R_N. The second resistive transition corresponds to the development of superconductivity in the wire. With increasing magnetic field, both transitions shift to lower temperatures.

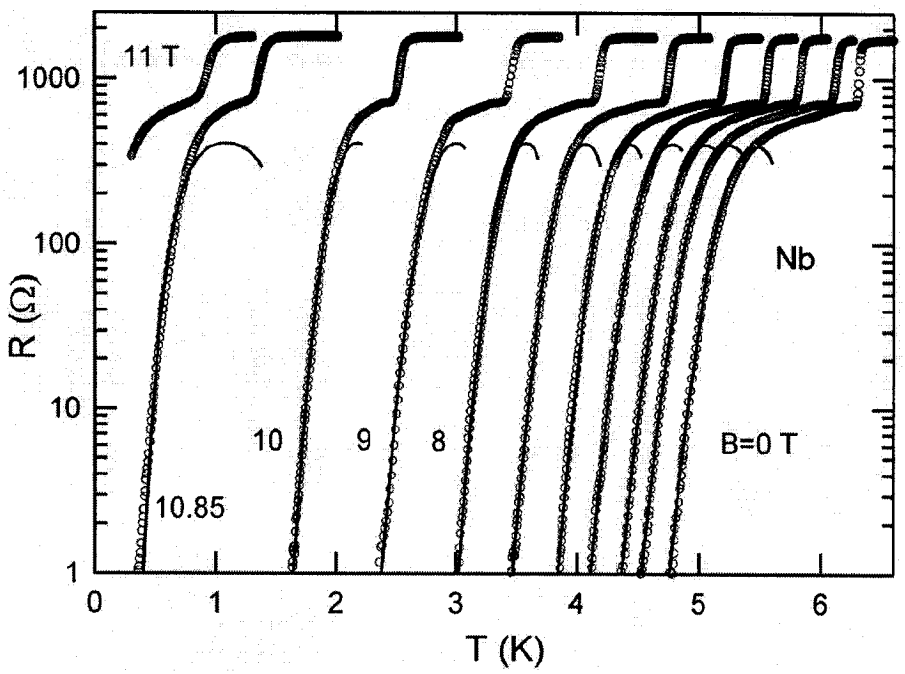

Figure 4.12: Resistance versus temperature dependence for a Nb nanowire (the thickness is 8 nm, the normal resistance is $R_N = 700\,\Omega$, and the length is $L = 120\,\text{nm}$). Each $R(T)$ curve is measured in a fixed magnetic field; some fields are indicated. Solid lines show the fits to the LAMH theory.

Reproduced with permission of the copyright owner. Further reproduction prohibited without permission.

To analyze these data we employ the LAMH expression for zero-bias resistance:

$$R_{LAMH}(T) = \frac{\pi\hbar^2\Omega}{2e^2 k_B T} e^{-\Delta F/k_B T} \tag{4.7}$$

where $\Delta F = \left(8\sqrt{2}/3\right)\left(H_C^2/8\pi\right)A\xi$ is the energy barrier, $\Omega = \left(L/\xi\right)\left(\Delta F/k_B T\right)^{1/2}\left(1/\tau_{GL}\right)$ is the attempt frequency, and $\tau_{GL} = \left[\pi\hbar/8k_B\left(T_C - T\right)\right]$ is the Ginzburg-Landau (GL) relaxation time, L is the length of the wire, A is its cross-sectional area, and ξ is the GL coherence length. Following Ref. [14] we express the energy barrier as

$$\Delta F(T) \approx 0.83\left[L/\xi(0)\right]\left(R_Q/R_N\right)k_B T_C\left(1 - T/T_C\right)^{3/2} \tag{4.8}$$

where $R_Q = h/4e^2 = 6.45\,\mathrm{k\Omega}$ is the resistance quantum for Cooper pairs and $\xi(0)$ is defined by $\xi(T) = \xi(0)\left(1 - T/T_C\right)^{-1/2}$. Taking into account the contribution of quasiparticles, the total resistance is given as $R = \left(R_N^{-1} + R_{LAMH}^{-1}\right)^{-1}$. In our fitting procedure we use two adjustable parameters, T_C and $\xi(0)$.

The LAMH fits are shown as solid lines in Fig. 4.12, for various magnetic fields. Although the LAMH theory is derived for $B = 0$, we find that the resistance agrees with the LAMH fits very well for both Nb and MoGe samples, even in high fields up to ~11 T.

Our extension of the LAMH theory to high magnetic fields requires an explanation: For a phase slip to occur in a wire, the system needs to overcome an energy barrier that is a product of the condensation energy density $\left(H_C^2/8\pi\right)$ in a volume of a phase slip $A\xi$. It can be shown within the GL theory that in magnetic field the condensation energy density goes to zero as $\left[1 - T/T_C(B)\right]^2$, where $T_C(B)$ is the field-

Reproduced with permission of the copyright owner. Further reproduction prohibited without permission.

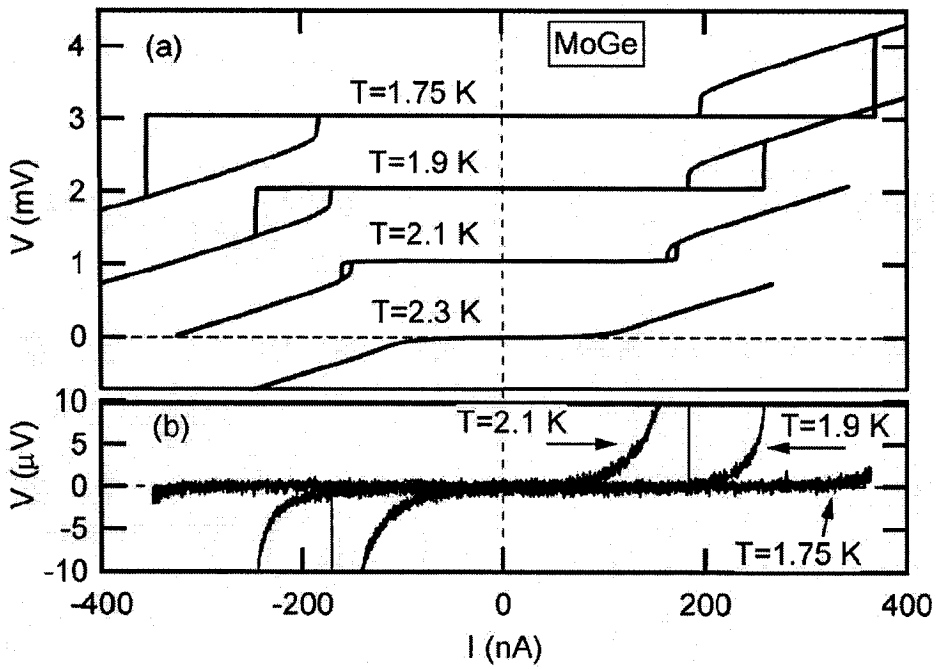

Figure 4.13: (a) Voltage versus current dependence at indicated temperatures for a MoGe nanowire (sample 031027m1, thickness 7 nm, $R_N = 4.3\,\mathrm{k\Omega}$, and $L = 190\,\mathrm{nm}$) at $B = 0$. The curves are vertically shifted by 1 mV for clarity. (b) The same data at a magnified scale.

dependent critical temperature. The coherence length varies as $\xi(0,B)\left[1-T/T_C(B)\right]^{-1/2}$ and diverges at $T_C(B)$. Because the temperature dependence of both the condensation energy and the coherence length has the same form as in zero field, we expect Eqs. 4.7 and 4.8 to be applicable in magnetic fields also. The observed agreement with the experiment suggests that the mechanism of the phase slippage in 1D wires is not changed by magnetic field.

To test the LAMH theory in a nonlinear regime, we performed measurements of the voltage-current $V(I)$ dependencies at high bias currents for some MoGe wires (Fig.

Reproduced with permission of the copyright owner. Further reproduction prohibited without permission.

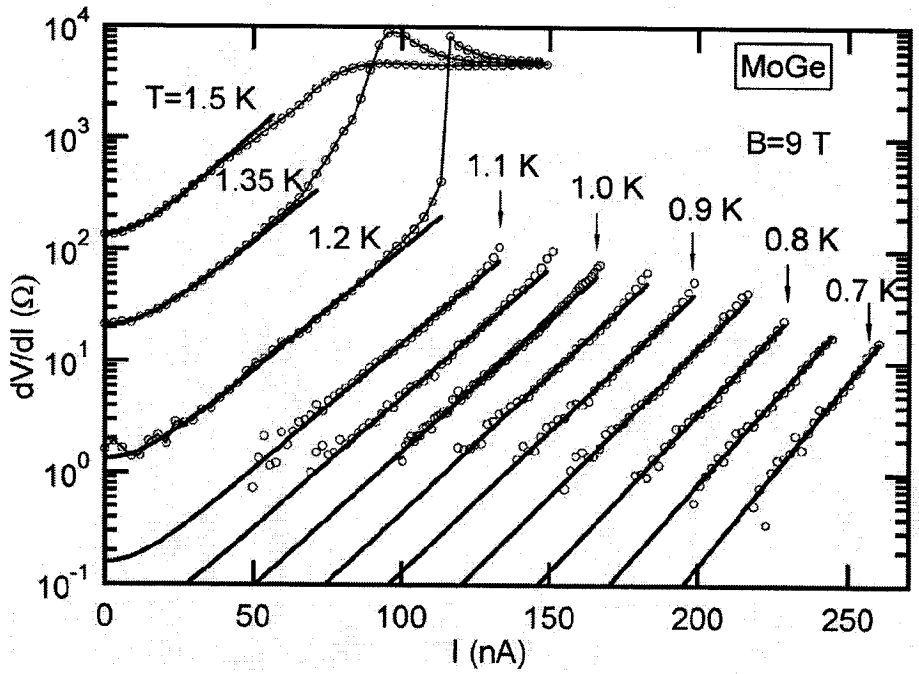

Figure 4.14: Differential resistance versus bias current at indicated temperatures for the MoGe nanowire (sample 031027m3, thickness 7 nm, $R_N = 3.9\,\mathrm{k}\Omega$, and $L = 150\,\mathrm{nm}$) in a fixed magnetic field $B = 9\,\mathrm{T}$. Solid lines are fits to the LAMH expression $dV/dI = R(T)\cosh(I/I_0)$.

4.13(a)). We observe that at high currents the wires undergo a transition into the resistive state. This transition is smooth at high temperatures and it is jumpwise, with some hysteresis, at low temperatures [7, 40, 41] (Fig. 4.13(a)). A closer inspection of the data revealed that even at low temperatures there exists a small nonlinear voltage variation at currents slightly lower than the switching current (Fig. 4.13(b)). The $V(I)$ curves remain qualitatively unchanged in magnetic field.

In order to investigate in more detail the resistive tails observed slightly below the switching current we measured the differential resistance dV/dI versus bias current I as shown in Fig. 4.14. It is clear that at all temperatures the dV/dI versus I data follow

Reproduced with permission of the copyright owner. Further reproduction prohibited without permission.

exponential dependence, which is expected from the LAMH expression $dV/dI = R(T)\cosh(I/I_0)$, where $R(T)$ is the zero-bias resistance given by Eq. 4.7 and $I_0 = 4ek_BT/h$. We fit the data with the above expression and extract two adjustable parameters $R(T)$ and I_0. Experimental values of I_0 are close to the theoretical value $I_0 = 4ek_BT/h$ (Fig. 4.15(inset)). We speculate that the observed small upward deviation of I_0 might be due to the fact that some fraction of the bias current is carried by

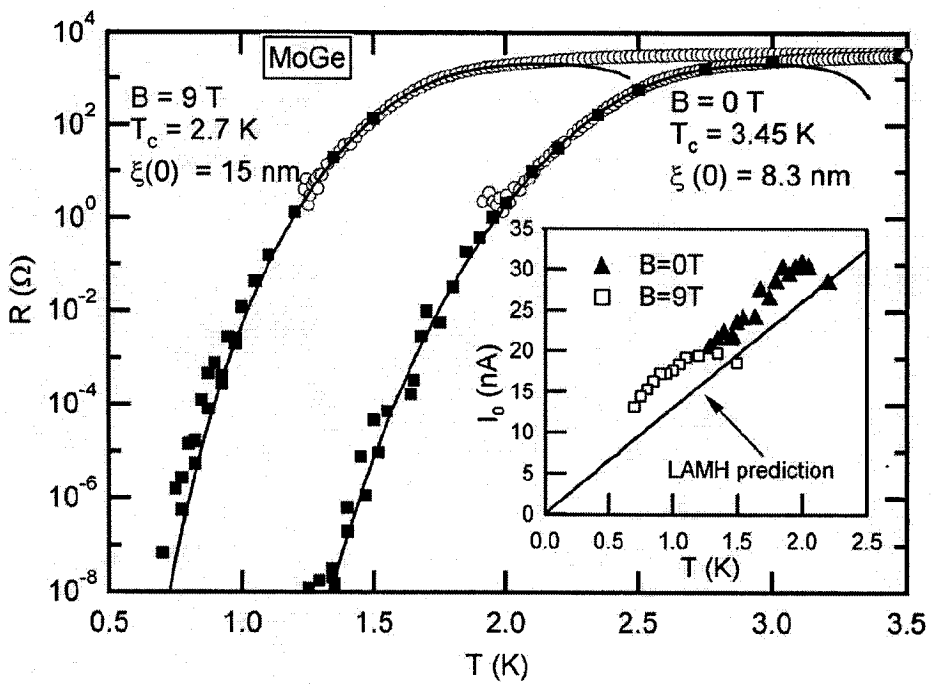

Figure 4.15: Resistance versus temperature for the MoGe nanowire (sample 031027m3, same as in Fig. 4.14) in magnetic fields 0 and 9 T. Open circles represent zero-bias-current measurements and black squares indicate the resistance values obtained from the fit of the nonlinear portion of dV/dI curves (Fig. 4.14). Solid lines are the fits to the LAMH theory. Extracted fitting parameters T_C and $\xi(0)$ are indicated. The inset shows the experimental dependence of the parameter I_0 on temperature (solid and open symbols) and the theoretical value $I_0 = 4ek_BT/h$ (solid line).

Reproduced with permission of the copyright owner. Further reproduction prohibited without permission.

nonequilibrium quasiparticles. Such quasiparticles are generated by the phase slips and are not taken into account within the LAMH theory. A detailed theoretical analysis is needed for further understanding of the $I_0(T)$ behavior.

In Fig. 4.15 we superimpose the zero-bias resistance data and the resistance data obtained from the fits to the nonlinear portion of dV/dI vs I curves. These two sets of data appear mutually consistent. The LAMH fit (solid lines in Fig. 4.15) gives an excellent description of all resistance data in a range of *11 orders of magnitude*. We also find good agreement with the LAMH theory for data taken in magnetic field $B = 9\,\mathrm{T}$ (Fig. 4.15). It is therefore concluded that the resistance in studied nanowires is determined by thermally activated phase slips even in high magnetic fields.

In Fig. 4.16 we plot the extracted parameters $T_C(B)$ and $\xi(0,B)$ versus magnetic field. The coherence length increases very slowly in low fields and starts to grow more rapidly at $B > 8\,\mathrm{T}$. We consider now the critical temperature $T_C(B)$, which is the main focus of this work. Although the initial decrease of T_C agrees with the variation predicted by the GL theory (Fig. 4.16(a)), it is clear that the GL phenomenology is not sufficient to account for the observed $T_C(B)$ dependence. One possible reason is that the GL theory does not take into account the spin pair-breaking effect and the coefficients of the GL theory can change in the high field regime. Thus we have to use the exact theory of pair breaking [31-33]. In both Nb and MoGe nanowires superconductivity persists to magnetic fields that are larger than the paramagnetic limit, $B_P[\mathrm{T}] = 1.84 T_C[\mathrm{K}]$ [11] (10.6 T for Nb and 8.1 T for MoGe). Since the superconductivity is not fully suppressed at such fields, we conclude that the effect of magnetic field on the spin part of the Cooper

Reproduced with permission of the copyright owner. Further reproduction prohibited without permission.

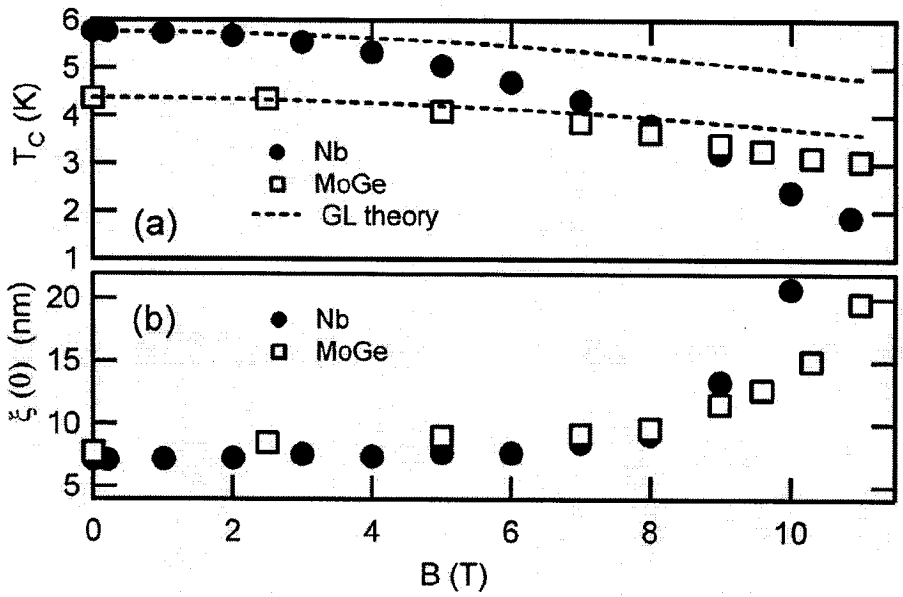

Figure 4.16: Adjustable parameters used in the LAMH fits of the type shown in Fig. 4.12. (a) The critical temperature versus magnetic field $T_C(B)$ is shown for the Nb wire (same as in Fig. 4.12) and for a MoGe wire. The theoretical Ginzburg-Landau dependence is indicated by dashed lines. (b) The GL coherence length versus magnetic field. The parameters of the MoGe wire (sample 020904d)are that thickness is 9 nm, $R_N = 7.5\,\text{k}\Omega$, and $L = 460\,\text{nm}$.

pair is reduced by the spin-orbit scattering, as expected for materials with high atomic numbers. If the spin-orbit scattering is sufficiently strong, the transition into the normal state is continuous. This allows us to take into account both the spin and the orbital effects on T_C in an implicit relation of the theory of pair-breaking perturbations [11]

$$\ln\frac{T_C(B)}{T_C(0)} = \psi\left(\frac{1}{2}\right) - \psi\left(\frac{1}{2} + \frac{\alpha_o + \alpha_s}{2\pi k_B T_C(B)}\right) \tag{4.9}$$

where $\psi(z)$ is the digamma function and $\alpha_o = 2De^2\langle A^2\rangle/\hbar c^2$ and $\alpha_s \approx \tau_{so}e^2\hbar B^2/2m^2c^2$ are the orbital and the spin pair-breaker strength parameters, D is

Reproduced with permission of the copyright owner. Further reproduction prohibited without permission.

the diffusion coefficient, and τ_{so} is the spin-orbit scattering time. To find the vector potential averaged over the cross-sectional area of a wire, $\langle A^2 \rangle$, we use the expression for a cylinder in perpendicular magnetic field, $\langle A^2 \rangle = B^2 d^2/16$, where d is the diameter of the wire.

By solving Eq. 4.9 numerically the theoretical dependence of the normalized critical temperature versus the normalized magnetic field is obtained. In Fig. 4.17 this dependence is compared to the experimental values of $T_C(B)/T_C(0)$ [same data as in Fig. 4.16(a)]. Since both pair breakers, α_o and α_s, have a quadratic dependence on B, only one adjustable parameter is required, which is the critical field of the wire at zero

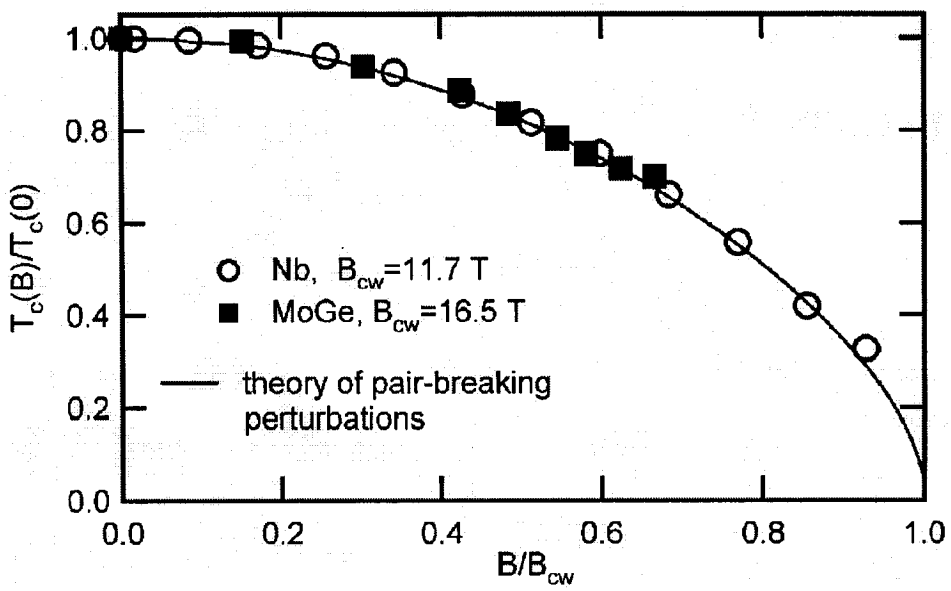

Figure 4.17: Normalized critical temperature versus normalized magnetic field for the Nb and MoGe wires. Critical magnetic fields (B_{cw}) for both wires are indicated. The solid line is a fit to the theory of pair-breaking perturbation (Eq. 4.9).

Reproduced with permission of the copyright owner. Further reproduction prohibited without permission.

temperature, B_{cw}. The best fits are obtained by choosing $B_{cw} = 11.7$ T for Nb and 16.5 T for MoGe (Fig. 4.17).

To compare orbital and spin pair-breaking contributions we introduce an orbital critical field (B_{co}) and a spin critical field (B_{cs}), defined as fields needed to suppress superconductivity if only one of the two pair-breaking mechanisms is present. These fields are obtained from equations $2\alpha_o = 2\alpha_s = 1.76 k_B T_C(0)$ [11]. The total critical field is then $B_{cw} = \left(B_{co}^{-2} + B_{cs}^{-2}\right)^{-1/2}$. Using BCS and GL relations the orbital critical field can be written as $B_{co} = 0.53\Phi_0 / d\xi(0)$, where Φ_0 is the flux quantum. The value of the coherence length $\xi(0)$ is known from the LAMH fit in zero field (7.1 nm for Nb and 7.7 nm for MoGe). Taking d as the thickness of the deposited material (corrected for oxidation for the MoGe wire [24]) we estimate $B_{co} \approx 22$ T for both wires. From B_{co} and experimental total critical field B_{cw} we determine the spin critical fields, $B_{cs} \approx 14$ T for Nb and $B_{cs} \approx 25$ T for MoGe. Thus the spin and orbital pair breakers have comparable strengths.

From the B_{cs} we estimate the spin-orbit scattering time as $\tau_{so} = 2.3 \pm 0.5 \times 10^{-13}$ s for the Nb wire and $\tau_{so} = 5 \pm 3 \times 10^{-14}$ s for the MoGe wire. The MoGe result is considerably different from the value $\tau_{so} \simeq 1.3 \times 10^{-12}$ s obtained for thin MoGe films from weak localization measurements [1]. With such a τ_{so} value the superconductivity in the MoGe wire would be completely suppressed at $B_{cs} \simeq 5$ T, contrary to our observation. On the other hand, we can use the formula $\tau_{so} \simeq \tau\left(\hbar c / Ze^2\right)^4$ given in Ref.

Reproduced with permission of the copyright owner. Further reproduction prohibited without permission.

[42]. With elastic scattering time $\tau \simeq 6\times10^{-16}$ s [1] this gives a shorter spin-orbit scattering time 8×10^{-14} s, that agrees with our result. The latter estimate also works well for the Nb nanowire. Here we have elastic time $\tau = \ell/v_F \simeq 1.9\times10^{-15}$ s ($v_F = 0.62\times10^{-8}$ cm/s [43], $\ell = 1.2$ nm [7]), and so $\tau_{so} \simeq 2.4\times10^{-13}$ s, again in agreement with the experimental value. Thus we conclude that the pair-breaking theory combining spin and orbital contributions gives an accurate quantitative prediction for the suppression of the critical temperature of homogeneous 1D superconducting wires.

4.5 References

[1] J. M. Graybeal and M. R. Beasley, Phys. Rev. B **29**, 4167 (1984); J. M. Graybeal, Ph.D. thesis, Stanford University, 1985.

[2] H. M. Jaeger, D. B. Haviland, A. M. Goldman, and B. G. Orr, Phys. Rev. B **34**, 4920 (1986).

[3] D. B. Haviland, Y. Liu, and A. M. Goldman, Phys. Rev. Lett. **62**, 2180 (1989).

[4] A. Frydman, Physica C **391**, 189 (2003).

[5] Y. Oreg and A. M. Finkel'stein, Phys. Rev. Lett. **83**, 191 (1999).

[6] A. Bezryadin, C. N. Lau, and M. Tinkham, Nature **404**, 971 (2000).

[7] A. Rogachev and A. Bezryadin, Appl. Phys. Lett. **83**, 512 (2003).

[8] J. S. Langer and V. Ambegaokar, Phys. Rev. **164**, 498 (1967).

[9] D. E. McCumber and B. I. Halperin, Phys. Rev. B **1**, 1054 (1970).

[10] R. S. Newbower, M. R. Beasley, and M. Tinkham, Phys. Rev. B **5**, 864 (1972).

[11] M. Tinkham, *Introduction to Superconductivity*, 2nd ed. (McGraw-Hill, New York, 1996).

Reproduced with permission of the copyright owner. Further reproduction prohibited without permission.

[12] N. Giordano, Phys. Rev. Lett. **61**, 2137 (1988).

[13] D. S. Golubev and A. D. Zaikin, Phys. Rev. B **64**, 014504 (2001).

[14] C. N. Lau, N. Markovic, M. Bockrath, A. Bezryadin, and M. Tinkham, Phys. Rev. Lett. **87**, 217003 (2001).

[15] C. N. Lau, Ph.D. thesis, Harvard University, 2001.

[16] M. Tian, J. Wang, J.S. Kurtz, Y. Liu, M.H.W. Chan, T.S. Mayer, and T.E. Mallouk, Phys. Rev. B **71**, 104521 (2005).

[17] M. Zgirski, K.-P. Riikonen, V. Touboltsev, and K. Arutyunov, Nano Lett. **5**, 1029 (2005).

[18] F. Altomare, A. M. Chang, M. R. Melloch, Y. Hong, and C. W. Tu, cond-mat/0505772 (2005).

[19] Y. Song, J. Appl. Phys. **47**, 2651 (1976).

[20] J. M. Duan, Phys. Rev. Lett. **74**, 5128 (1995).

[21] K. A. Matveev, A. I. Larkin, and L. I. Glazman, Phys. Rev. Lett. **89**, 096802 (2002).

[22] A. D. Zaikin, D. S. Golubev, A. van Otterlo, G. T. Zimányi, Phys. Rev. Lett. **78**, 1552 (1997).

[23] G. Rafael, E. Demler, Y. Oreg, and D. S. Fisher, Phys. Rev. B **68**, 214515 (2003).

[24] A. T. Bollinger, A. Rogachev, M. Remeika, and A. Bezryadin, Phys. Rev. B **69**, 180503(R) (2004).

[25] B. Camarota, F. Parage, F. Balestro, P. Delsong, and O. Buisson, Phys. Rev. Lett. **86**, 480 (2001).

Reproduced with permission of the copyright owner. Further reproduction prohibited without permission.

[26] H. P. Büchler, V. B. Geshkenbein, and G. Blatter, Phys. Rev. Lett. **92**, 067007 (2004).

[27] S. Sachdev, P. Werner, and M. Troyer, Phys. Rev. Lett. **92**, 237003 (2004).

[28] S. Khlebnikov, Phys. Rev. Lett. **93**, 090403 (2004).

[29] R. A. Smith, B. S. Handy, and V. Ambegaokar, Phys. Rev. B **63**, 094513 (2001).

[30] P. Xiong, A. V. Herzog, and R. C. Dynes, Phys. Rev. Lett. **78**, 927 (1997).

[31] A. A. Abrikosov and L. P. Gor'kov, Zh. Eksp. Teor. Fiz. **39**, 1781 (1960) [Sov. Phys. JETP **12**, 1243 (1961)].

[32] K. Maki and P. Fulde, Phys. Rev. **140**, A1586 (1965).

[33] A. T. Larkin, Zh. Eksp. Teor. Fiz. **48**, 232 (1965) [Sov. Phys. JETP **21**, 153 (1965)].

[34] R. Meservey and P. M. Tedrow, Phys. Rep. **238**, 173 (1994).

[35] V. Yu. Butko, P. W. Adams, and I. L. Aleiner, Phys. Rev. Lett. **82**, 4284 (1999).

[36] D. C. Raplh, C. T. Black, and M. Tinkham, Phys. Rev. Lett. **78**, 4087 (1997).

[37] F. Braun, J. vonDelft, D. C. Ralph, and M. Tinkham, Phys. Rev. Lett. **79**, 921 (1997).

[38] A. V. Lopatin and V. M. Vinokur, Phys. Rev. Lett. **90**, 047003 (2003).

[39] W. A. Little, Phys. Rev. **156**, 398 (1967).

[40] D. Y. Vodolazov, F. M. Peeters, L. Piraux, S. Matefi-Tempfli, and S. Michotte, Phys. Rev. Lett. **91**, 157001 (2003).

[41] M. Tinkham, J. U. Free, C. N. Lau, and N. Markovic, Phys. Rev. B **68**, 134515 (2003).

Reproduced with permission of the copyright owner. Further reproduction prohibited without permission.

[42] A. A. Abrikosov and L. P. Gor'kov, Zh. Eksp. Teor. Fiz. **42**, 1088 (1962) [Sov. Phys. JETP **15**, 752 (1962)].

[43] L. F. Mattheiss, Phys. Rev. B **1**, 373 (1970).

Reproduced with permission of the copyright owner. Further reproduction prohibited without permission.

Chapter 5

Properties of Insulating Nanowires

The superconducting wires that were considered in Chapter 4 were shown to follow the predictions of the Langer-Ambegaokar-McCumber-Halperin (LAMH) theory of thermally activated phase slips very well, with resistance that went to zero as temperature went to zero. Also, the differential resistance showed a minimum at zero-bias and a slight increase at higher bias, before jumping to the high resistance state, which also was found to agree with the LAMH theory. These two characteristics of superconducting samples are in sharp contrast to the behavior observed for insulating samples. Instead of going to zero with decreasing temperature, wires in the insulating regime show increasing resistance. In addition, a zero-bias maximum is observed in the differential resistance at zero-bias. We will examine these two traits of insulating wires in this chapter and provide an explanation for their appearance.

The results and text of this chapter were submitted for publication under the title "Coulomb Blockade in the Insulating Regime of Short Superconducting Nanowires" by Anthony T. Bollinger, Andrey Rogachev, and Alexey Bezryadin and are repeated here. For future reference, the sample labels used in the paper, A, B, C, D, E, F, G, and H, correspond to samples 070404c, 070404b, RD1, 022402g, 022402h, 070404a, AR1, and 041702d, respectively.

Reproduced with permission of the copyright owner. Further reproduction prohibited without permission.

5.1 Introduction

One of the fundamental unresolved problems concerning one-dimensional (1D) superconductivity is understanding the mechanism that drives the observed superconductor-insulator transition (SIT) [1-3]. Under certain conditions, usually associated with some critical resistance per square [1], critical resistance [2], or critical diameter [4], a wire can loose its superconductivity and acquire some characteristics of insulating behavior, such as increased resistance with cooling and a zero-bias resistance peak [2, 3].

Theoretically, a number of models have been suggested which capture certain features of the SIT. Some models rely on the "fermionic" mechanism, in which the Coulomb interaction [5, 6] or weak localization [7] drives the critical temperature, T_C, of the superconductor to zero, thus destroying superconductivity completely. In other "bosonic" models the order parameter and the critical temperature remain above zero at the SIT critical point but the coherence and thus the ability of the sample to carry a supercurrent is destroyed by quantum fluctuations known as quantum phase slips (QPS) [8-14]. In many models, the interaction of the superconductor with the quantum environment is of crucial importance. Experimentally, the mechanism of the SIT and its relation to QPS is still under debate [1-4].

Here we report systematic measurements on a large ensemble of nanowires in the vicinity of the SIT. Our main focus in this Letter is on wires in the insulating phase, which are the least understood. We find that the behavior of these wires follows closely the predictions of theories considering coherent transport in mesoscopic normal metal conductors in which the transport properties are determined by a weak Coulomb blockade

Reproduced with permission of the copyright owner. Further reproduction prohibited without permission.

[15, 16]. In essence, this is the same behavior as the weak Coulomb blockade found in tunnel junctions and explained by Pekola *et al.* [17]. Here we also demonstrate that the wires in the superconducting phase, even those that are close to the SIT, obey the predictions of the theory of thermally activated phase slips (TAPS), due to Langer, Ambegaokar, McCumber, and Halperin (LAMH) [18]. This suggests that a true superconducting regime, i.e. zero resistance at zero temperature, is realized in this group of wires. The apparent SIT is abrupt, in the sense that each wire studied either exhibits a perfect LAMH behavior or follows the predictions for the weak Coulomb blockade in coherent normal metal wires.

5.2 Recap of fabrication and measurement

The nanowires used in this study were 45-140 nm in length and fabricated by molecular templating [2]. Fluorinated single-walled carbon nanotubes (FSWNTs), which are known to be insulating [19], were deposited from an isopropanol solution onto the surface of a Si/SiO2/SiN substrate that had a trench cut into it by electron beam lithography and reactive ion etching. The substrate with suspended nanotubes was then DC sputtered with amorphous [20] $Mo_{0.79}Ge_{0.21}$ in a high vacuum ($\leq 3\times10^{-7}$ Torr) chamber equipped with a cold trap. Many wires that connect the thin films, simultaneously grown on both sides of the trench, were formed in this process. Using a scanning electron microscope we examined all of the wires on the substrate and picked the best one for measurements. Our choice was influenced by such factors as apparent homogeneity and straightness of the wire, desired dimensions, and good connection of the wire to the films. The last condition is indicated by bright spots at the ends of the

Reproduced with permission of the copyright owner. Further reproduction prohibited without permission.

wires that show that the wire begins at the top of the trench and does not dip down into it (Fig. 5.1(a)). Using standard photolithography the chosen wire was masked off and contact pads were defined in the thin films on either side of the trench. Unprotected wires and portions of the films were subsequently etched away with 3% H_2O_2.

Transport measurements were performed in ^{4}He and ^{3}He cryostats, and one sample (sample F) was tested in a top-loading dilution refrigerator. Each system had appropriate π and microwave filtering placed at room- and cold-temperature stages, respectively. By current biasing the sample at 1 nA through a large (~ 1 MΩ) resistor, zero-bias resistance vs. temperature, $R(T)$, was obtained from the slope of the linear part of voltage vs. current, $V(I)$, curves. The differential conductance vs. bias voltage, $dI(V)/dV$, was measured using an AC excitation on top of a DC offset both generated by an ultra low distortion function generator (SRS-DS360).

5.3 R(T) behavior of insulating nanowires

Resistance vs. temperature data for representative insulating and superconducting samples are shown in Figs. 5.1(b) and (c), respectively. The transition occurring in all samples at higher temperature is not that of the wires but of the film electrodes that are measured in series with the wires. Below this transition the electrodes are superconducting and we are probing the wires themselves. All of the wires were fabricated with the same technique but the thickness of MoGe that was sputtered was continuously reduced from sample to sample in the interval 8.5-4.0 nm. This can be seen in Figs. 5.1(b) and (c) by noticing that the critical temperature of the thin film electrodes continuously decreases as we go from the thickest superconducting samples to the

Reproduced with permission of the copyright owner. Further reproduction prohibited without permission.

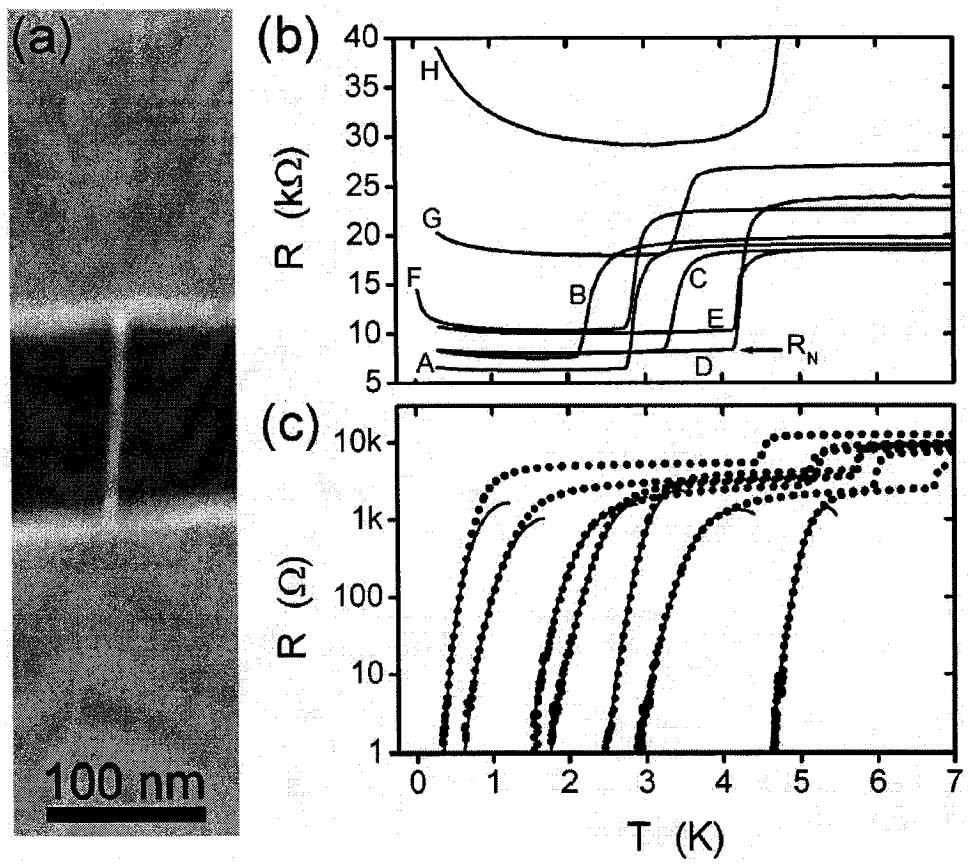

Figure 5.1: (a) SEM picture of a nanowire ~8 nm wide (light) fabricated across a trench (dark). The scale bar is 100 nm. Resistance vs. temperature curves for (b) insulating (4.0-6.0 nm MoGe thickness) and (c) superconducting (6.0-8.5 nm MoGe thickness) wires. In (c), data are shown as symbols and fits to the LAMH theory are shown as lines.

thinnest insulating ones. We find that the resistive transitions of the superconducting wires are well described by the LAMH theory of TAPS (Fig. 5.1(c)). Details of the fitting procedure are given in Ref. [21] (and Chapter 4). The only modification that was made here was replacing the temperature dependence for the thermodynamic critical fueld from the form valid near T_C, $H_C(T) \propto 1-T/T_C$, to the form that is appropriate for low temperatures, $H_C(T) \propto 1-(T/T_C)^2$, in the LAMH free energy barrier for phase slips, $\Delta F(T) = \left(8\sqrt{2}/3\right)\left(H_C^2(T)/8\pi\right)A\xi(T)$, where A is the cross-sectional area of the wire

Reproduced with permission of the copyright owner. Further reproduction prohibited without permission.

and $\xi(T)$ is the Ginzburg-Landau coherence length [22]. This modification was only applied to fit the data for the two samples with the lowest T_C. Such good agreement with the LAMH theory confirms that the observed superconducting regime is a true superconducting phase with zero resistance at zero temperature. Also, it confirms the homogeneity of our samples, since inhomogeneities or discontinuities along the length of the wires would lead to phase slip centers with multiple resistive transitions and critical currents (all of our samples showed one critical current step).

The $R(T)$ curves of insulating wires obviously do not display a behavior consistent with TAPS. Rather they show an upturn at the lowest temperatures, with R increasing as T decreases. No reentrant downturn was ever observed, even for sample F, which was measured down to 10 mK. The main goal of this work is to elucidate the cause of this upturn as it will help to better understand the SIT in 1D superconducting wires and possibly lead to insight into the mechanism behind it.

As discussed in the introduction, one proposed explanation for the SIT is that it is due to quantum phase slips. There are actually two ideas centered around QPS. The first is that the SIT is not a true quantum phase transition but rather a crossover from a state in which the QPS rate is too low to be detected to a state in which the QPS rate is so high that it drives the wire normal [4, 10]. In this approach the insulating behavior emerges because the electronic states in the quasi-1D normal wires are localized. Since the barrier for quantum tunneling is the lowest in the thinnest wires ($\Delta F \propto A$), QPS occur more readily and these wires appear insulating. However, our wires do not display any signs of such a crossover. None of the superconducting samples show signs of greatly broadened resistive transitions compared with the LAMH theory [4] or of resistance "tails" [8, 23,

Reproduced with permission of the copyright owner. Further reproduction prohibited without permission.

24], both of which are characteristic of the aforementioned crossover. On the contrary, the transition from the LAMH to insulating behavior is abrupt. Thus we conclude that a quantum phase transition does occur in short nanowires. We speculate that this quantum phase transition takes place due to coupling of QPS to their electromagnetic environment [9, 12]. The prediction for insulating wires of finite length [12] is that, as $T \to 0$, R saturates at some finite value close to the wire's normal state resistance, R_N (shown in Fig. 5.1(b) for sample D). This is the behavior that we observe. Although the $R(T)$ curves show greater resistance than R_N at the lowest temperatures (Fig. 5.1(b)), we attribute this phenomenon to the weak Coulomb blockade as discussed below.

To understand the increase in resistance for insulating samples we compare our data with the predictions of theories that consider coherent transport in disordered conductors that include the effects of Coulomb blockade, which should be important for our mesoscopic wires. Weak Coulomb blockade was first observed and explained in tunnel junctions [17]. Later it was shown by Nazarov that Coulomb blockade can survive in homogeneous normal wires even if their resistance is much lower than the quantum resistance [15]. In other words, although a wire may be homogeneous and continuous, i.e. no breaks exist in the wire that serves as tunnel barriers, the Coulomb blockade can be present. Golubev and Zaikin (GZ) [16] confirmed this prediction by an effective action technique and extended the work to include a derivation of the $I(V)$ behavior, thus providing a clear means for comparison with experimental results.

The weak Coulomb blockade occurs at high temperatures ($k_B T > E_C$) and the zero-bias conductance, $G(T) \equiv 1/R(T)$, is given in the GZ theory as

Reproduced with permission of the copyright owner. Further reproduction prohibited without permission.

$$\frac{G(T)}{G_0} \simeq 1-\beta\left[\frac{E_C}{3k_BT}-\left(\frac{3\zeta(3)}{2\pi^4}g+\frac{1}{15}\right)\left(\frac{E_C}{k_BT}\right)^2\right] \tag{5.1}$$

where $\beta = 1/3$ for diffusive wires, which is the case for our samples ($\beta = 1$ for tunnel junctions), $\zeta(3) \simeq 1.202$, $g = 4G_0R_Q$, G_0 is the conductance in the absence of Coulomb effects, $R_Q = h/4e^2$, and E_C is the charging energy. Note that apart from the second

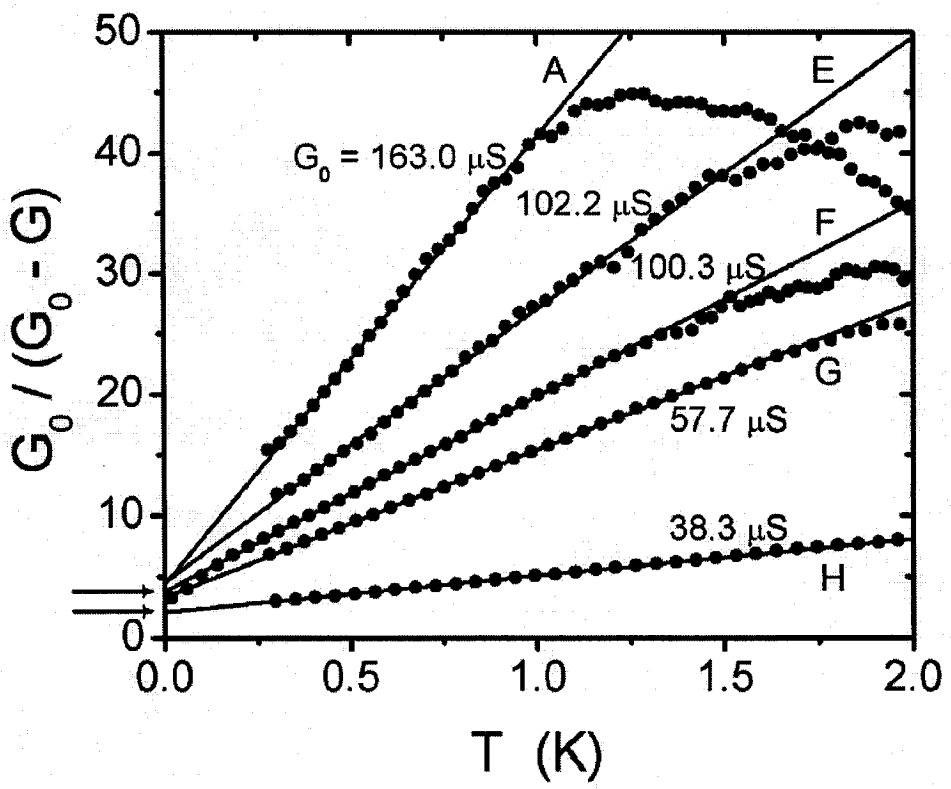

Figure 5.2: Normalized conductance change vs. temperature for samples A, E, F, G, and H. Data are shown as symbols and fits to GZ theory (Eq. 5.2) are shown as lines. Values of the fitting parameter G_0 are indicated and the range of theoretical predictions for the $T = 0$ intercepts is shown along the vertical axis by arrows. For these samples, G_0^{-1} = 6.14, 9.78, 9.97, 17.33, and 26.10 kΩ and R_N = 6.43, 10.33, 10.50, 18.05, and 32.46 kΩ, respectively.

Reproduced with permission of the copyright owner. Further reproduction prohibited without permission.

order term in E_C/k_BT this is the same result as obtained from the orthodox theory of tunneling for tunnel junctions [17]. By appropriate expansion in either E_C or $1/T$, this equation can be rewritten as

$$\frac{G_0}{G_0 - G(T)} = \frac{3k_BT}{\beta E_C} + \frac{9}{\beta}\left(\frac{3\zeta(3)}{2\pi^4}g + \frac{1}{15}\right) \tag{5.2}$$

In Fig. 5.2 we show the $R(T)$ data for samples A, E, F, G, and H from Fig. 5.1(b) plotted according to Eq. 5.2. The $R(T)$ upturns are clearly described quite well by Eq. 5.2 as demonstrated by the linearity of the curves. Similar results were obtained for samples B, C, and D but were omitted from Fig. 5.2 for clarity. As indicated by Eq. 5.2, the slope of linear fits to the $G_0/(G_0 - G(T))$ vs. T data is determined by the charging energy of the wire and the $T = 0$ intercept is determined by G_0 (through g). The experimentally determined $T = 0$ intercepts are in very good agreement with those predicted in Eq. 5.2 with the reasonable value of $G_0 = R_N^{-1}$ (arrows in Fig. 5.2).

5.4 dI(V)/dV behavior of insulating nanowires

The agreement between our measurements and the GZ theory is also evident from $G(V) \equiv dI(V)/dV$ data. A thermally smeared conductance "dip" is observed in the $dI(V)/dV$ behavior of all the insulating wires (Fig. 5.3). The shape of the $dI(V)/dV$ curves can be obtained from the GZ theory, in which the $I(V)$ dependence is given as

$$I = VG_0 - \frac{e\beta k_BT}{\hbar}\mathrm{Im}\left[w\Psi\left(1+\frac{w}{2}\right) - iv\Psi\left(1+\frac{iv}{2}\right)\right] \tag{5.3}$$

Reproduced with permission of the copyright owner. Further reproduction prohibited without permission.

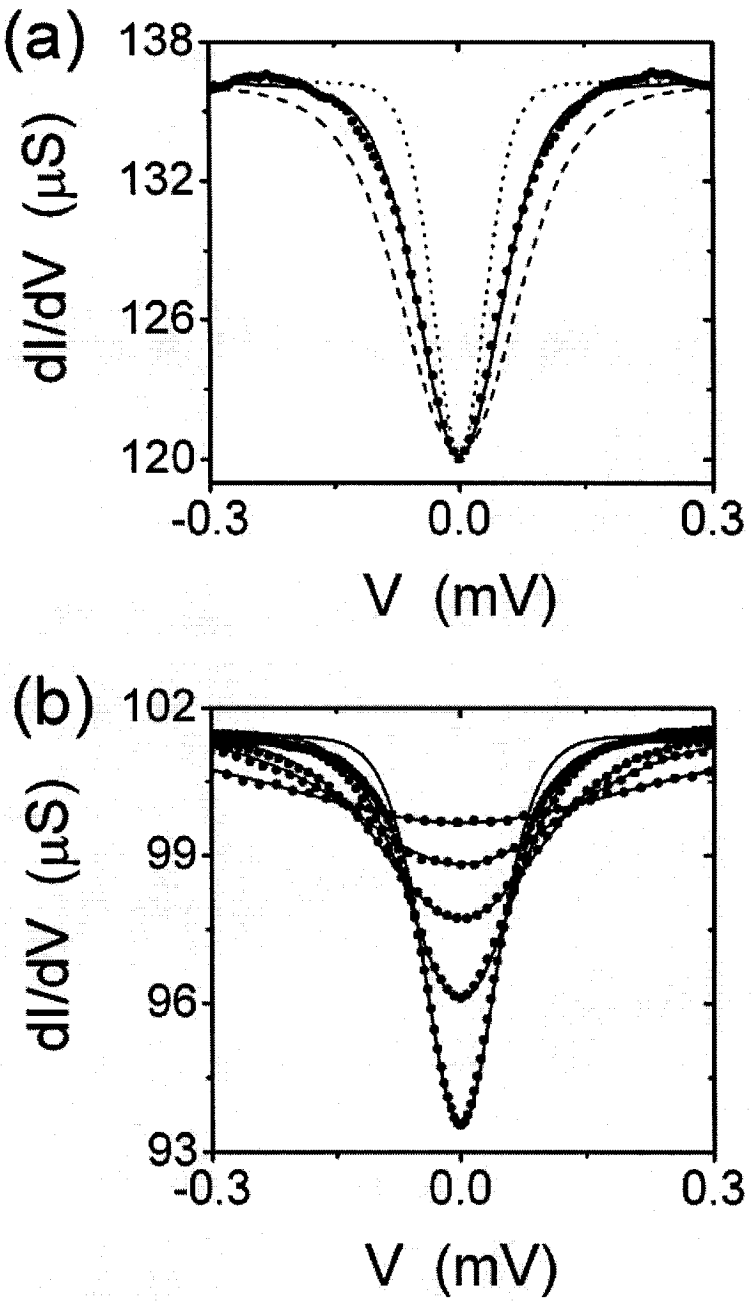

Figure 5.3: (a) Differential conductance vs. bias voltage data (symbols) for sample B at $T = 0.28\,\mathrm{K}$. Comparisons to the GZ theory are shown with $q_{eff} = e$ (dashed line), $q_{eff} = 1.29e$ (solid line), and $q_{eff} = 2e$ (dotted line). (b) Differential conductance vs. bias voltage curves at different temperatures for sample E with $T =$ 0:3 (deepest dip), 0.5, 0.75, 1.0, and 1.5 K (shallowest dip). Data are shown as symbols with fits to GZ theory shown as lines.

Reproduced with permission of the copyright owner. Further reproduction prohibited without permission.

where $w = u + iv$, $u = gE_C/\pi^2 k_B T$, $v = eV/\pi k_B T$, and $\Psi(x)$ is the digamma function. Again, to first order in $E_C/k_B T$ this is equivalent to the result for tunnel junctions [17]. By differentiating Eq. 5.3 and making a series expansion of $\Psi(x)$ we were able to perform fits to our data. One complication that does arise, however, is that the width of the experimentally observed dip was frequently found to be slightly narrower than what is predicted by the GZ theory (Fig. 5.3(a)). This cannot be explained by simply assuming an electron temperature higher than the lattice temperature, as this would result in the opposite case, i.e. even wider dips. One way to interpret these results is that the carriers have an effective charge, q_{eff}, that is larger than e. This is plausible since even though the wire is not superconducting, the thin film electrodes connected to it are. Therefore, a contribution to the conductance from double-electron transfer by Andreev reflection occurring at the ends of the wires should exist.

To take the effective charge into account we performed the fits to $dI(V)/dV$ data using the derivative of Eq. 5.3 with e replaced in all instances by q_{eff}, which we used as a fitting parameter along with G_0 and E_C. In Fig. 5.3(a) we plot the differential conductance vs. bias voltage for sample B at $T = 0.28\,\mathrm{K}$ compared to the GZ theory using different values of q_{eff}. Clearly, the original theory with $q_{eff} = e$ (dashed line) predicts a wider dip than what is observed, whereas $q_{eff} = 2e$ (dotted line) predicts a dip that is narrower. The best fit is found for $q_{eff} = 1.29e$ (solid line). We show the dip at various temperatures for a representative wire, sample E, as well as the fitting curves in

Reproduced with permission of the copyright owner. Further reproduction prohibited without permission.

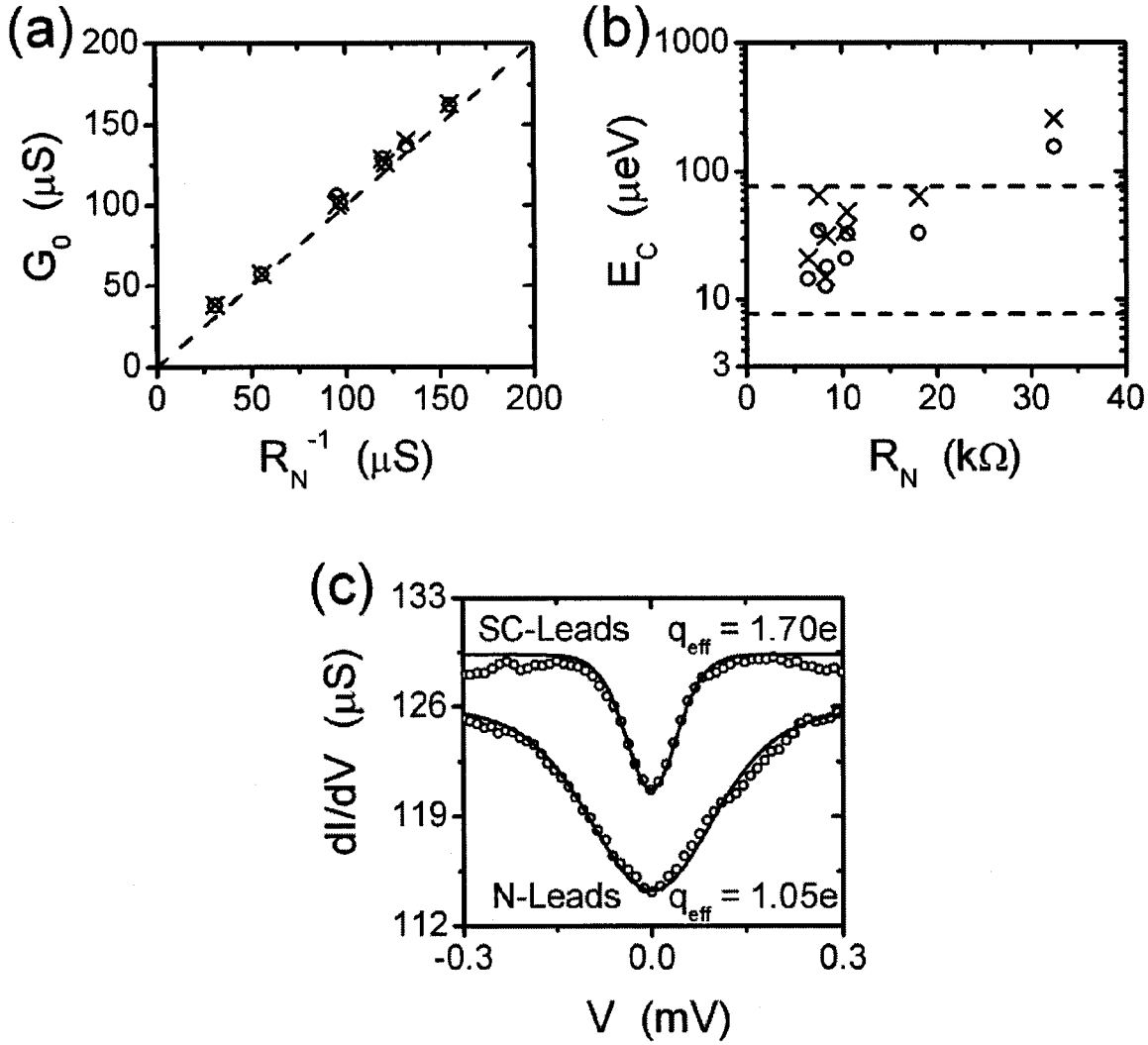

Figure 5.4: (a) Values of G_0 extracted from fits to GZ theory vs. inverse normal state resistance. Symbols are G_0 from temperature dependent (×) and voltage dependent (○) data. Dashed line is $G_0 = R_N^{-1}$. (b) Charging energy extracted from fits to GZ theory vs. normal state resistance. Symbols are E_C from temperature dependent (×) and voltage dependent (○) data. Dashed lines indicate the range of E_C determined independently from calculations of electrode geometry. (c) Differential conductance vs. bias voltage for sample D at two different magnetic fields. At zero field the leads are superconducting (SC-Leads) and $q_{eff} = 1.70e$ whereas at high field ($B = 9$ T) the leads are driven normal (N-Leads) and q_{eff} drops to $1.05e$. Solid lines are fits to GZ theory.

Reproduced with permission of the copyright owner. Further reproduction prohibited without permission.

Fig. 5.3(b). The model predicts the zero-bias conductance suppression for this sample rather well, with a similar fit quality found for the other samples.

The values obtained from these fits for G_0 and E_C for each sample are consistent with those found from fits to the $G_0/(G_0 - G(T))$ vs. T data (Figs. 4(a) and (b)). Furthermore, it is clear from Fig. 5.4(a) that G_0 is nearly the same as R_N^{-1} for all samples, which is expected since the temperatures at which R_N is defined is relatively high compared to the position of the upturn and so the Coulomb blockade is suppressed. The charging energies shown in Fig. 5.4(b) are also close to their expected range of values $\sim 8-76\ \mu eV$, which was obtained from a calculation of the capacitance for our electrode structure. The values for the effective charge are also reasonable as we always find $q_{eff} < 2e$, which is to be expected if the extra charge is from Andreev reflection. Finally, when a perpendicular magnetic field was used to drive the electrodes normal, q_{eff} was found to decrease to $\sim e$, providing additional proof for the excess charge stemming from the superconducting electrodes (Fig. 5.4(c)).

5.5 Conclusions

In summary, we have measured the behavior of superconducting nanowires and find they exhibit one of two distinct behaviors. Nanowires on the superconducting side of the superconductor-insulator transition follow the LAMH theory of thermally activated phase slips even for samples close to the SIT. The temperature dependent and voltage dependent data of nanowires on the insulting side of the transition agree well with the predictions of the GZ theory of weak Coloumb blockade in coherent diffusive wires. The

Reproduced with permission of the copyright owner. Further reproduction prohibited without permission.

parameters, G_0 and E_C, determined from theoretical fits to both temperature dependent and voltage dependent data are consistent with each other and are in good agreement with expected values. Thus we conclude that the transport mechanism in the insulating phase of the SIT can be understood in the same way as the diffusive quantum transport of single electrons in zero-dimensional mesoscopic conductors [15, 16, 25].

We thank R. Dinsmore for providing assistance with sample fabrication.

5.6 References

[1] F. Sharifi, A. V. Herzog, and R. C. Dynes, Phys. Rev. Lett. **71**, 428 (1993); P. Xiong, A. V. Herzog, and R. C. Dynes, Phys. Rev. Lett. **78**, 927 (1997).

[2] A. Bezryadin, C. N. Lau, and M. Tinkham, Nature **404**, 971 (1999).

[3] A. T. Bollinger, A. Rogachev, M. Remeika, and A. Bezryadin, Phys. Rev. B **69**, 180503(R) (2004).

[4] C. N. Lau, N. Markovic, M. Bockrath, A. Bezryadin, and M. Tinkham, Phys. Rev. Lett. **87**, 217003 (2001).

[5] Y. Oreg and A.M. Finkel'stein, Phys. Rev. Lett. **83**, 191 (1999).

[6] H. Ebisawa, H. Fukuyama, and S. Maekawa, J. Phys. Soc. Jpn. **55**, 4408 (1986).

[7] Y. -J. Kim and K. J. Chang, cond-mat/9706032.

[8] N. Giordano, Phys. Rev. Lett. **61**, 2137 (1988).

[9] A. D. Zaikin, D. S. Golubev, A. van Otterlo, G. T. Zimányi, Phys. Rev. Lett. **78**, 1552 (1997).

[10] D. S. Golubev and A. D. Zaikin, Phys. Rev. B **64**, 014504 (2001).

[11] Y. Oreg and E. Demler, cond-mat/0106645.

Reproduced with permission of the copyright owner. Further reproduction prohibited without permission.

[12] H. P. Büchler, V. B. Geshkenbein, and G. Blatter, Phys. Rev. Lett. **92**, 067007 (2004).

[13] S. Khlebnikov, Phys. Rev. Lett. **93**, 090403 (2004).

[14] S. Sachdev, P. Werner, and M. Troyer, Phys. Rev. Lett. **92**, 237003 (2004).

[15] Y. V. Nazarov, Phys. Rev. Lett. **82**, 1245 (1999).

[16] D. S. Golubev and A. D. Zaikin, Phys. Rev. Lett. **86**, 4887 (2001).

[17] J. P. Pekola, K. P. Hirvi, J. P. Kauppinen, and M. A. Paalanen, Phys. Rev. Lett. **73**, 2903 (1994); J.P. Kauppinen and J.P. Pekola, Phys. Rev. Lett. **77**, 3889 (1996).

[18] J. S. Langer and V. Ambegaokar, Phys. Rev. **164**, 498 (1967); D. E. McCumber and B. I. Halperin, Phys. Rev. B **1**, 1054, (1970).

[19] E. T. Mickelson, C. B. Huffman, A. G. Rinzler, R. E. Smalley, R. H. Hauge and J. L. Margrave, Chem. Phys. Lett. **296**, 188 (1998).

[20] J. M. Graybeal and M. R. Beasley, Phys. Rev. B **29**, 4167 (1984); J. M. Graybeal, Ph.D. thesis, Stanford University, 1985.

[21] A. Rogachev, A.T. Bollinger, and A. Bezryadin, Phys. Rev. Lett. **94**, 017004 (2005).

[22] M. Tinkham, *Introduction to Superconductivity*, 2nd ed. (McGraw-Hill, New York, 1996).

[23] M. Tian, J. Wang, J. S. Kurtz, Y. Liu, M. H. W. Chan, T. S. Mayer, and T. E. Mallouk, Phys. Rev. B **71**, 104521 (2005).

[24] M. Zgirski, K. -P. Riikonen, V. Touboltsev, and K. Arutyunov, Nano Lett. **5**, 1029 (2005).

Reproduced with permission of the copyright owner. Further reproduction prohibited without permission.

[25] D. Beckmann, H. B. Weber, and H. v. Löhneysen, Phys. Rev. B **70**, 033407 (2004).

Reproduced with permission of the copyright owner. Further reproduction prohibited without permission.

Chapter 6

The Superconductor-Insulator Transition

The results of the previous two chapters show that the MoGe nanowires we have studied fall into two classes – those that are superconducting and those that are insulating. The superconducting wires were shown to follow the predictions of the Langer-Ambegaokar-McCumber-Halperin (LAMH) theory [1, 2] of thermally activated phase slips (TAPS) very well. No evidence was found for additional resistance due to quantum phase slips (QPS). Insulating wires, on the other hand, agree with the theory [3] of weak Coulomb blockade for diffusive normal metal wires. Although we have explained the behavior of the two classes separately, we have yet to describe what governs the transition between the two classes.

We now turn our attention to the above results as a whole and try to understand what factors determine whether a wire displays superconducting or insulating behavior. Previous accounts of MoGe wires fabricated by molecular templating have reported conflicting results. Wires of length $L \approx 100$ nm were believed to show a quantum phase transition controlled by the normal state resistance, R_N, of the wire [4]. The superconductor-insulator transition (SIT) critical point was reported to be close to

Reproduced with permission of the copyright owner. Further reproduction prohibited without permission.

$R_N \approx R_Q = h/4e^2 = 6.5\,\mathrm{k\Omega}$. Wires with lower R_N were found to be superconducting while wires with larger R_N were insulating [4]. This is in contrast to results obtained on a larger set of longer wires, which had various lengths from $\sim 100\,\mathrm{nm}$ up to $\sim 1\,\mu\mathrm{m}$ [5]. For this set of wires a *crossover*, rather than a quantum phase transition, from superconducting to insulating behavior was reported that depended not on the normal state resistance but on the normal state resistance per unit length, R_N/L (or, equivalently, cross-sectional area, A). As R_N/L of the wires increased (A decreased), the wires became less superconducting, exhibiting broadened resistive transitions attributed to quantum phase slips (QPS), until superconductivity disappeared completely for the wires with the largest values of R_N/L ($R_N/L \sim 100\,\Omega/\mathrm{nm}$).

To resolve this apparent inconsistency we have fabricated three sets of fluorinated single walled carbon nanotube templated MoGe wires at different length scales, as described in chapter 3. The trench widths of the substrates used were the standard width of 100 nm used in Ref. [4], shorter trenches of width 50 nm, and wider trenches of width 450 nm. We will call the resulting wires corresponding to this three types of trenches as "standard length wires" (i.e. 86-187 nm), "short wires" (29-63 nm), and "long wires" (300-477 nm). By fabricating sets of standard length, short, and long wires on these substrates we were able to test the existence of a SIT in superconducting nanowires and also examine whether it is R_N or R_N/L that controls this transition. Parameters for all of these wires are given in Tables 6.1 and 6.2. The indicated lengths of the nanowires is measured from SEM images, between the centers of the white spots occurring at the ends of well-suspended nanowires. Note that as discussed in Chapter 4, the listed SEM

Reproduced with permission of the copyright owner. Further reproduction prohibited without permission.

		Sample	R_N (kΩ)	L (nm)	w (nm)	t (nm)	R_N/L (Ω/nm)	$R_{N,T}$ (kΩ)	T_{min} (K)
Short Wires	Superconducting	121204f	2.21	61	16.8	8.0	36.2	2.48	1.45
		101304a*	2.70	52	13.2	8.0	51.9	3.17	0.28
		041204c	2.78	63	22.1	7.0	44.1	3.12	1.53
		031405c	3.18	54	15.7	6.0	58.9	3.66	1.19
		121801c*	3.22	46	11.0	7.0	70.0	3.78	1.25
		121204i	3.64	43	13.3	7.0	84.7	4.33	0.29
		070404f*	4.76	38	13.8	5.0	125.3	6.04	0.19
	Insulating	070404d	6.34	56	11.4	5.0	113.2	7.43	1.50
		070404c	6.43	46	12.8	4.0	139.8	8.10	0.28
		070404b	7.54	45	11.3	4.0	167.6	9.77	0.29
		101304g	8.02	29	11.0	6.0	276.6	10.93	1.49
		070404a	10.50	49	10.2	4.0	214.3	13.02	0.02
Standard Length Wires	Superconducting	022402i	2.39	99	21.4	8.5	24.1	2.56	1.21
		022402j	3.14	127	18.7	8.5	24.7	3.31	1.41
		022402k	3.61	93	16.8	8.5	38.8	3.88	1.42
		031027m3 [†]	3.86	152	17.5	7.0	25.4	4.03	1.76
		031027m1 [†]	4.29	187	20.5	7.0	22.9	4.45	1.75
		013002d*	4.73	109	12.6	7.0	43.4	5.07	1.21
		070404k	5.46	177	15.5	6.5	30.8	5.70	0.29
		121801d*	5.61	116	11.6	7.0	48.4	5.96	1.47
		013002b*	6.09	125	14.2	7.0	48.7	6.46	1.32
		070404l*	6.92	180	19.2	7.0	38.4	7.21	1.34
		070404j*	7.35	141	13.4	6.5	52.1	7.76	0.29
	Insulating	RD1 [‡]	8.25	140	17.8	6.0	58.9	8.80	0.28
		022402g	8.35	105	10.6	5.5	79.5	9.01	0.30
		022402f	8.67	121	8.8	5.5	71.7	9.22	1.20
		022402h	10.33	140	10.8	5.5	73.8	10.93	0.30
		101503h	10.38	143	13.0	6.5	72.6	10.90	1.45
		AR1 [†]	18.05	162	11.4	5.0	111.4	19.03	0.28
		041702d	32.46	86	13.6	4.5	377.4	35.47	0.30

Table 6.1: Parameters for short and standard length samples. The normal state resistance, R_N, was determined from $R(T)$ curves. The length, L, and width, w, were measured from SEM micrographs. The sputtered MoGe thickness, t, was obtained from known sputtering rates. The normal resistance per unit length, R_N/L, was calculated from R_N and L. The proximity effect corrected total normal state resistance, $R_{N,T}$, was calculated using Eq. 6.1. T_{min} is the lowest measured temperature. * indicates a superconducting sample unable to be measured to low enough temperature to observe its full transition.

Reproduced with permission of the copyright owner. Further reproduction prohibited without permission.

		Sample	R_N (kΩ)	L (nm)	w (nm)	t (nm)	R_N/L (Ω/nm)	$R_{N,T}$ (kΩ)	T_{min} (K)
Long Wires	S	020904c	2.51	427	25.1	16.0	5.9	2.55	1.52
	M	020904b	2.79	435	23.1	16.0	6.4	2.83	0.30
	M	031027u1 [†]	3.15	474	26.0	15.0	6.6	3.20	2.42
	M	020904a	3.20	414	22.4	16.0	7.7	3.25	1.50
	S	031027v1 [†]	3.71	300	16.8	10.0	12.4	3.79	1.68
	S	020904d	7.23	461	24.4	9.0	15.7	7.33	1.51
	M	020904e	7.29	399	24.5	9.0	18.3	7.41	1.54
	S	020904f	7.53	396	19.1	9.0	19.0	7.66	1.97
	M	041204g	7.89	455	26.5	7.0	17.3	8.01	1.55
	M	031027w2* [†]	9.10	440	18.0	6.7	20.7	9.24	1.44
	S	041204h	9.40	431	19.9	7.0	21.8	9.55	1.51
	M	041204l	16.15	477	21.0	5.0	33.9	16.42	0.29
	I	041204k	22.41	433	14.8	5.0	51.8	22.82	0.02
	I	041204j	24.63	455	19.0	5.0	54.1	25.12	1.55

Table 6.2: Parameters for long samples. The normal state resistance, R_N, was determined from $R(T)$ curves. The length, L, and width, w, were measured from SEM micrographs. The sputtered MoGe thickness, t, was obtained from known sputtering rates. The normal resistance per unit length, R_N/L, was calculated from R_N and L. The proximity effect corrected total normal state resistance, $R_{N,T}$, was calculated using Eq. 6.1. T_{min} is the lowest measured temperature. For these wires, S indicates superconducting behavior, I insulating behavior, and M mixed behavior. * indicates a superconducting sample unable to be measured to low enough temperature to observe its full transition.

measured widths and thicknesses determined from sputtering rates are actually larger than the actual dimensions of the conducting cores of the wires due to oxidation. Our best estimate (explained in Chapter 4) is that oxidation has the effect of reducing the thickness by ~2.5 nm and the width by ~5 nm.

Reproduced with permission of the copyright owner. Further reproduction prohibited without permission.

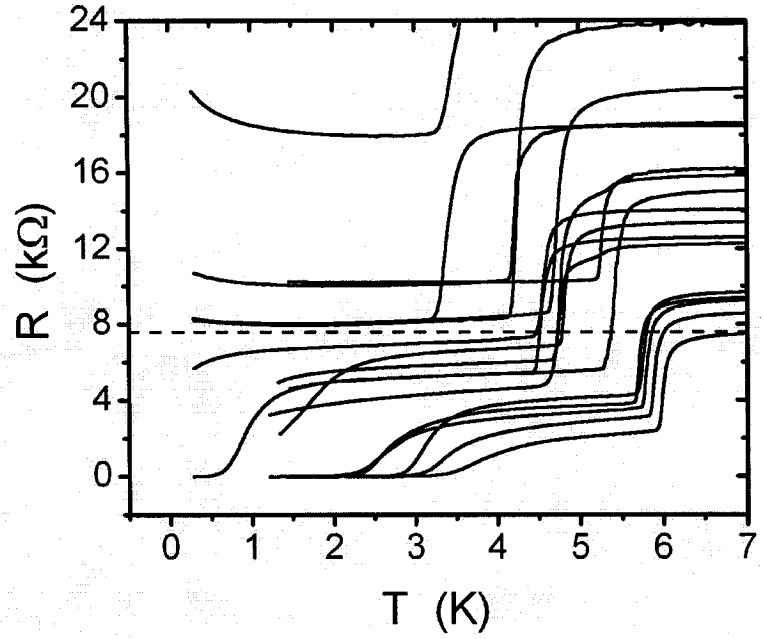

(a)

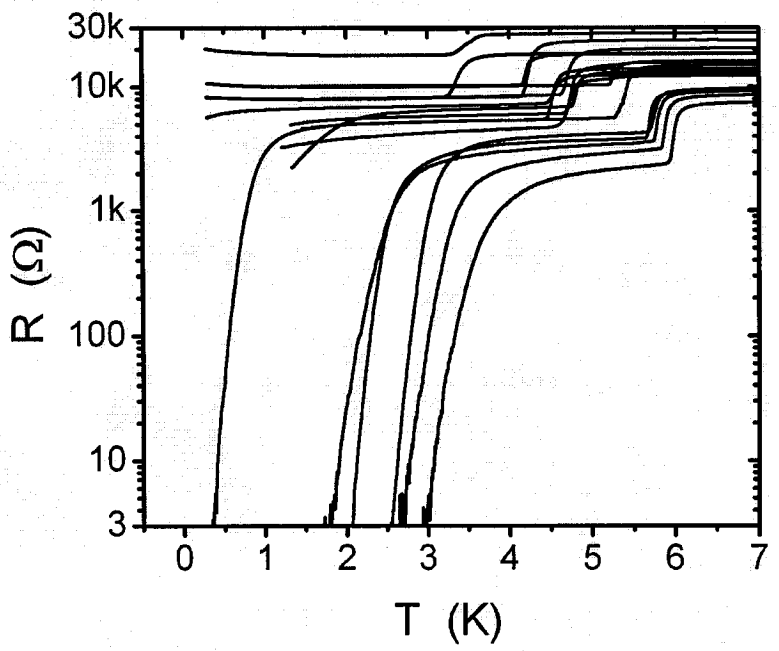

(b)

Figure 6.1: Resistance vs. temperature curves for standard length (~100 nm) wires in the (a) linear-linear and (b) log-linear representations. In (a), the dashed line separating superconducting and insulating wires is at 7.8 kΩ.

Reproduced with permission of the copyright owner. Further reproduction prohibited without permission.

6.1 R(T) curves

In Fig. 6.1 we show the resistance vs. temperature, $R(T)$, curves for standard length (~100 nm) wires. We find that the wires fall into two groups, superconducting and insulating, which confirms the results of Ref. [4] that an SIT occurs in superconducting nanowires at this length scale. The separatrix, shown as a dashed line in Fig. 6.1(a), between superconducting and insulating samples occurs at $R_N \approx 7.8 \pm 0.5\,\mathrm{k\Omega}$, which is slightly higher than that reported in Ref. [4]. Some of the superconducting samples in Fig. 6.1 were not measured to temperatures low enough that their resistance went to a value much lower than R_N. This lack of complete characterization was usually due to the samples "burning" from an accidental electrostatic discharge while being transferred from the ^{4}He to the ^{3}He system. We classify them as superconductors because: (i) they have decreasing resistance with decreasing temperature and (ii) they show zero-bias minimums at the lowest temperatures in differential resistance, $dV(I)/dI$, measurements, i.e. no zero-bias peak as in the case of insulating samples, and (iii) the curvature of the $\ln(R)$ vs. T curve is negative (it is always positive for the insulating wires). The lowest temperature, $T_{\min}$, down to which the samples were measured is shown in Tables 6.1 and 6.2.

The $R(T)$ curves for short wires are shown in Fig. 6.2. Again, two groups of samples are present – superconducting and insulating. For this family of curves, the separatrix occurs at $R_N \approx 5.5 \pm 0.8\,\mathrm{k\Omega}$ (Fig. 6.2(a)). This would seem to indicate that the SIT is not controlled by R_N, as this is different from the value obtained for standard

Reproduced with permission of the copyright owner. Further reproduction prohibited without permission.

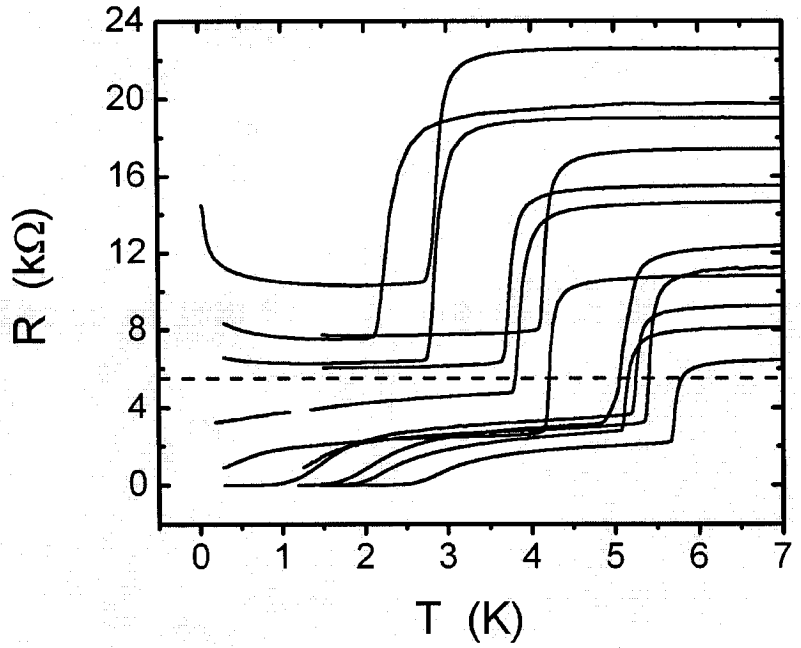

(a)

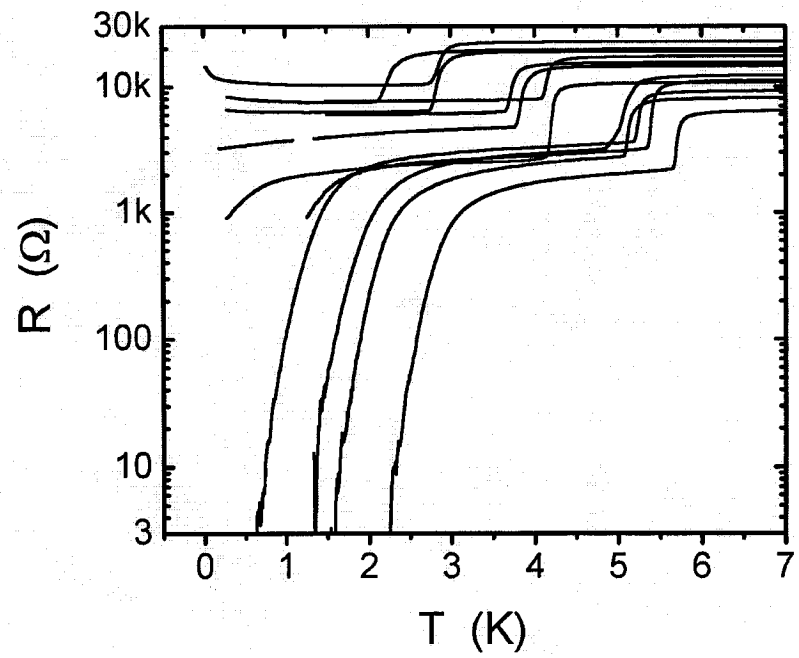

(b)

Figure 6.2: Resistance vs. temperature curves for short (~50 nm) wires in the (a) linear-linear and (b) log-linear representations. In (a), the dashed line separating superconducting and insulating wires is at 5.5 kΩ.

Reproduced with permission of the copyright owner. Further reproduction prohibited without permission.

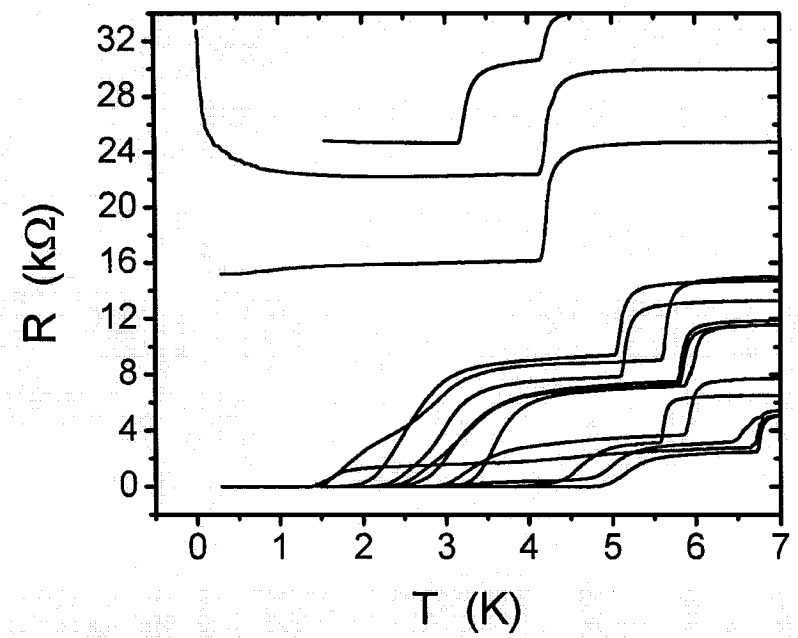

(a)

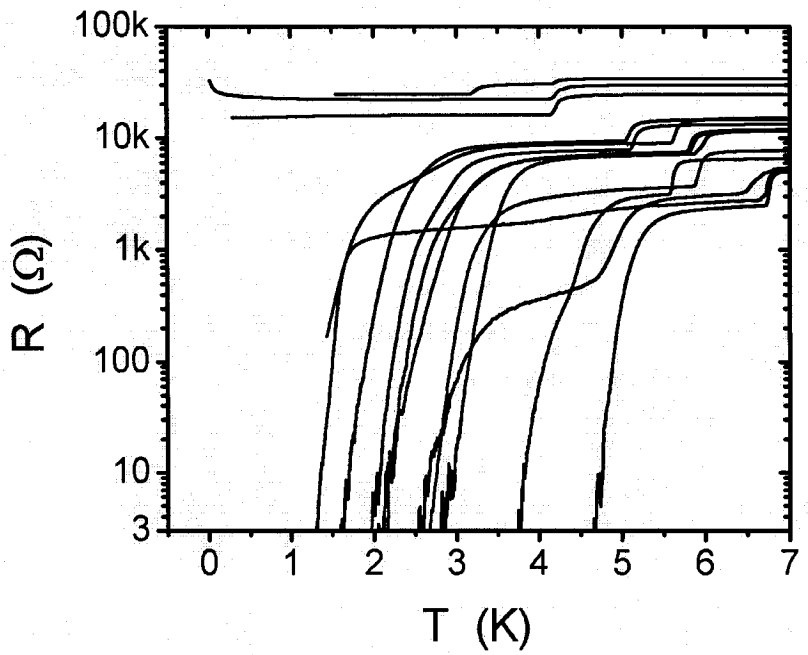

(b)

Figure 6.3: Resistance vs. temperature curves for long (~450 nm) wires in the (a) linear-linear and (b) log-linear representations.

Reproduced with permission of the copyright owner. Further reproduction prohibited without permission.

length wires. However, the error bars are rather large due to the fact that a large number of samples is needed for this method to give a precise answer. Also we note that lengths of the short wires are about half the lengths of the standard length samples. The critical R_N for the short samples is about 0.71 the critical R_N for standard length samples which means that R_N/L is not the control parameter for this SIT. This result is discussed further in the next section of this chapter.

In Fig. 6.3 we show the $R(T)$ curves for the long wires. Unlike the results obtained for short and standard length wires, the family of curves for the long wires does not display such a clear dichotomy of superconducting and insulating behavior. This is due to the fact that frequently the long wires act as though they are composed of a few independent sections. For example, sample 020904a shows two superconducting transitions (in addition to the transition from the thin film electrodes) and two critical currents at low temperature (Fig. 6.4) indicating it is composed of two superconducting sections. These double transitions are observed in other samples as well. Sample 041204l appears to be composed of one superconducting section and one insulating section as its $R(T)$ curve initially shows a superconductor-like decrease but then an insulator-like upturn at the lowest temperatures (Fig. 6.5). Such behavior is never observed in shorter homogeneous wires.

There are two possible explanations for this "mixed" behavior in long wires. The first is that the long wires are less homogeneous than the shorter wires. They could then contain a certain number of weak links that could lead to multiple superconducting transitions or to initially decreasing resistance and then saturation or even an increase in resistance at low temperatures, depending on the nature of the weak link. However, since

Reproduced with permission of the copyright owner. Further reproduction prohibited without permission.

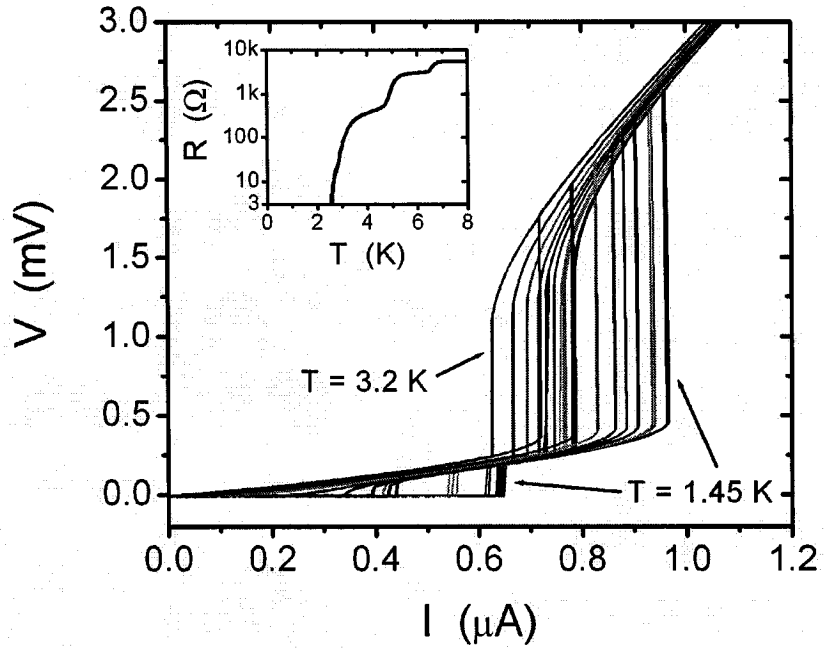

Figure 6.4: Voltage vs. current curves for sample 020904a. The temperatures at which these curves were taken are 1.45, 1.6, 1.8, 2.0, 2.2, 2.5, 2.8, and 3.2 K. (inset) Resistance vs. temperature curve for the same sample.

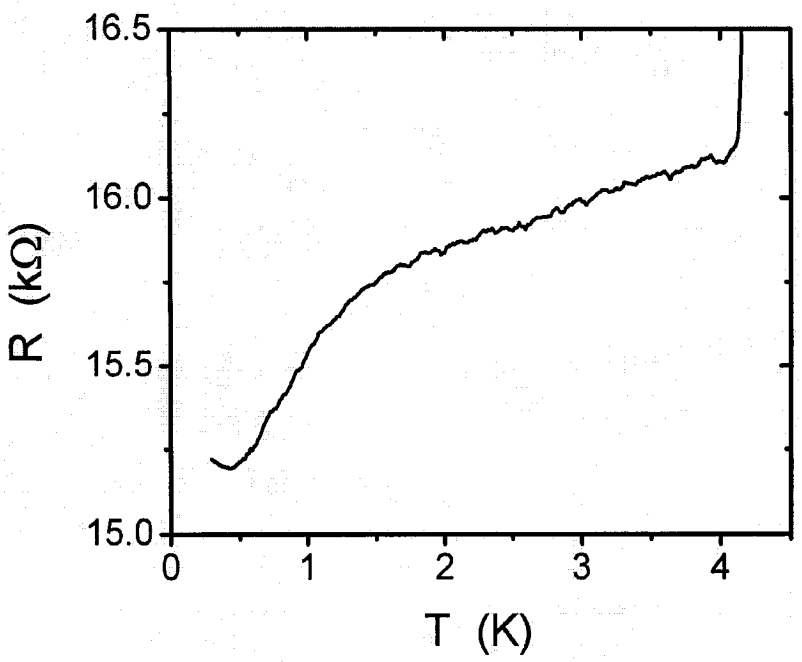

Figure 6.5: Resistance vs. temperature curve for sample 041204l.

Reproduced with permission of the copyright owner. Further reproduction prohibited without permission.

the long wires were fabricated with the same technique as the short and standard length wires it is not obvious why they should be less homogeneous. The thin film electrode transitions of the long wire samples occurs at nearly the same temperatures as the other samples (depending on film thickness) which indicates that the quality of the sputtered MoGe films are comparable to that of the other samples. Also, if the long wires were composed of many weak links their calculated resistivity should be larger than that of the other samples, but this is not the case. The second explanation for the observed behavior in long wires is that it is due to phase slip centers. It is well known that a long superconducting wire can show multiple critical temperatures and currents due to phase slip centers. Though the phase slip centers are usually attributed to some inhomogeneity, it is not a necessary condition [6]. The dissipative size of a phase slip center, $2\Lambda_Q$, was estimated to be about 200 nm for MoGe wires [7], which explains why we only see singular behavior in short and standard length wires but mixed behavior in the long wires. Whatever the exact mechanism for the mixed behavior in long wires it is plain that a clear SIT is not observed in these wires. Still, it is significant that the resistive "tails" expected from QPS are not observed in this family of wires.

6.2 Phase diagram

The above results show that a superconductor-insulator transition occurs in the short (~50 nm) and standard length (~100 nm) wires, although it is not apparent that the parameter controlling the transition is in exact agreement with either of the previously published results [4, 5]. This is most easily seen in Figs. 6.6 and 6.7 where we plot $R(T)$ and $R(T)/L$, respectively, for all short and standard length wires. In Fig. 6.6(b),

Reproduced with permission of the copyright owner. Further reproduction prohibited without permission.

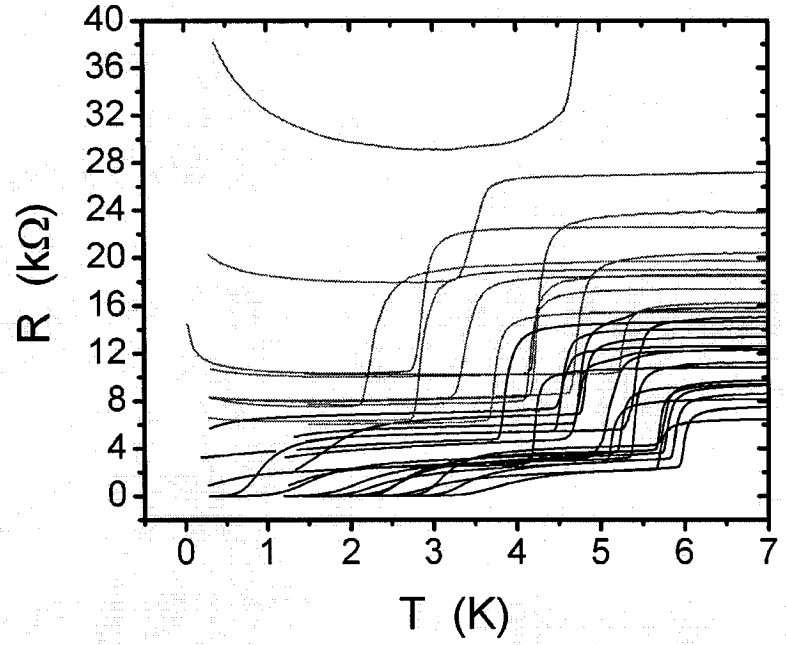

(a)

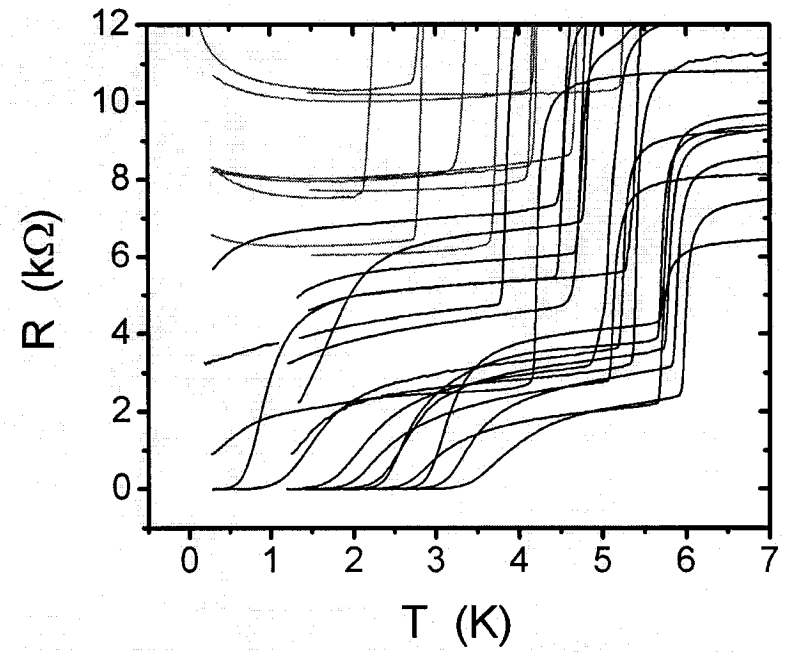

(b)

Figure 6.6: Resistance vs. temperature curves for short and standard length wires. Superconducting wires are shown as black lines and insulating wires as grey lines. (a) Full scale. (b) Zoomed in scale near the transition.

Reproduced with permission of the copyright owner. Further reproduction prohibited without permission.

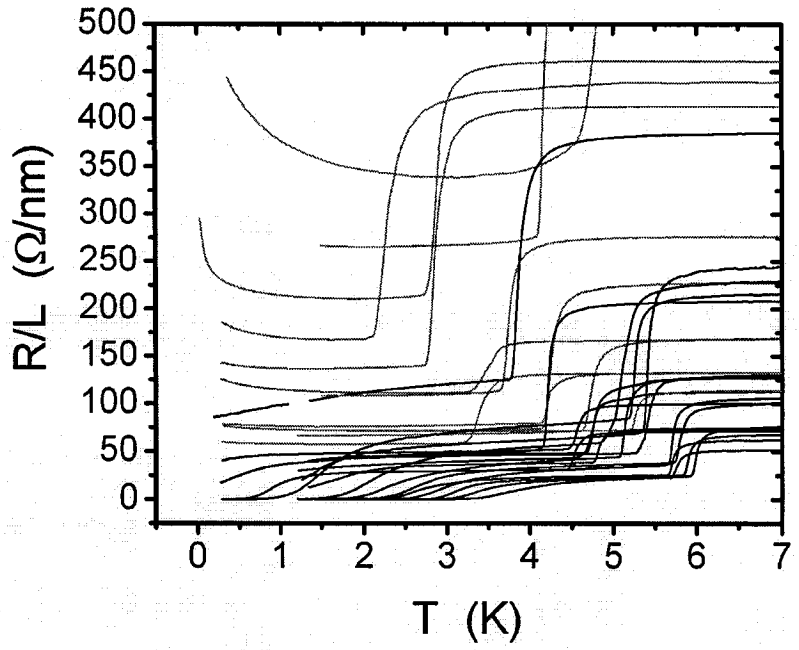

(a)

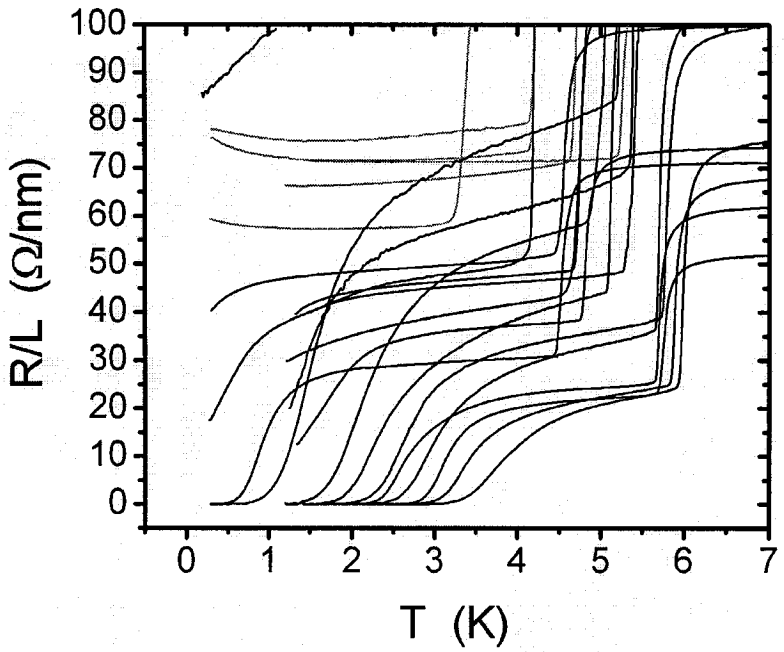

(b)

Figure 6.7: Resistance per unit length vs. temperature curves for short and standard length wires. Superconducting wires are shown as black lines and insulating wires as grey lines. (a) Full scale. (b) Zoomed in scale near the transition.

Reproduced with permission of the copyright owner. Further reproduction prohibited without permission.

we find that R_N *nearly* determines the transition from the superconducting to insulating state, in agreement with Ref. [4]. Also, the transition does occur near $R_N = R_Q$, again in agreement with Ref. [4], but there is a slight overlap between superconducting and insulating states. A clearer conclusion can be drawn from Fig. 6.7. Especially in Fig. 6.7(b) it is obvious that R_N/L does not control the SIT as many superconducting and insulating wires share the same R_N/L value and yet are in different phases.

Aside from the small overlap between the superconducting and insulating phases in Fig. 6.6, we conclude that it is the normal state resistance of the wire that controls the superconductor-insulator transition in homogeneous one-dimensional superconducting nanowires. To understand this overlap we show in Fig. 6.8(a) the phase diagram obtained from the measurements of all samples plotted in the R_N and L parameter space. Here, each (L, R_N) point represents a single wire. Superconducting samples are shown as filled (or black) circles, insulating wires as open (or white) circles, and the long wires that showed "mixed" behavior as grey-filled circles. Again, here it is clear that no single line that passes through the origin, which would represent a critical value of R_N/L, can be drawn that separates all superconducting and insulating wires. However, a horizontal line, indicating a critical value of R_N, can be drawn at $R_N = R_Q$ that nearly separates the superconducting and insulating wires of short and standard length ($L \leq 200$ nm). This analysis supports our previous discussion of Figs. 6.6 and 6.7.

When taking the normal state resistance for each sample from the $R(T)$ curves it is important to realize that we are not actually determining the *total* normal state resistance of the wire. Some short length on either side of the wire becomes

Reproduced with permission of the copyright owner. Further reproduction prohibited without permission.

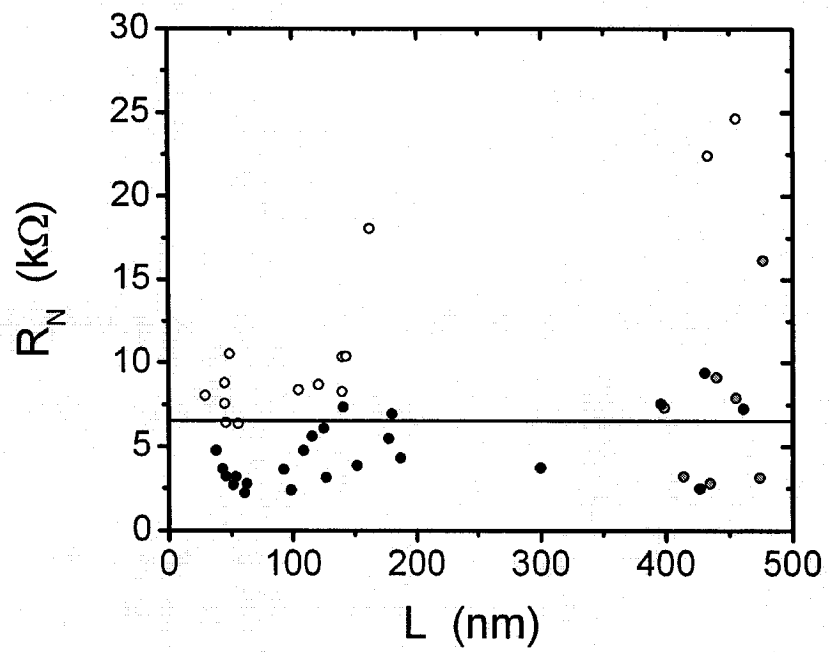

(a)

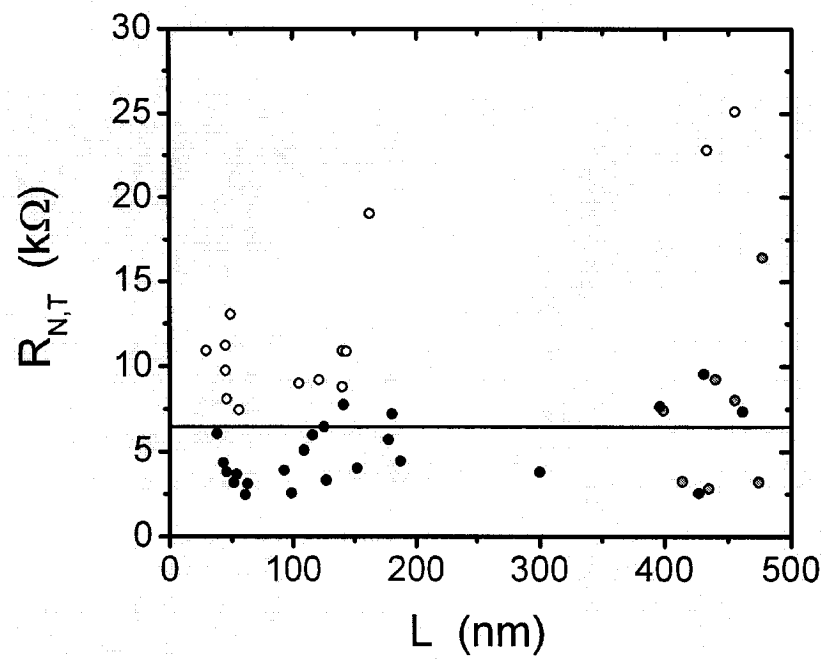

(b)

Figure 6.8: Phase diagram of all measured samples. Superconducting wires are shown as closed circles, insulating wires as open circles, and mixed wires as grey-filled circles. The solid line is $R_N = R_Q$. (a) R_N as originally determined from the $R(T)$ curves. (b) $R_{N,T}$ is *total* normal resistance corrected for proximity effect due to the film electrodes.

Reproduced with permission of the copyright owner. Further reproduction prohibited without permission.

superconducting due to the proximity effect from the thin film electrodes the wire is seamlessly connected to. The length that the Cooper pairs diffuse into the wire from one side is the normal metal coherence length, $\xi_N = \sqrt{\hbar D/2\pi k_B T}$ [6]. The length of wire contributing to the measurement of R_N is then $L - 2\xi_N$. Therefore, the total normal state resistance, corrected for proximity effect, is

$$R_{N,T} = R_N \frac{L}{L - 2\xi_N} \tag{6.1}$$

In Fig. 6.8(b) we plot the total normal state resistance vs. length for each sample. In this representation, the insulating state only occurs when $R_{N,T} > R_Q$. This type of behavior is typical for a Chakravarty-Schmid transition, which was observed experimentally in resistively shunted Josephson junctions and arrays [8, 9]. An interesting attempt was recently made to extend this type of analysis to a system involving mesoscopic grains, which showed that the total resistance of the shunts controls the transition [10]. Since this work was constructed for Josephson junctions, it seems to neglect the possibility of vanishing order parameter amplitude. Also, we do have two samples (070404j and 070404l) with normal resistance slightly higher than the quantum resistance, which show signatures of superconducting behavior. Note that these are two samples that we were unable to measure to low enough temperatures to characterize them fully. So, it is possible that at lower temperatures they would also show evidence of insulating behavior. Also, we cannot completely rule out the possibility that these two samples are simply inhomogeneous.

Reproduced with permission of the copyright owner. Further reproduction prohibited without permission.

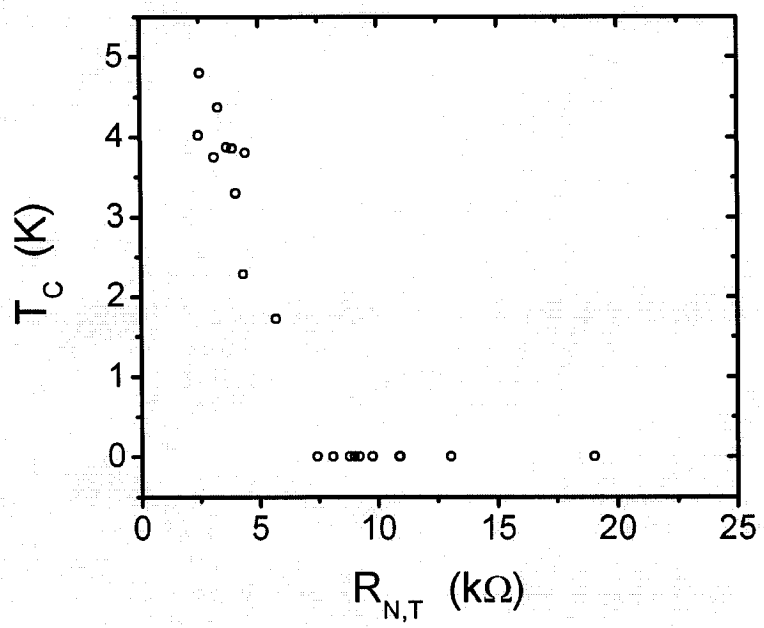

(a)

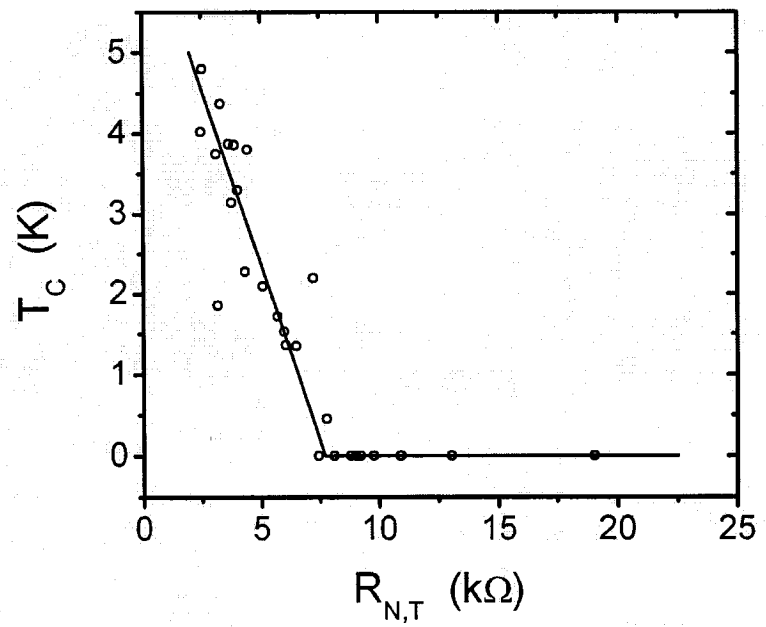

(b)

Figure 6.9: Critical temperature vs. total normal state resistance. (a) T_C is extracted from fits to the LAMH theory. (b) Estimated critical temperatures for those superconducting wires not able to be measured to low enough temperature to fit their full transition with the LAMH theory are combined with the data in (a). The line is a guide to the eye. Insulating wires in both (a) and (b) have been assigned $T_C = 0$.

Reproduced with permission of the copyright owner. Further reproduction prohibited without permission.

We finish this section by turning our attention to the disappearance of the superconducting state. In Fig. 6.9(a) we plot the critical temperature, T_C, of the short and standard length superconducting wires extracted from fits to the LAMH theory. Insulating wires are assigned a critical temperature of $T_C = 0$. With increasing total normal state resistance the critical temperature of the wires decreases, approaching zero near the SIT critical point. By including approximate critical temperatures from those superconducting samples that were not able to be measured to low enough temperatures to fit their resistive transitions with the LAMH theory this trend becomes even clearer (Fig. 6.9(b)). To obtain these estimated critical temperatures we use the fact that, on average, the resistances of the superconducting wires fit with the LAMH theory were found to be $0.82R_N$ at $T = T_C$. The suppression of T_C with increasing total normal state resistance and its approach to zero near the SIT critical point for wires in the superconducting states is in agreement with our conclusion that the order parameter is zero in the insulating phase. This is why the theory of weak Coulomb blockade for mesoscopic normal metals is successful in explaining the transport properties of our insulating wires.

6.3 Role of homogeneity

The results and text of this section were published under the title "Effect of Morphology on the Superconductor-Insulator Transition in One-Dimensional Nanowires" and are repeated here. Reprinted with permission from Anthony T. Bollinger, Andrey Rogachev, Mikas Remeika, and Alexey Bezryadin, Physical Review B **69**, 180503(R) (2004). Copyright 2004 by the American Physical Society.

Reproduced with permission of the copyright owner. Further reproduction prohibited without permission.

6.3.1 Introduction

Evidence for a superconductor-insulator quantum phase transition (SIT) in one-dimensional (1D) wires has been found in a number of experiments [4, 11] Yet, other studies have demonstrated a crossover, as opposed to a SIT, in thin wires where superconductivity disappears gradually, as diameter is reduced, presumably due to an increasing number of quantum phase slips (QPS) [5, 12, 13]. Thus the existence and possible origins of superconductor-insulator transitions in 1D remain important open problems. In particular, it is not known how the SIT depends on the morphology of nanowires.

In two-dimensional system, for example, the crucial role of morphology (i.e., granularity) on the SIT is well known [14-16]. For uniform films, as the film thickness is reduced, a reduction of the critical temperature is observed while the superconducting transition remains sharp. The SIT occurs when the square resistance of the film reaches a critical value close to the quantum resistance $R_Q = h/4e^2 = 6.5\,\mathrm{k\Omega}$ [17, 18]. In nonhomogeneous (granular) films, on the other hand, a reduction of the film thickness results in a *crossover* between superconducting and insulating regimes, with very broad resistive transitions in the thinnest superconducting samples [14, 19, 20]. Our goal here is to determine the morphological requirements for *1D nanowires* under which a SIT can occur.

In this Rapid Communication, we present a comparative study of homogeneous and inhomogeneous nanotube templated wires and find a qualitatively different behavior at low temperatures. Homogeneous samples (of length ~100 nm) show a SIT which occurs when the wire's normal resistance is close to R_Q, confirming previous results

Reproduced with permission of the copyright owner. Further reproduction prohibited without permission.

where different nanotubes were utilized as substrates [4]. Inhomogeneous wires, on the other hand, exhibit a mixed behavior displaying properties of superconductors and insulators at once. Such samples frequently show multiple steps in the resistive transitions but no resistive tails typical of QPS [5, 12, 13]. We propose a qualitative model which regards the inhomogeneous wire as a sequence of weak link constrictions (WLC's) connected in series. Each WLC has a certain dissipative size and corresponding normal resistance, depending on which the WLC can be either superconducting or insulating. Homogeneous (and short enough) wires do not show such mixed behavior because each wire acts as a single WLC.

6.3.2 Essential fabrication difference

The wires were fabricated using a molecular templating technique [4], in which a single-walled carbon nanotube was suspended over a ~100 nm wide trench etched into a multilayered Si/SiO2 /SiN substrate. Unlike previous studies [4, 5], here we use *fluorinated* single-wall nanotubes (FSWNT), which are known to be insulating [21]. The substrate with suspended nanotubes was then sputter-coated [22] in one of the two ways: (i) with amorphous [23] $Mo_{0.79}Ge_{0.21}$ or (ii) with a slightly thinner amorphous $Mo_{0.79}Ge_{0.21}$ film followed (in the same vacuum cycle) by a 2 nm Si film. Contact pads were defined using photolithography, followed by (i) wet etching in H_2O_2 for MoGe or (ii) reactive ion etching followed by wet H_2O_2 etching for Si-coated samples. While both processes produce samples with the same geometry (Fig. 6.10(a)) and similar dimensions (Table 6.3), these two fabrication methods result in different wire morphologies as revealed by transmission electron microscopy (TEM) imaging and confirmed by transport measurements (see below). The first process results in homogeneous nanowires (Fig.

Reproduced with permission of the copyright owner. Further reproduction prohibited without permission.

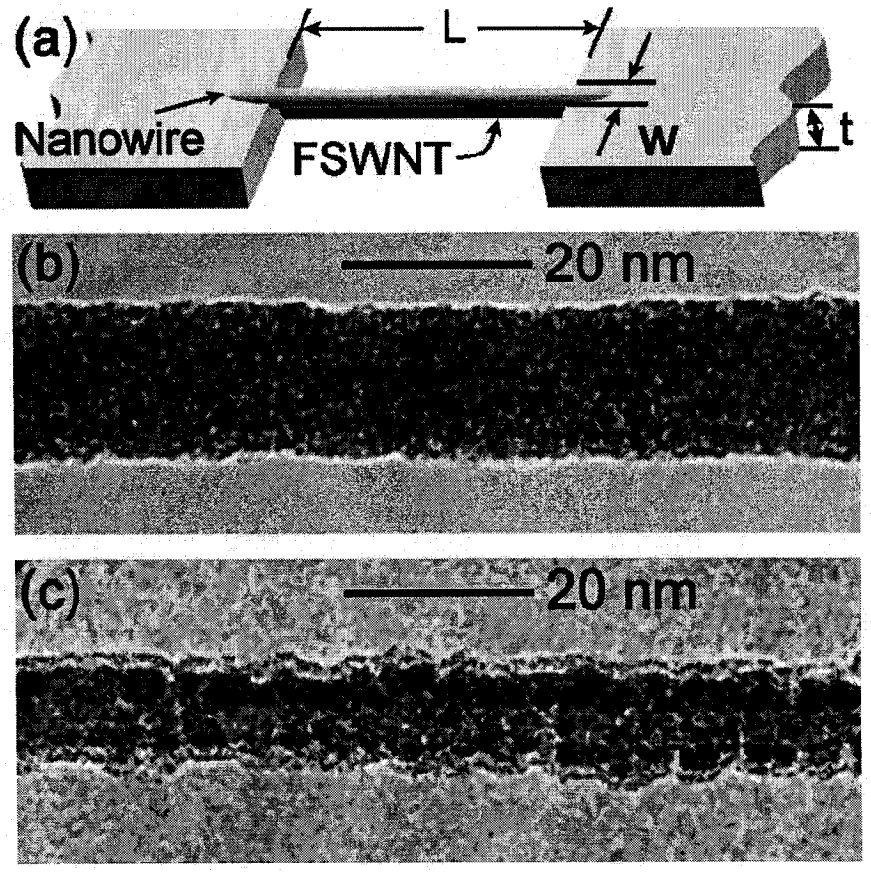

Figure 6.10: (a) Sample configuration. The sample consists of two coplanar films seamlessly connected by a thin wire. (b) A TEM micrograph of a typical uncoated wire formed on a nanotube template. The MoGe thickness is 8 nm. (c) A TEM micrograph of a Si-coated MoGe wire. Sputtered MoGe thickness is 4.5 nm and Si thickness is 2 nm.

6.10(b)), which we will refer to as ''bare'' wires. The second method yields inhomogeneous wires, which will be called ''Si-coated'' wires (Fig. 6.10(c)). Although these two fabrication methods give qualitatively different wires, the exact mechanism of this is not clear. The most probable explanation is that Si introduces some surface tension that leads to the creation of grains. On the other hand, if exposed to air, the outer layer of MoGe wires oxidizes unless coated by a protective film, in our case Si. To ensure that the conducting cores of bare wires have similar dimensions as the cores of the

Reproduced with permission of the copyright owner. Further reproduction prohibited without permission.

Label	Sample	R_N (kΩ)	L (nm)	w (nm)	t (nm)
A1	022402i	2.39	99	21.4	8.5
A2	022402j	3.14	127	18.7	8.5
A3	022402k	3.59	93	16.8	8.5
A4	031027m3	3.86	156	18.5	7.0
A5	031027m1	4.29	188	20.8	7.0
A6	013002d	4.73	109	12.6	7.0
A7	121801d	5.61	116	11.6	7.0
A8	013002b	6.09	125	14.2	7.0
A9	022402g	8.22	105	10.6	5.5
A10	022402f	8.67	121	8.8	5.5
A11	022402h	9.67	140	10.8	5.5
A12	041702d	32.46	86	13.6	7.5
B1	062603a	4.85	126	15.4	6.0
B2	012003d	8.30	121	14.9	4.5
B3	012003c	9.52	139	12.1	4.5
B4	012003f	15.26	121	11.4	3.5
B5	062603d	16.31	123	13.8	4.0
B6	012003f	19.30	145	15.9	4.0
B7	062603f	44.83	115	13.0	2.0

Table 6.3: Parameters of nanowires. The names in the column "Label" is what a sample was referred to as in this paper and the name in the column "Sample" is what they are called in this dissertation. Both are given for consistency between the paper and this dissertation. Samples A1-A12 are bare MoGe wires and B1-B7 are Si-coated wires. The normal resistance of nanowires (R_N) was determined from $R(T)$ curves, as indicated by an arrow for sample A1 in Fig. 6.12(a). Wire lengths (L) and widths (w) were measured with a SEM. Here t is the sputtered thickness of MoGe.

Si-coated wires, the bare wires must be made thicker to compensate for the expected surface oxidation. Since thicker wires are typically more homogeneous than the very thin ones, our bare wires exhibit a much higher degree of homogeneity.

6.3.3 Estimation of oxidized MoGe thickness

The oxidized layer thickness (in bare wires) can be estimated as follows (Fig. 6.11). For each sample, the wire length L divided by the normal state resistance R_N is

Reproduced with permission of the copyright owner. Further reproduction prohibited without permission.

plotted versus scanning electron microscopy (SEM) measured width w in Fig. 6.11(a). The bare wire data (circles) can be well approximated by a linear fit (dashed line), providing evidence for their homogeneous structure. The fitting parameters give an oxidized layer thickness ~2.3 nm (half of the fit's x-axis intercept value) and the resistivity for MoGe $\rho \sim 180\,\mu\Omega$-cm (obtained from the fit's slope and the wire's average thickness, $d_{ave} \approx 4.7$ nm, estimated under the assumption that the top 2.3 nm of the sputtered MoGe is oxidized), in agreement with published values [4, 23]. No reasonable linear fit could be obtained for the Si-coated wires (crosses), further indicating their inhomogeneous structure. In Fig. 6.11(b) we compare the T_C's of bare MoGe films

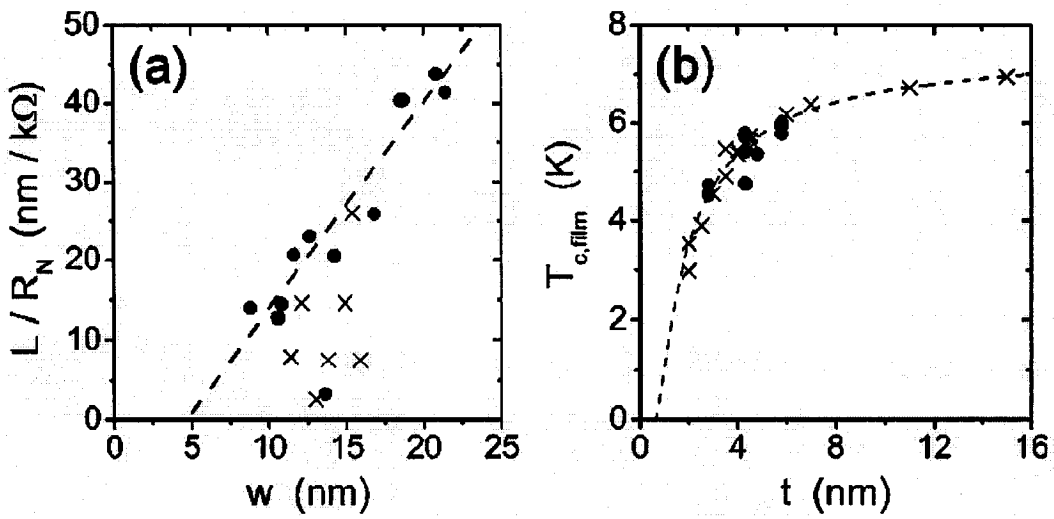

Figure 6.11: (a) L/R_N vs. w for bare (circles) and Si-coated (crosses) wire samples. The dashed line is a linear fit to the bare wire data, $L/R_N = (2.6\,\text{mS})(w - 4.6\,\text{nm})$. (b) Film T_C vs. t for bare (circles) and Si-coated (crosses) film samples. In order for the data to agree, the bare MoGe film data have been shifted from their actual position to the left by 2.7 nm, which accounts for the thickness of the oxidized surface layer. The dashed curve is a theoretical fit (Eq. 3 in Ref. [24]).

Reproduced with permission of the copyright owner. Further reproduction prohibited without permission.

and Si-coated MoGe films (circles and crosses, respectively) plotted versus their thicknesses. By shifting the data for bare films by 2.7 nm to the left the two families of data points overlap (Fig. 6.11 (b)). It is therefore concluded that the oxidized layer thickness is 2.7 nm, similar to the above estimate.

6.3.4 Recap of measurement

Voltage versus current measurements, $V(I)$, were performed by current biasing the sample through a large (~1 MΩ) resistor. Zero-bias resistance $R(T)$ was obtained from the slope of the linear part of the $V(I)$ curves as temperature was varied. Similar to Ref. [25], transport measurements were performed in ^{4}He or ^{3}He cryostats equipped with rf-filtered leads. The differential resistance vs. bias current, $dV(I)/dI$, was measured using an ac excitation on top of a dc current offset generated by a low-distortion function generator (SRS-DS360)

6.3.5 R(T) measurements

Zero-bias resistance versus temperature measurements are compared for homogeneous (Figs. 6.12(a) and (b)) and inhomogeneous (Figs. 6.12(c) and (d)) nanowires. First note that the rightmost superconducting transition observed on all samples is due to the electrodes (i.e., thin MoGe films connected to the ends of the wire). Below the temperature of this transition ($T_{C,film}$) only the wire contributes to the measured resistance. Therefore, in what follows we will only be interested in temperatures $T < T_{C,film}$. We first discuss the family of $R(T)$ curves for bare wire samples, presented in Fig. 6.12(a), which show a clear dichotomy. In the log-linear representation, samples A1–A8 all have negative curvature ($d^2 \log(R)/dT^2 < 0$) with

Reproduced with permission of the copyright owner. Further reproduction prohibited without permission.

more than half of these samples reaching immeasurably low resistances. Therefore, we refer to these samples as superconducting. Although samples A6, A7, and A8 do not reach such low resistances, their negative curvature as well as their decreasing resistance with decreasing temperature (Fig. 6.12(b) lead us to believe they too are superconducting. Due to their smaller widths we assume that their critical temperatures are suppressed [24]

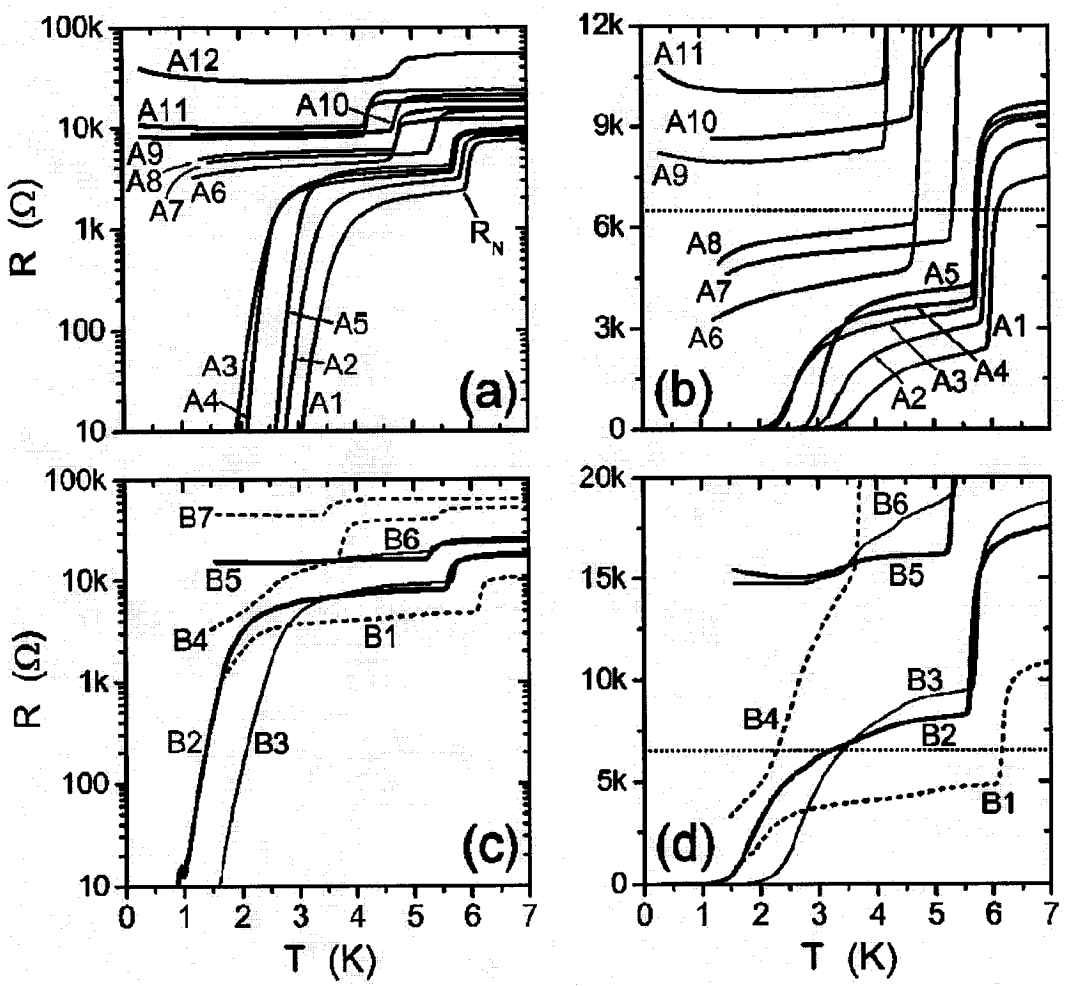

Figure 6.12: Resistance vs. temperature curves are shown for bare wires, which are homogeneous ((a) and (b)), and Si-coated wires, which are inhomogeneous ((c) and (d)). Figures (b) and (d) show the data on a linear scale for clarity. The horizontal dotted lines indicate the R_Q level at which the SIT occurs in homogeneous samples.

Reproduced with permission of the copyright owner. Further reproduction prohibited without permission.

such that they do not go through their full superconducting transition within the temperature range studied. Samples A9–A12 show only the transition of the film electrodes. Their curvature is always positive (for $T < T_{C,film}$) with increasing resistances as temperature is decreased. Consequently we consider these samples to be insulating. The insulating regime can be either due to a suppression of T_C to zero [24] or due to a proliferation of QPS [26] (or both). Observation of these two regimes indicates that a superconductor-insulator transition occurs in this family of nanowires, confirming previous results [4]. This transition occurs when the wire's $R_N \approx R_Q$ (Fig. 6.12(b)). Therefore it can be suggested that the R_N of the wire is the parameter that controls the SIT. However, since wire length was not varied over a wider range in this study we cannot exclude the possibility here that the cross-sectional area of the wire is the control parameter.

Measurements presented in Fig. 6.12 demonstrate that bare and Si-coated wires are qualitatively different. In the Si-coated wires the $R(T)$ curves are less predictable, show multiple steps or "humps" (Figs. 6.12(c) and (d)), and in some cases exhibit a mixed behavior that does not always allow them to be clearly identified as either superconducting or insulating. For example, sample B4 shows three steps on the $R(T)$ curve and a tail at the lowest temperature, which could be the beginning of the fourth transition. The first step, as always, reflects the superconducting transition in the electrodes, but the other steps correspond to some weak links in the wire itself. Some Si-coated wires exhibit both positive and negative curvature at different temperatures. Such mixed behavior is seen in samples B5 and B6, with their resistance initially dropping as

Reproduced with permission of the copyright owner. Further reproduction prohibited without permission.

in superconducting wires (i.e., with a negative curvature) but then starting to increase as in insulating wires. The conclusion is that no clear SIT at $R_N \approx R_Q$ can be observed in the family of nonhomogeneous wires.

6.3.6 dV(I)/dI measurements

A clear difference between bare and Si-coated wires is also found in the $dV(I)/dI$ measurements (Fig. 6.13). Bare MoGe wires (left column) again show one of only two distinct types of behavior. The superconducting wires exhibit a large minimum

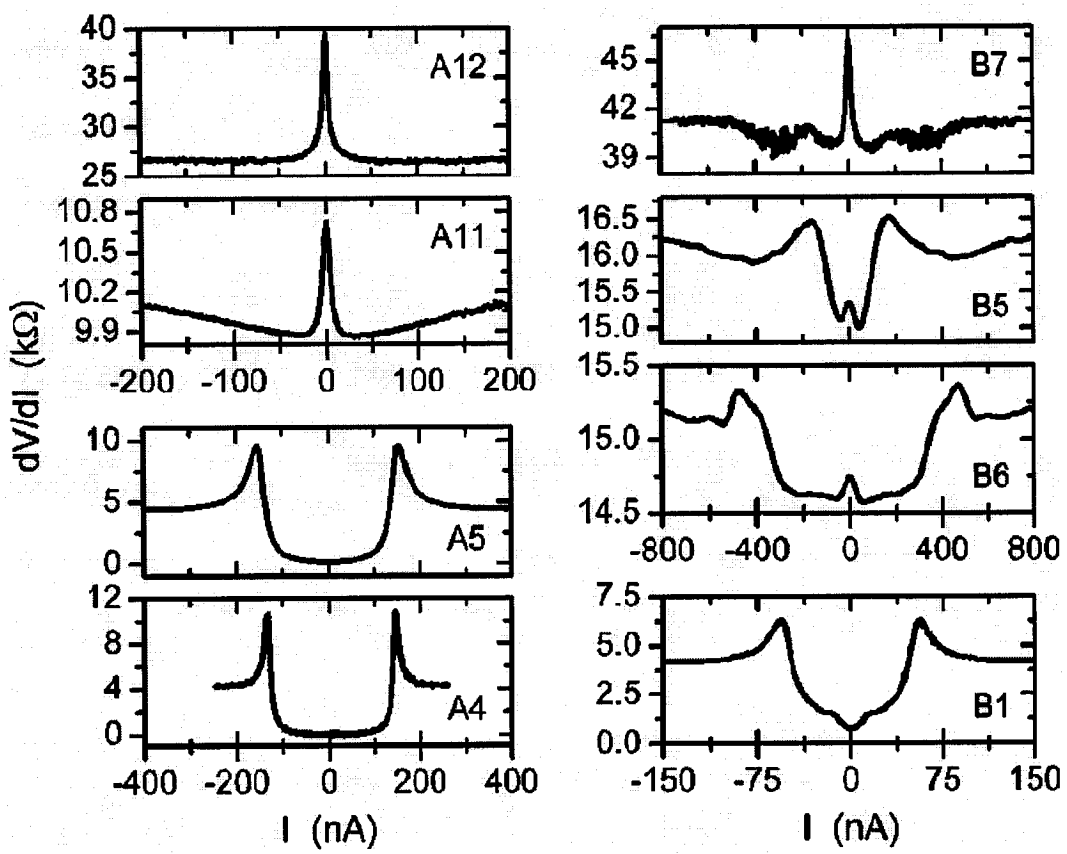

Figure 6.13: Differential resistance as a function of bias current for various bare (left column) and Si-coated (right column) samples. Measurement temperatures are 0.3 K for samples A11 and A12, 2.8 K for sample A5, 2.2 K for sample A4, and 1.5 K for samples B1, B5, B6, and B7.

Reproduced with permission of the copyright owner. Further reproduction prohibited without permission.

centered around zero bias (e.g., A4 and A5) and peaks at the bias current which is equal to the critical current of the nanowire. The insulating samples show a single zero-bias resistance peak (e.g., A11 and A12). This is in agreement with previous experiments [4].

The Si-coated MoGe wires, on the other hand, frequently show various combinations of such types of behavior. For example, sample B5 has a clear resistance depression in the range ±150 nA with the critical current peaks at the limits of this depression, and, in addition to this, a narrow zero-bias resistance peak. Such mixed behavior indicates that some parts of the wire are superconducting while other sections appear insulating. Sample B6 also shows similar results. This fact again confirms that these wires are not homogeneous.

6.3.7 Discussion of inhomogeneous wires

The properties of *inhomogeneous* wires can be understood by assuming that they contain a sequence of independent weak link constrictions, each surrounded by a dissipative region, the size of which determines the normal resistance of the WLC. Since the free-energy barriers for phase slips are different in each such WLC and the constrictions are connected in series it is clear that $R(T)$ curves should show crossings [13] and multiple steps (such as for sample B4 in Fig. 6.12(c)). Moreover some links can be insulating if their normal resistance is large enough, similar to the insulating behavior found in homogeneous wires. For example, sample B5 shows a mixed behavior that is explained by assuming it contains two WLC's - one superconducting and one insulating. The $R(T)$ curve then should show one superconducting hump and a tail with increasing resistance at lower temperatures, typical of insulating wires. Likewise, a single superconducting feature and an insulating zero-bias peak should be observed in the

Reproduced with permission of the copyright owner. Further reproduction prohibited without permission.

$dV(I)/dI$ curve. These characteristics are indeed observed (Figs. 6.12(d) and 6.13). In some wires all WLC's can be superconducting, as for example, in sample B1 (and possibly B2, B3, and B4). In the case of B1, two humps in the $R(T)$ curve (at $T \approx 5\,\mathrm{K}$ and $T \approx 2\,\mathrm{K}$) and two superconducting peaks on $dV(I)/dI$, corresponding to two critical currents (at $I \approx 15\,\mathrm{nA}$ and $I \approx 60\,\mathrm{nA}$), are observed, indicating that two superconducting WLCs are present. Finally, since each insulating WLC produces a single $dV(I)/dI$ peak located at zero current, the wires with a few insulating WLC's should nevertheless exhibit only one peak at zero bias, as could be the case for sample B7 in Fig. 6.13.

All measured homogeneous samples act as superconductors if they satisfy $R_N < R_Q$ and as insulators otherwise (Fig. 6.12(b)). Inhomogeneous wires frequently violate this condition, as for example sample B2 (Fig. 6.12(d)). This can be explained by the WLC model and by assuming that each WLC can be either insulating or superconducting depending on its own normal resistance. The sample B2 has shown two distinguishable peaks on its $dV(I)/dI$ curve (not shown), corresponding to two superconducting WLC's with slightly different critical currents. Since this sample's normal resistance is 8.30 kΩ and since two similar WLC's are detected in this wire, it can be estimated that the normal resistance of each WLC is ≈ 4.15 kΩ. Thus each WLC is superconducting and hence the entire wire is superconducting as well.

Since each WLC is manifest by a jumpwise increase of the sample resistance at the WLC's critical current, it is reasonable to associate WLC's with phase slip centers [27, 28] (which are usually positioned at weak spots along the wire). The normal

Reproduced with permission of the copyright owner. Further reproduction prohibited without permission.

resistance of a WLC is then the resistance of the dissipative region or the region which is populated by quasiparticles generated by the phase slip center. This dimension is the quasiparticle diffusion length, $\Lambda_Q \approx (D\tau_{in})^{1/2} \sim 100\,\text{nm}$, where $D \sim 10^{-4}\ \text{m}^2/\text{s}$ is the diffusion constant and $\tau_{in} \sim 10^{-10}\,\text{s}$ is the inelastic scattering time [27-29]. If constrictions are present in the wire, Λ_Q is further reduced and equals the distance between the constrictions. Our short homogeneous wires are not longer than Λ_Q, so each wire acts as a single WLC. These wires therefore show a clear SIT. Inhomogeneous wires have more than one WLC (i.e., will develop more than one phase slip center under strong current bias) and consequently show a mixed behavior.

6.3.8 Conclusions

In summary, we have found that the morphology of superconducting nanowires has a strong effect on the observed superconductor-insulator transition. A clear SIT is only found in homogeneous wires whereas inhomogeneous samples show a smeared transition and mixed behavior. In the latter case, the results are understood by the assumption that inhomogeneous wires are composed of weakly coupled sections connected in series. Each section exhibits either superconducting or insulating behavior while the entire wire shows a mixed behavior.

6.4 Final conclusions

At the beginning of this dissertation we asked a few important questions: Does a superconductor-insulator transition in one-dimensional superconducting wires exist? If so, what controls it? What are the requirements for its occurrence? And what are the

Reproduced with permission of the copyright owner. Further reproduction prohibited without permission.

natures of the superconducting and insulating phases? Also, why have quantum phase slips been observed in some experiments but not others? In completing this dissertation answers to these questions have been provided. A superconductor-insulator transition in one-dimensional wires was shown to exist for short enough wires. When the wires become too long or inhomogeneous the transition becomes smeared. The control parameter for the SIT is the total normal state resistance of the wire, with the SIT critical point occurring near $R_{N,T} = R_Q$. When $R_{N,T} < R_Q$, the wires are in a truly superconducting state that follows the predictions of the LAMH theory of thermally activated phase slips. When $R_{N,T} > R_Q$, the wires obey the predictions of the theory of weak dynamic Coulomb blockade in disordered normal metal wires. This piece of evidence as well as the observation of critical temperature suppression with increasing total normal state resistance for superconducting wires indicates that the quantum phase transition is associated with a disappearance of the amplitude of the order parameter in the insulating state - as $R_{N,T}$ increases the critical temperature is reduced until it becomes zero at the SIT critical point.

6.5 References

[†] These samples were graciously provided by Dr. Andrey Rogachev.

[‡] This sample was graciously provided by Robert Dinsmore.

[1] J. S. Langer and V. Ambegaokar, Phys. Rev. **164**, 498 (1967).

[2] D. E. McCumber and B. I. Halperin, Phys. Rev. B **1**, 1054 (1970).

Reproduced with permission of the copyright owner. Further reproduction prohibited without permission.

[3] D. S. Golubev and A. D. Zaikin, Phys. Rev. Lett. **86**, 4887 (2001); J. P. Kauppinen and J. P. Pekola, Phys. Rev. Lett. **77**, 3889 (1996); P. Joyez and D. Esteve, Phys. Rev. B **56**, 1848 (1997).

[4] A. Bezryadin, C. N. Lau, and M. Tinkham, Nature **404**, 971 (2000).

[5] C. N. Lau, N. Markovic, M. Bockrath, A. Bezryadin, and M. Tinkham, Phys. Rev. Lett. **87**, 217003 (2001).

[6] M. Tinkham, *Introduction to Superconductivity*, 2nd ed. (McGraw-Hill, New York, 1996).

[7] A. T. Bollinger, A. Rogachev, M. Remeika, and A. Bezryadin, Phys. Rev. B **69**, 180503(R) (2004).

[8] S. Chakravarty, Phys. Rev. Lett. **49**, 681 (1982); A. Schmid, Phys. Rev. Lett. **51**, 1506 (1983).

[9] J. S. Penttilä, Ü. Parts, P. J. Hakonen, M. A. Paalanen, and E. B. Sonin, Phys. Rev. Lett. **82**, 1004 (1999); H. Miyazaki, Y. Takahide, A. Kanda, and Y. Ootuka, Phys. Rev. Lett. **89**, 197001 (2002).

[10] G. Refael, E. Demler, Y. Oreg, and D. S. Fisher, Phys. Rev. B **68**, 214515 (2003).

[11] P. Xiong, A.V. Herzog, and R.C. Dynes, Phys. Rev. Lett. **78**, 927 (1997).

[12] N. Giordano, Phys. Rev. Lett. **61**, 2137 (1988).

[13] C. N. Lau, Ph.D. thesis, Harvard University, 2001.

[14] A. Frydman, Physica C **391**, 189 (2003).

[15] J. M. Valles, Jr., S. –Y. Hsu, R. C. Dynes, and J. P. Garno, Physica B **197**, 522 (1994).

[16] A. M. Finkel'stein, Physica B **197**, 636 (1994).

Reproduced with permission of the copyright owner. Further reproduction prohibited without permission.

[17] D. B. Haviland, Y. Liu, and A. M. Goldman, Phys. Rev. Lett. **62**, 2180 (1989).

[18] A. Goldman and N. Markovic, Phys. Today **51** (11), 39 (1998).

[19] R. P. Barber, Jr., L. M. Merchant, A. La Porta, and R. C. Dynes, Phys. Rev. B **49**, 3409 (1994).

[20] A. Frydman, O. Naaman, and R. C. Dynes, Phys. Rev. B **66**, 052509 (2002).

[21] E. T. Mickelson, C. B. Huffman, A. G. Rinzler, R. E. Smalley, R. H. Hauge and J. L. Margrave, Chem. Phys. Lett. **296**, 188 (1998).

[22] The sputtering was DC for MoGe and RF for the Si overlayer. The sputterer was equipped with an LN_2 cold trap.

[23] J. M. Graybeal and M. R. Beasley, Phys. Rev. B **29**, 4167 (1984).

[24] Y. Oreg and A. M. Finkel'stein, Phys. Rev. Lett. **83**, 191 (1999).

[25] A. Rogachev and A. Bezryadin, Appl. Phys. Lett. **83**, 512 (2003).

[26] A. D. Zaikin, D. S. Golubev, A. van Otterlo, and G. T. Zimanyi, Phys. Rev. Lett. **78**, 1552 (1997).

[27] W. J. Skocpol, M. R. Beasley, and M. Tinkham, J. Low Temp. **16**, 145 (1974).

[28] R. Tidecks, *Current-Induced Nonequilibrium Phenomena in Quasi-One-Dimensional Superconductors* (Springer-Verlag, New York, 1990).

[29] J. M. Graybeal, Ph.D. thesis, Stanford University, 1985.

Reproduced with permission of the copyright owner. Further reproduction prohibited without permission.

Chapter 7

Additional Measurements: Superconducting Nanobridges

The results and text of this chapter were published under the title "Phase Slips in Superconducting Films with Constrictions" and are repeated here. Reprinted with permission from Sang L. Chu, Anthony T. Bollinger, and Alexey Bezryadin, Physical Review B **70**, 214506 (2004). Copyright 2004 by the American Physical Society.

7.1 Introduction

Thermally activated vortex-like excitations (topological defects) of the superconducting condensate are the primary source of dissipation in mesoscopic superconducting structures [1] These fluctuations take different forms in one-dimensional (1D) and two-dimensional (2D) systems. In 2D thin films the fluctuations are known to be broken vortex-antivortex pairs [2–11] while in 1D wires the resistance is due to phase slips [12–21]. One important difference between these two types of fluctuations is that vortices and antivortices form bound pairs below a certain critical temperature, known as the Berezinskii-Kosterlitz-Thouless (BKT) transition temperature, while phase slips and anti-phase-slips are unbound at any finite temperature. Thus the resistance of 1D wires is greater than zero at any finite temperature due to the presence of

Reproduced with permission of the copyright owner. Further reproduction prohibited without permission.

phase slips, which are described by the theory of Langer, Ambegaokar, McCumber, and Halperin (LAMH) [13, 14].

Here we report a study of structures in which both types of fluctuations can coexist, namely, thin films containing constrictions, which are comparable in size to the coherence length. The goals of this work are (i) to test the applicability of the LAMH theory for short and rather wide constrictions and (ii) to test the effect of the vortex-antivortex sea existing in the thin film banks adjacent to the constriction on the phase slippage rate on the constriction itself. For this purpose we fabricate and measure a series of thin superconducting MoGe films [22] (which are about 15 μm wide) interrupted by constrictions or "bridges" (see Fig. 7.1(a)). The width of the narrowest point of the bridges is in the range of 13–28 nm, i.e., a few times larger than the coherence length (we

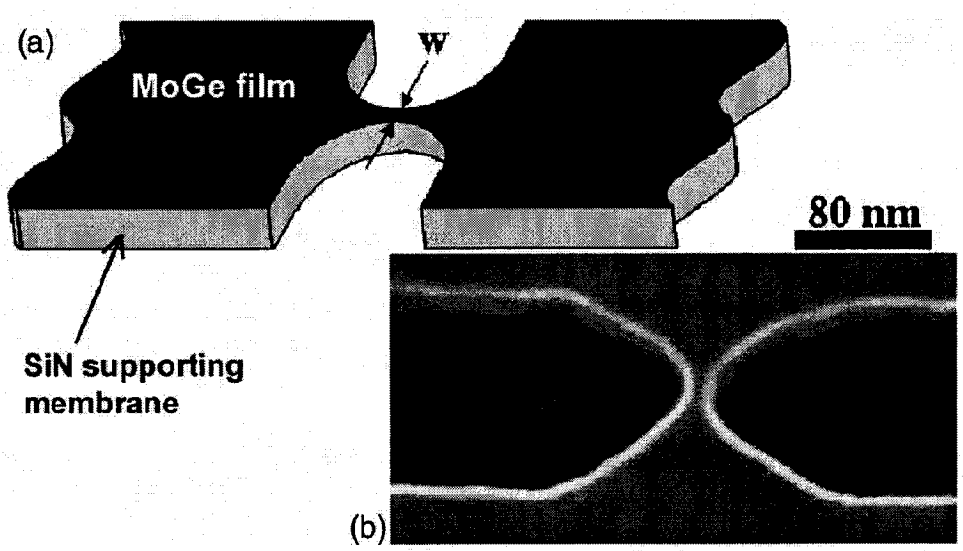

Figure 7.1: (a) Sample schematic. MoGe film (black) of thickness $d = 2.5 - 4.5$ nm is deposited over a SiN membrane (gray) substrate with a constriction of width w. (b) An SEM micrograph of a typical sample. The MoGe coated SiN bridge (gray) is suspended over a deep trench (black).

Reproduced with permission of the copyright owner. Further reproduction prohibited without permission.

estimate $\xi(0) \approx 7$ nm for our MoGe films [23]). Two resistive transitions are observed in such samples indicating that the vortex-antivortex pair binding-unbinding transition (if any) and thermally activated phase slip processes occur separately. For $T > T_{BKT}$ the contribution of vortex-antivortex pairs is dominant. On the other hand, below T_{BKT} the transport properties are determined by the phase slip process on the bridge, which may be regarded as a vortex-antivortex pair breaking assisted by the bridge.

Using direct and indirect techniques we have tracked the sample's resistance within a range of eleven orders of magnitude. The resulting $R(T)$ curves are compared with the LAMH theory. Regardless of the large width of the bridges and their shortness, the shape of the measured $R(T)$ curves is in perfect agreement with the overall shape of the curves computed using the standard LAMH theory (note that this theory was originally derived for very long wires that are much thinner than the coherence length). The only disagreement found with LAMH is that the preexponential factor had to be modified in order to obtain a reasonably low critical temperature of the bridges. The critical temperature is used as an adjustable parameter in the fitting procedure. Following the argument of Little [12] we arrive at the conclusion that the preexponential factor should be simply R_N and obtain a good agreement with measured curves. The measurements show that the bridges with intermediate dimensions (i) allow phase slippage which does not quench at any finite temperature, (ii) behave independently of the thin film banks, and (iii) exhibit a higher rate of phase slippage in the cases when the width of the bridge is smaller and therefore when the coupling between the thin film banks is weaker.

Reproduced with permission of the copyright owner. Further reproduction prohibited without permission.

Before presenting our experimental results we give a brief summary of the BKT theory of topological phase transitions and the LAMH theory of thermally activated phase slips. In thin superconducting films, even in the absence of a magnetic field, an equal population of free vortices and antivortices is expected to occur. The BKT theory predicts a universal jump in the film superfluid density n_s at the characteristic temperature T_{BKT}, lower than the mean-field critical temperature of the film T_{c0}. Such a jump is related to the vortex-antivortex pair binding through a logarithmic interaction potential between free vortices [3, 26]. Applied currents can break bound pairs producing free vortices which lead to nonlinear $V(I)$ curves. Above T_{BKT} the linear resistance of a film is given by the Halperin-Nelson (HN) formula [6, 9]

$$R_{HN} = 10.8bR_{n,f}\exp\left[-2\sqrt{(T_{c0}-T_{BKT})/(T-T_{BKT})}\right] \tag{7.1}$$

where $R_{n,f}$ is the normal state resistance per square of the film and b is a nonuniversal constant. Note that the HN equation predicts zero resistance for temperatures below the BKT phase transition temperature T_{BKT}.

The LAMH theory [1, 12-14] applies to narrow superconducting channels, in which thermal fluctuations can cause phase slips, i.e., jumps by 2π of the phase difference of the superconducting order parameter. In unbiased samples the number of phase slips (which change the phase difference by 2π) equals the number of anti-phase-slips (which change the phase difference by -2π). An applied bias current pushes the system away from equilibrium and the number of phase slips becomes larger than the number of anti-phase-slips. Thus a net voltage appears on the sample, which can be calculated, following LAMH, as $V = \hbar\dot{\phi}/2e$ (below we will also discuss an alternative

Reproduced with permission of the copyright owner. Further reproduction prohibited without permission.

approach to the voltage definition). Here $\hbar$ is Planck's constant, e is the electron charge, and $\dot{\phi}$ is the rate of change of the phase difference between the ends of the wire. During the phase slip process the energy of the system increases since the order parameter becomes suppressed to zero in the center of the phase slip. Thermal activations of the system over this free energy barrier $\Delta F(T)$ occur at a rate given by $\left(\Omega(T)/2\pi\right)e^{-\Delta F/k_B T}$. If the bias current is not zero, then the net rate of the phase slippage is $\dot{\phi} = \Omega(T)\left(e^{-\Delta F_+(I)/k_B T} - e^{-\Delta F_-(I)/k_B T}\right)$. Here I is the bias current, and ΔF_+ and ΔF_- are the barriers for phase slips and anti-phase-slips correspondingly (these two barriers become equal to each other at zero bias current). The attempt frequency derived from a time-dependent Ginzburg-Landau (GL) theory, for the case of a long and thin wire, is [14]

$$\Omega(T) = \frac{L}{\xi(T)}\frac{1}{\tau_{GL}}\left(\frac{\Delta F}{k_B T}\right)^{1/2} \tag{7.2}$$

where T is the temperature of the wire and $L/\xi(T)$ is the length of the wire measured in units of the GL coherence length $\xi(T)$. The attempt frequency is inversely proportional to the relaxation time $\tau_{GL} = \pi\hbar/8k_B(T_c - T)$ of the time-dependent GL theory, with T_c being the mean-field critical temperature of the wire (or of the bridge, as in our discussions below). The factor $\left(\Delta F/k_B T\right)^{1/2}$ provides a correction for the overlap of fluctuations at different places of the wire and the factor $L/\xi(T)$ gives the number of statistically independent regions in the wire [14]. The free energy barrier for a single phase slip is given by [13, 18]

Reproduced with permission of the copyright owner. Further reproduction prohibited without permission.

$$\Delta F = \frac{8\sqrt{2}}{3}\frac{H_c^2(T)}{8\pi}A\xi(T) \tag{7.3}$$

which is essentially the condensation energy density $H_c^2(T)/8\pi$ multiplied by the effective volume $8\sqrt{2}A\xi(T)/3$ of a phase slip (A is the cross-sectional area of the wire).

A bias current I causes a nonzero voltage (time averaged) given by

$$V = \frac{\hbar\Omega(T)}{e}e^{-\Delta F/k_BT}\sinh(I/I_0) \tag{7.4}$$

where $I_0 = 4ek_BT/h$ ($I_0 = 13.3\,\text{nA}$ at $T = 1\,\text{K}$). Differentiation of this expression with respect to the bias current I gives the differential resistance

$$dV/dI = \frac{\hbar\Omega(T)}{eI_0}e^{-\Delta F/k_BT}\cosh(I/I_0) \tag{7.5}$$

The dependence of the attempt frequency and free energy on the bias current is neglected in this derivation. In the limit of low currents $I \ll I_0$, Ohm's law is recovered

$$R_{LAMH}(T) = \frac{\hbar\Omega(T)}{eI_0}e^{-\Delta F/k_BT} = R_Q\left(\frac{\hbar\Omega(T)}{k_BT}\right)e^{-\Delta F/k_BT} \tag{7.6}$$

where $R_Q = h/(2e)^2 = 6.5\,\text{k}\Omega$. In this approach the fluctuation resistance does not have any explicit dependence on the normal resistance of the wire.

7.2 Experimental setup

The sample geometry is shown schematically in Fig. 7.1(a). The fabrication is performed starting with a Si wafer covered with SiO_2 and SiN films. A suspended SiN bridge is formed using electron beam lithography, reactive ion etching, and HF wet etching [24]. The bridge and the entire substrate are then sputter coated with amorphous

Reproduced with permission of the copyright owner. Further reproduction prohibited without permission.

Sample	w (nm)	R_N (Ω)	T_c (K)	T_{c0} (K)	d (nm)	β
A1	27 ± 4	1380	3.88	3.90	2.5	1.47
B1	13 ± 4	1650	4.80	4.91	3.5	0.723
B2	28 ± 4	1320	4.81	4.91	3.5	1.10
C1	13 ± 4	1440	5.16	5.50	4.5	0.653
C2	27 ± 4	680	5.39	5.50	4.5	2.21

Table 7.1: Sample parameters, including the width of the constriction (w), determined from SEM images, normal resistance of the bridge (R_N), determined from the $R(T)$ curves (at a temperature slightly below the resistive transition of the thin film banks), critical temperature (T_c), determined from $R_{WL}(T)$ fits given by Eq. 7.9, critical temperature of the film (T_{c0}), film thickness (d), and a geometrical fitting parameter (β).

$Mo_{79}Ge_{21}$ superconducting alloy, topped with a 2 nm overlayer of Si for protection [25] The resulting bridges are 100 nm long with a minimum width $w \approx 13-28$ nm as measured with a scanning electron microscope (SEM) (Fig. 7.1(b)). All samples are listed in Table 7.1.

Transport measurements are performed in a pumped ^{4}He cryostat equipped with a set of rf-filtered leads. The linear resistance $R(T)$ is determined from the low-bias slope (the bias current is in the range of 1-10 nA) of the voltage versus current curves. The high-bias differential resistance is measured using an ac excitation on top of a dc current offset generated by a low-distortion function generator (SRS-DS360) connected in series with a 1 MΩ resistor. One sample was measured down to the mΩ level using a low-temperature transformer manufactured by Cambridge magnetic refrigeration.

Reproduced with permission of the copyright owner. Further reproduction prohibited without permission.

7.3 Results

First we compare a sample with a hyperbolic constriction ("bridge sample") with a reference sample, which is a plain MoGe film of the same thickness, without any constriction ("film sample"). Both are fabricated on the same substrate simultaneously. A resistive transition measured on the film sample is shown in Fig. 7.2. The HN fit

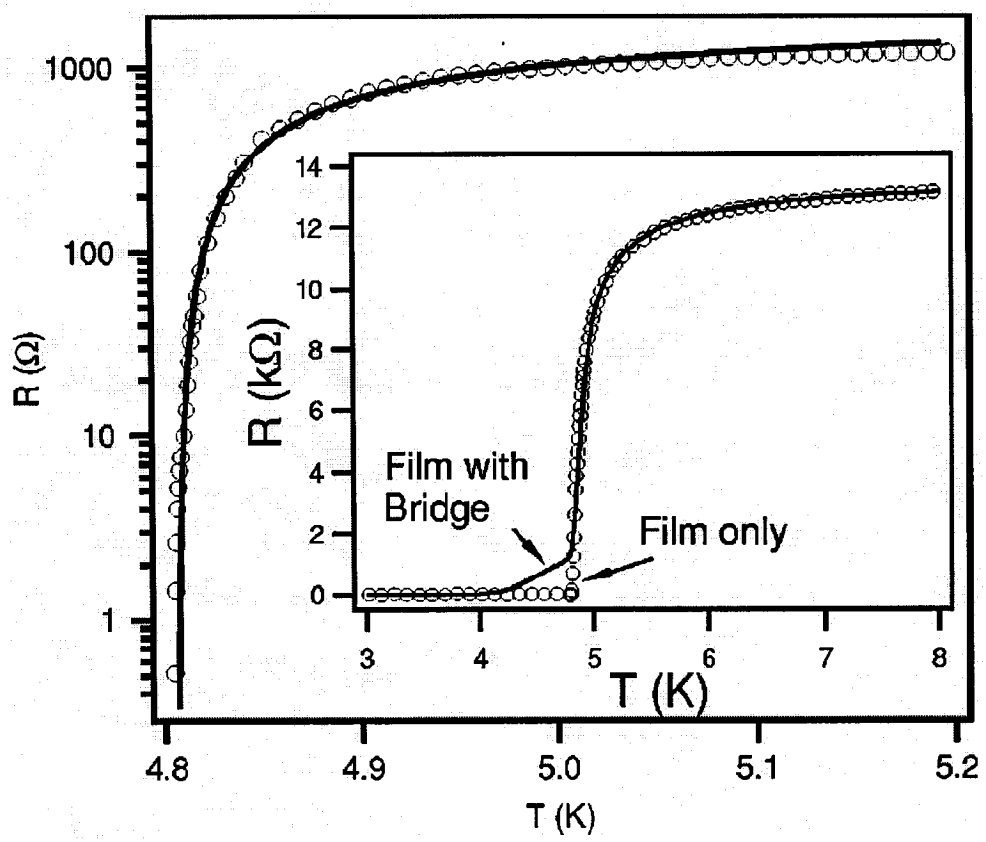

Figure 7.2: Low-bias resistance versus temperature dependence (open circles), measured on a thin film ($d = 3.5$ nm) without constriction. The solid line is a fit to the Halperin-Nelson theory (Eq. 7.1). (Inset) Resistance of the film without constriction (multiplied by a constant factor), shown as open circles, is compared to the sample with a hyperbolic bridge (B2), shown by the solid line. The only qualitative difference is the presence of a "resistive tail," observed on all samples with constrictions.

Reproduced with permission of the copyright owner. Further reproduction prohibited without permission.

generated by Eq. 7.1 is shown as a solid line and exhibits a good agreement with the data, yielding a BKT transition temperature of $T_{BKT} = 4.8\,\mathrm{K}$ and a mean-field critical temperature $T_{c0} = 4.91\,\mathrm{K}$. Such good fit suggests that the transition observed in the banks might be the BKT transition, although a more extensive set of experiments is necessary in order to prove this assumption rigorously. As expected, T_{BKT} is slightly lower than T_{c0}. The inset of Fig. 7.2 compares the $R(T)$ measurements of the "film" (open circles) and the "bridge" (solid line) samples. At $T = 4.8\,\mathrm{K}$ the $R(T)$ curve for the film sample crosses the $R = 0$ axis with a nonzero (and large) slope, in agreement with the behavior predicted by the HN resistance equation (Eq. 7.1). Nevertheless, unlike the film sample, the bridge sample shows a nonzero resistance even below the BKT transition temperature predicted by Eq. 7.1. Such resistive tails, occurring at $T < T_{BKT}$, have been found in all samples with constrictions.

In Fig. 7.3 the $R(T)$ curves for five samples with bridges are plotted in a log-linear format. The resistance of sample B1 has been measured down to the mΩ range using a low-temperature transformer. Two resistive transitions are seen in each curve as the temperature decreases. The first transition is the superconducting transition in the thin film banks adjacent to the bridge. The second transition corresponds to the resistive tail mentioned above. In order to understand the origin of the second transition it should be compared to the LAMH theory.

Reproduced with permission of the copyright owner. Further reproduction prohibited without permission.

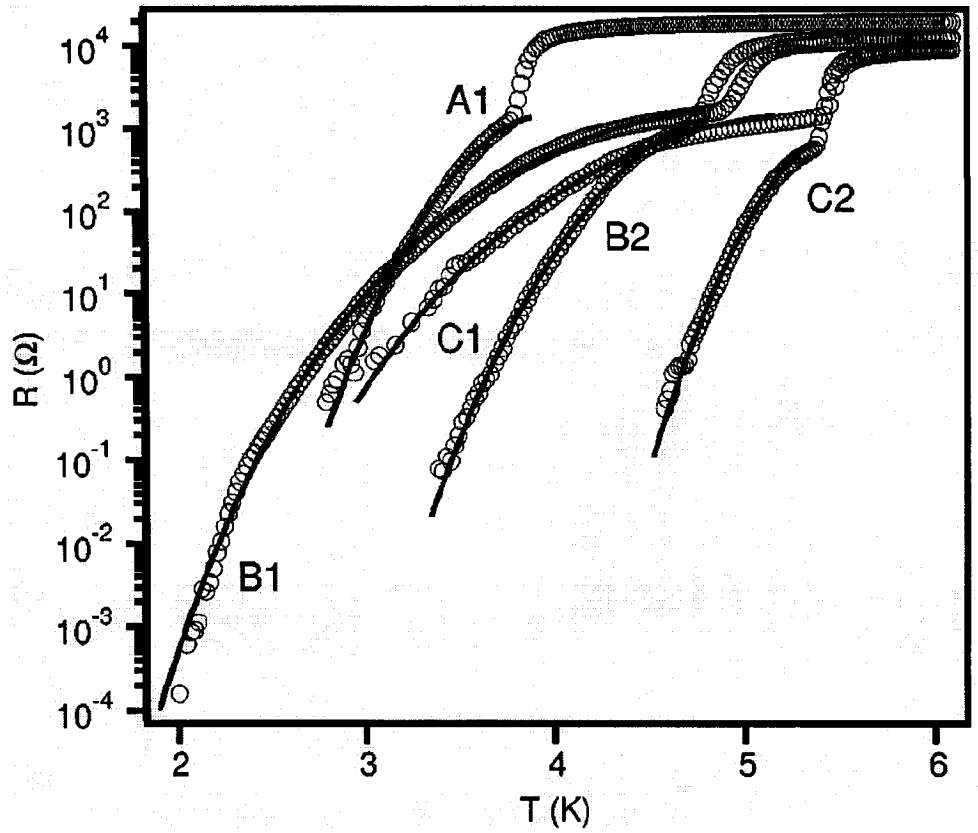

Figure 7.3: Low-bias resistance for five different samples with bridges. The parameters of the samples are given in Table 7.1. The data points are shown by open symbols. Solid lines are fits to the "bridge" phase slip model given by Eqs. 7.7 and 7.9.

7.4 Discussion

Below we analyze the resistive tails found on samples with a constriction and demonstrate that they are caused by the phase slip events localized on the bridge and behave independently of the adjacent thin film banks. The analysis indicates that no BKT (no vortex-antivortex binding within the constrictions) or any other type of transition occurs on the constrictions and that the phase slips and anti-phase-slips are unpaired at any nonzero temperature due to thermal fluctuations. This is demonstrated below by fitting the $R(T)$ curves with the LAMH-like fitting curves.

Reproduced with permission of the copyright owner. Further reproduction prohibited without permission.

7.4.1 LAMH attempt frequency for a short bridge

In order to compare our results to the LAMH theory we have to take into account the small length of the bridge, which does not allow more than one phase slip at a given time. Therefore the attempt frequency $\Omega(T)$ of Eq. 7.2 can be simplified. First, it has a term $L/\xi(T)$ that accounts for the number of independent sites where a phase slip can occur [14]. Since each of our samples has only one narrow region where phase slip events can happen, we take $L/\xi(T)=1$. Second, the coefficient $(\Delta F/k_BT)^{1/2}$ which takes into account possible overlaps of phase slips at different places along the wire [14] is taken to be unity also. This is because for short hyperbolic bridges (not much longer than the coherence length) it is reasonable to expect that there is only one spot, i.e., the narrowest point of the bridge, where phase slips occur. As a result, we obtain the attempt frequency for a short hyperbolic bridge $\Omega_{WL}=1/\tau_{GL}$ (the abbreviation "WL" stands for "weak link"). This attempt frequency can be combined with the usual form of the LAMH resistance in Eq. 7.6 and can be used to fit the experimental $R(T)$ curves (below the resistive transition of the films). Although such fits follow the data very well, there is one inconsistency, that is they require the critical temperature of the bridge to be chosen higher than the critical temperature of the films, which is unphysical for such a system. We attempt to modify the preexponential factor in order to resolve this inconsistency, as discussed below.

7.4.2 Modification of the prefactor

Since the exact expression is unknown, we approximate the resistance of a constriction (weak link) as

Reproduced with permission of the copyright owner. Further reproduction prohibited without permission.

$$R_{WL}(T) = R_N e^{-\Delta F/k_B T} \tag{7.7}$$

The exponential factor here is that of the LAMH theory and the prefactor is simply the normal resistance of the bridge. This expression (Eq. 7.7) can be justified by the following argument: the duration of a single phase slip (i.e., the time it takes for the order parameter to recover) is $\sim \tau_{GL}$ and the number of phase slips occurring per second is $\sim \Omega_{WL}(T)\exp\left[-\Delta F(T)/k_B T\right]$, with the attempt frequency being the inverse GL relaxation time $\Omega_{WL} = 1/\tau_{GL}$, as was argued above. Therefore the time fraction during which the constriction is experiencing a phase slip (i.e., when superconductivity is suppressed on the bridge) is the product of these two values, i.e., $f = (\tau_{GL})(1/\tau_{GL})\exp\left[-\Delta F(T)/k_B T\right] = \exp\left[-\Delta F(T)/k_B T\right]$. Following Little [12], it can be assumed that the bridge has the normal resistance R_N during the time when a phase slip is present (i.e., when the bridge is in the normal state), and the resistance is zero otherwise (when there is no phase slip). Thus we arrive at the averaged resistance for a bridge or a small size weak link $R_{WL} = f \times R_N + (1-f)\times 0 = R_N \exp\left[-\Delta F(T)/k_B T\right]$ as in Eq. 7.7. Note that unlike in the LAMH theory, in the present formulation the fluctuation resistance is directly linked to to the normal state resistance of the sample.

In order to compare Eq. 7.7 to the experimental results, an explicit expression for the energy barrier ΔF_{WL} for a phase slip localized on the bridge is required. Starting with the usual form [18] derived for a long 1D wire and some well known results from BCS and GL theory [1,18], we find that $\Delta F_{WL}(0) = \left(8\sqrt{2}/3\right)\left[H_c^2(0)/8\pi\right] A\xi(0)$

Reproduced with permission of the copyright owner. Further reproduction prohibited without permission.

$= 0.83 k_B T_c R_Q L / R_N \xi(0)$, where L is the length of the weak link. Using $R_N = \rho_n L / A$, the free energy barrier for a weak link is

$$\Delta F_{WL}(0) = 0.83 k_B T_c \frac{\beta w d R_Q}{\rho_n \xi(0)} \tag{7.8}$$

where w is the width of the bridge, d is the film thickness, ρ_n is the normal resistivity, and $A = wd$. The parameter β measures the ratio of the phase slip length along the bridge to the effective length of a phase slip in a 1D wire, which is equal to $8\sqrt{2}\xi(T)/3$. Finally, assuming the same temperature dependence of the barrier as in the LAMH theory, i.e., $\Delta F(T) = \Delta F(0)(1 - T/T_c)^{3/2}$, we arrive at the expression for the bridge fluctuation-induced resistance

$$R_{WL}(T) = R_N \exp\left[-0.83 \frac{\beta w d R_Q}{\rho_n \xi(0)} \left(1 - \frac{T}{T_c}\right)^{3/2} \frac{T_c}{T} \right] \tag{7.9}$$

The fits generated by Eq. 7.9 are shown in Fig. 7.3 as solid lines. An impressively good agreement is found for all five samples. In particular, sample B1 measured using the low-temperature transformer, shows an agreement with the predicted resistance R_{WL} over about seven orders of magnitude, down to a temperature that is more than two times lower compared to the critical temperature of the sample. Only two fitting parameters are used: β and T_c (listed in Table 7.1). The other parameters required in Eq. 7.9, including R_N, d, w, $\xi(0) \approx 7$ nm, and $\rho_n \approx 180$ μΩ-cm are known [18, 19, 23]. The fits give quite reasonable values for the critical temperature of the bridges, in the sense that they are slightly lower than the corresponding critical temperatures of thin films of the same thickness, as expected. This fact supports the validity of Eq. 7.7. Such good agreement

Reproduced with permission of the copyright owner. Further reproduction prohibited without permission.

also indicates that the dissipation in a thin film with a constriction at $T < T_{BKT}$ is solely due to thermal activation of phase slips on constrictions. As expected, $\beta \approx 1$ for all samples and the larger β values are found on wider constrictions.

7.4.3 Determination of the linear resistance from high bias current measurements

We now discuss the nonlinear properties of films with constrictions. Measurements of the differential resistance versus bias current dV/dI vs I are plotted in Fig. 7.4 on log-linear scale. Using these results it is possible to distinguish between the BKT mechanism, which leads to a power-law $V(I)$ dependence, and the phase slippage process, which is characterized by an exponential $V(I)$ dependence (Eqs. 7.4 and 7.5). From Fig. 7.4 it is clear that at $T < T_{BKT}$ and sufficiently low currents the dependence of the differential resistance on bias current is exponential (it appears linear on the log-linear plots). Thus it is appropriate to compare the results with the LAMH theory. Equation 7.5 can be written as $dV/dI = R(T)\cosh(I/I_0)$, where $R(T)$ is the temperature-dependent zero-bias resistance. Using this relation, we fit the differential resistance data and use $R(T)$ as a fitting parameter, as shown in Fig. 7.4 by solid lines, each corresponding to a fixed temperature [27]. The fitting procedure illustrated in Fig. 7.4 gives us a powerful indirect method of determination of the zero-bias resistance. This method is useful when the temperature is low and the resistance of the sample is below the resolution limit of the experimental setup. Thus, by fitting the $dV(I)/dI$ curves, we obtained the zero-bias resistance $R(T)$ down to very low values ($\sim 10^{-8}\ \Omega$). This method was systematically

Reproduced with permission of the copyright owner. Further reproduction prohibited without permission.

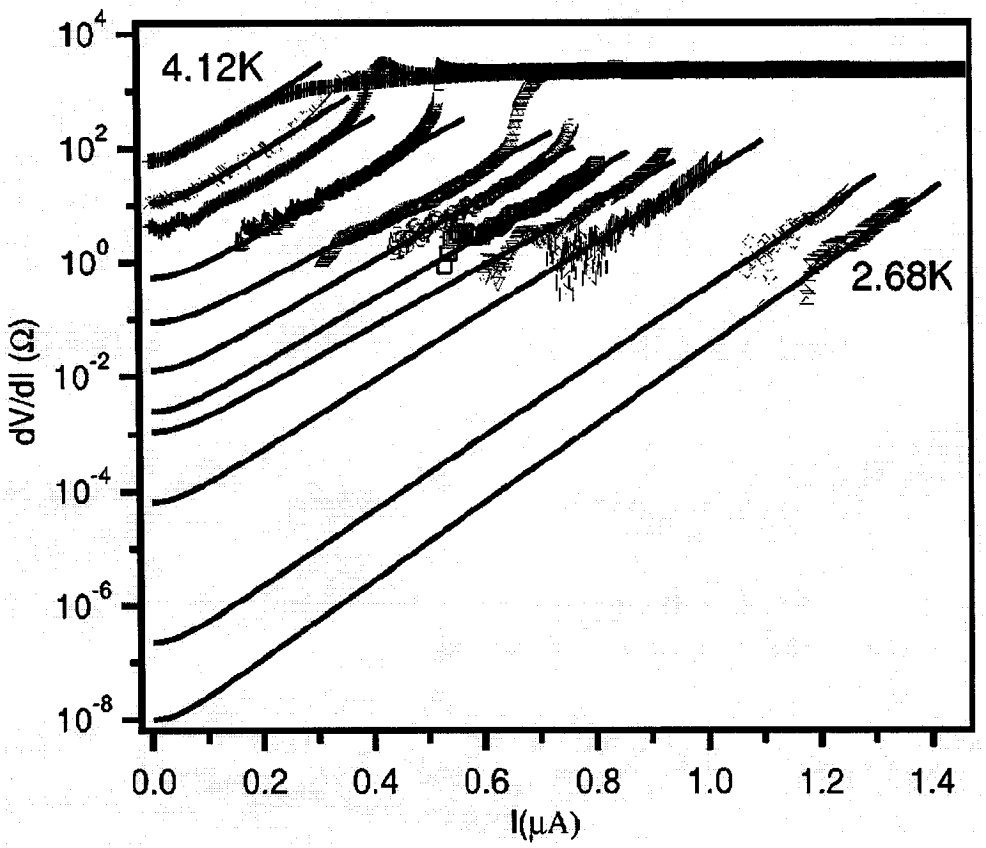

Figure 7.4: Differential resistance as a function of the dc bias current for sample B2. Experimental data are denoted by open symbols and the solid lines are fits to $dV/dI = R(T)\cosh(I/I_0)$. Temperatures from left to right are 4.12, 3.92, 3.80, 3.64, 3.45, 3.36, 3.26, 3.16, 3.07, 2.80, and 2.68 K.

applied on sample B2 and the results are shown in Fig. 7.5 as solid squares. The open circles in Fig. 7.5 represent the zero-bias resistance obtained by direct measurements at low bias currents. The two sets of data are consistent with each other. The solid curve in Fig. 7.5 is a R_{WL} fit obtained using Eq. 7.9. An excellent agreement is seen in a wide range of resistances spanning eleven orders of magnitude. This reconfirms that the

Reproduced with permission of the copyright owner. Further reproduction prohibited without permission.

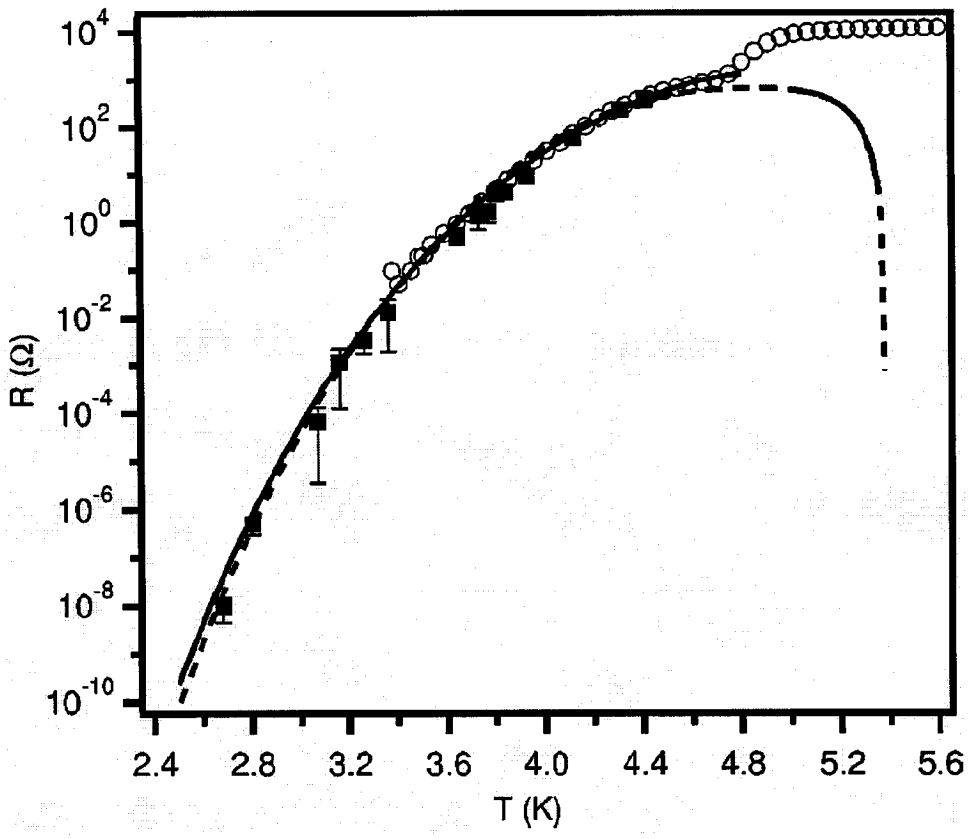

Figure 7.5: Resistance vs temperature curve for sample B2. Open circles represent data that have been directly measured while filled boxes give the resistance values determined by fitting the dV/dI curves of Fig. 7.4 using the formula $dV/dI = R(T)\cosh(I/I_0)$. The solid and the dashed curves give the best fits generated by the $R_{WL}(T)$ ($T_c = 4.81\,\mathrm{K}$) and $R_{LAMH}(T)$ ($T_c = 5.38\,\mathrm{K}$) formulas, respectively.

thermally activated phase slip mechanism is dominant in the bridge samples [29] for $T < T_{BKT}$. We emphasize that the critical temperature of the bridge, which is used as an adjustable parameter, is found to be $T_c = 4.81\,\mathrm{K}$. As expected, the T_c of the bridge is slightly lower than the critical temperature of the film electrodes $T_{c0} = 4.91\,\mathrm{K}$.

The usual LAMH expression R_{LAMH} (Eq. 7.6), which applies to thin superconducting wires [18–20, 23], can also be used to fit our data. The overall shape of

Reproduced with permission of the copyright owner. Further reproduction prohibited without permission.

the fitting curve (dashed curve in Fig. 7.5) agrees with the data as well as with the R_{WL} fit. The drawback of the usual LAMH formula is that the critical temperature of the bridge, which is used as an adjustable parameter, turns out considerably higher than the film transition temperature. For example, the dashed line fit in Fig. 7.5 is generated using $T_c = 5.38\,\mathrm{K}$ which is larger than the film critical temperature $T_{c0} = 4.91\,\mathrm{K}$. This apparent enhancement of the critical temperature of the bridge must be an artifact, because a reduction of the dimensions of MoGe samples always leads to a reduction of the critical temperature [28]. On the other hand, the T_c extracted from the fits made using Eq. 7.9 are almost equal but slightly lower than the film T_{c0} (Table 7.1), as expected.

A rapid decrease of the LAMH resistance at temperatures very close to the critical temperature reflects the behavior of the LAMH attempt frequency which approaches zero as $T \to T_c$. The LAMH resistance is proportional to the attempt frequency so we observe $R \to 0$ as $T \to T_c$ (dashed curve in Fig. 7.5). Such behavior is unphysical and occurs since the LAMH theory is not applicable very near T_c. It should be emphasized that some of our measured bridges are wider than $\xi(0)$, yet the thermally activated phase slip model agrees well with the data. This is in agreement with the prediction (Ref. 13, p. 510) that superconducting channels of width $w \leq 4.4\xi(T)$ should exhibit a 1D behavior, i.e., nucleation of vortices is unfavorable in such channels. Such condition is true for all of our samples.

Reproduced with permission of the copyright owner. Further reproduction prohibited without permission.

7.5 Summary

Fluctuation effects in thin films interrupted by "hyperbolic" constrictions are studied. The measurements show two separate resistive transitions. The higher-temperature transition shows some properties of a BKT transition in the films (follows the HN formula). The second apparent resistive transition is explained by a continuous reduction of the rate of thermally activated phase slips with decreasing temperature. A quantitative description of the fluctuation resistance of narrow and short superconducting constrictions is achieved. For this purpose we have modify the LAMH expression for the resistance of a one-dimensional nanowire. An indirect method that enables us to trace the resistance variation over eleven orders of magnitude is suggested, based on the analysis of the nonlinear effects occurring at high bias currents. The phase slippage model is found applicable in the entire range of measured resistances, suggesting that quantum phase slips [19] do not occur in these samples, in the studied temperature interval, which extends below $T_c/2$ for one sample (B1).

We thank P. Goldbart and M. Fisher for suggestions. S. L. C. thanks the support of NSF Grant No. PHY-0243675.

7.6 References

[1] M. Tinkham, *Introduction to Superconductivity*, 2nd ed. (McGraw-Hill, New York, 1996).

[2] V. L. Berezinskii, Zh. Eksp. Teor. Fiz. **59**, 907 (1970) [Sov. Phys. JETP **32**, 493 (1971)].

[3] J. M. Kosterlitz and D. J. Thouless, J. Phys. C **6**, 1181 (1973).

Reproduced with permission of the copyright owner. Further reproduction prohibited without permission.

[4] J. M. Kosterlitz, J. Phys. C **7**, 1046 (1974).

[5] M. R. Beasley, J. E. Mooij, and T. P. Orlando, Phys. Rev. Lett. **42**, 1165 (1979).

[6] B. I. Halperin and D. R. Nelson, J. Low Temp. Phys. **36**, 599 (1979).

[7] P. Minnhage, Rev. Mod. Phys. **59**, 1001 (1987).

[8] P. A. Bancel and K. E. Gray, Phys. Rev. Lett. **46**, 148 (1981).

[9] A. F. Hebard and A. T. Fiory, Phys. Rev. Lett. **50**, 1603 (1983).

[10] M. M. Rosario, Yu. Zadorozhny, and Y. Liu, Phys. Rev. B **61**, 7005 (2000).

[11] D. R. Strachan, C. J. Lobb, and R. S. Newrock, Phys. Rev. B **67**, 174517 (2003).

[12] W. A. Little, Phys. Rev. **156**, 396 (1967).

[13] J. S. Langer and V. Ambegaokar, Phys. Rev. **164**, 498 (1967).

[14] D. E. McCumber and B. I. Halperin, Phys. Rev. B **1**, 1054 (1970).

[15] J. E. Lukens, R. J. Warburton, and W. W. Webb, Phys. Rev. Lett. **25**, 1180 (1970).

[16] R. S. Newbower, M. R. Beasley, and M. Tinkham, Phys. Rev. B **5**, 864 (1972).

[17] F. Sharifi, A.V. Herzog, and R.C. Dynes, Phys. Rev. Lett. **71**, 428 (1993).

[18] M. Tinkham and C. N. Lau, Appl. Phys. Lett. **80**, 2946 (2002).

[19] C. N. Lau, N. Markovic, M. Bockrath, A. Bezryadin, and M. Tinkham, Phys. Rev. Lett. **87**, 217003 (2001).

[20] A. Rogachev and A. Bezryadin, Appl. Phys. Lett. **83**, 512 (2003).

[21] A. T. Bollinger, A. Rogachev, M. Remeika, and A. Bezryadin, Phys. Rev. B **69**, 180503(R) (2004).

[22] J. M. Graybeal and M. R. Beasley, Phys. Rev. B **29**, 4167 (1984); J. M. Graybeal, Ph.D. thesis, Stanford University, 1985.

Reproduced with permission of the copyright owner. Further reproduction prohibited without permission.

[23] A. Bezryadin, C. N. Lau, and M. Tinkham, Nature (London) **404**, 971 (1999).

[24] A. Bezryadin and C. Dekker, J. Vac. Sci. Technol. B **15**, 793 (1997).

[25] MoGe was dc sputtered while Si was rf sputtered. The sputtering system was equipped with a liquid-nitrogen-filled cold trap and had a base pressure of 10^{-7} Torr.

[26] A. M. Kadin, K. Epstein, and A. M. Goldman, Phys. Rev. B **27**, 6691 (1983).

[27] The parameter I_0 was also used as a fitting parameter in order to obtain the best fitting results. Some deviations of this parameter from the theoretical value $I_0 = 4ek_BT/h$ can be explained by the Joule heating of the bridges, which may become significant high bias currents.

[28] Y. Oreg and M. Finkel'stein, Phys. Rev. Lett. **83**, 191 (1999).

[29] This same method of resistance determination from high bias differential resistance measurements were applied to superconducting $Mo_{79}Ge_{21}$ nanowires templated by nanotubes (see Refs. [19–21, 23] regarding general information about the sample fabrication) and found to also work over a resistance range of twelve orders of magnitude. This data is to be published elsewhere.

Reproduced with permission of the copyright owner. Further reproduction prohibited without permission.

Author's Biography

Anthony Travis Bollinger was born on January 23, 1977 in Kokomo, Indiana and was raised in Elwood, Indiana. He graduated from Purdue University in 1999 with a B.S. in physics, completing the honors curriculum. While at Purdue, Anthony received a Freshman Physics Scholarship and a School of Science Scholarship.

Anthony started graduate school at the University of Illinois at Urbana-Champaign in 1999. He worked for a brief time under the supervision of Russ Giannetta, studying two-dimensional electron gases in mesoscopic structures. In 2001, Anthony joined the research group of Alexey Bezryadin and began studying quantum effects in superconducting nanowires, a subject he has worked on to the present time. Every semester that Anthony was supported by a graduate teaching assistantship he was named to the Incomplete List of Teachers Ranked Excellent by Their Students with a designation of "Outstanding".

After completing the Ph.D. program at Illinois, Anthony will study nanostructures fabricated from cuprates, manganites, and other complex oxide materials at Brookhaven National Laboratory.

Reproduced with permission of the copyright owner. Further reproduction prohibited without permission.